

Characterization and Modeling of Fundamental Electrical Behavior of QCM Devices

A Thesis

Presented in Partial Fulfillment of the Requirements for the

Degree of Master of Science

with a

Major in Chemical Engineering

in the

College of Graduate Studies

University of Idaho

by

Nathan Wilkerson

December 2014

Major Professor: Mark F. Roll, Ph.D.

Authorization to Submit Thesis

This thesis of Nathan Wilkerson, submitted for the degree of Master of Science with a major in Chemical Engineering and titled “Characterization and Modeling of Fundamental Electrical Behavior of QCM Devices” has been reviewed in final form. Permission, as indicated by the signatures and dates given below, is now granted to submit final copies to the College of Graduate Studies for approval.

Major Professor _____ Date _____

Mark F. Roll, Ph.D

Committee Members _____ Date _____

Vivek Utgikar, Ph.D

_____ Date _____

D. Eric Aston, Ph.D

Department Administrator _____ Date _____

D. Eric Aston, Ph.D

Discipline’s College Dean _____ Date _____

Larry A. Stauffer, Ph.D

Final Approval and Acceptance

Dean of the College
of Graduate Studies _____ Date _____

Jie Chen, Ph.D

Abstract

The purpose of this project as proposed is to further the knowledge of crystal oscillator and quartz crystal microbalance systems, while attempting to increase insight into the systems behavior by investigating the fundamental electrical properties and behavior of the system during operation. This was accomplished through the integration of previously discovered measurement techniques and equipment that have as of yet not been applied to these type of systems. By implementing and combining the results obtained by this project as well as future research it is anticipated that many new relationships and equations relating the behaviors exhibited by the system may be obtained while improving the accuracy of values traditionally being measured.

Using electrical results from common oscillator systems as a control values for more refined QCM systems, it is possible to compare the data to digital models of these systems. The results produced by the uncoated QCM tracked very closely to the digital model whose properties were matched to its specifications, even after accounting for any potential sources of error. Using this digital model it is possible to correlate the commonly measured electrical values and properties of QCM systems to their resulting mechanical behavior. These types of comparisons are necessary in order to gain additional insight into the system and the relationship between the voltage/current and mechanical properties in piezoelectric resonators as described by current piezoelectric theory.

Acknowledgements

The author would like to thank his Major Professor, Mark Roll as well as his committee members Eric Aston, and Vivek Utgikar. Finally I would like to thank Prof. Wudneh Admassu for his assistance in the final months of the project.

Table of Contents

Authorization to Submit Thesis	ii
Abstract.....	iii
Acknowledgements	iv
Table of Contents.....	v
List of Figures	vii
List of Tables	ix
List of Equations.....	x

Chapter 1: Introduction and Background

1.1 Introduction.....	1
1.2 Piezoelectric effect	2
1.3 Quartz Crystal Microbalance(QCM)	4
a. Background	4
b. QCM Operation	5
c. Issues with QCM Technology	8
1.4 4-point probe	10
1.5 SQUID (superconducting quantum interference device)	12
a. SQUID Background	12
b. SQUID Theory.....	14
1.6 LabVIEW Environment.....	15
1.7 COMSOL Background.....	16

Chapter 2: Experimental System Setup

2.1 Equipment Configuration and Instrumentation	19
2.2 LabVIEW	22
a. Writing a LabVIEW VI	22
b. Labview Integration	25
2.3 QCM Measurement Setup	25
2.4 SQUID Measurement Setup.....	29

Chapter 3: Modeling

3.1 Model design	30
3.2 Modeling results and interpretation	35
a. Basics properties at resonant peaks	35

3.3	Effects of Variations in Driving Circuit and Signal.....	40
3.4	Effects of Operation in Water Based Testing Environments	44
Chapter 4: Results		
4.1	Analysis of Common Oscillators	48
a.	Frequency Response analysis.....	48
b.	SQUID Linearization	51
c.	Four-Point Probe Tests.....	55
4.2	Electrical Output and comparison of QCM Devices	58
4.3	Water and Cell QCM Operation.....	63
d.	Comparison to digital models	67
Chapter 5: Conclusion and Future Work		
5.1	Project Conclusions	74
5.2	Next steps	76
5.3	Project Applications.....	77
	References	78
Appendices		
	Appendix A: FRA data for common oscillators.....	83
	Appendix B: Multimodal operation of digital model	88
	Appendix C: SQUID linearization data.....	90
	Appendix D: Half max frequency input-response data for QCM/oscillators	91

List of Figures

Figure 1: Illustration of various cuts possible from a quartz crystal.....	2
Figure. 2: Representation of thickness shear piezoelectric motion	5
Figure 3: illustration of a typical QCM design and set-up.	5
Figure 4: simple quartz oscillator circuit.....	6
Figure 5: Temperature induced resonant frequency changes for various quartz cuts.	9
Figure 6: Simplified diagram of a 4-point probe.....	10
Figure 7 : Voltmeter attachments to standard quartz oscillator.....	11
Figure 8: Simplified model of a SQUID.....	12
Figure 9: Visualization of flux vs. current effects.....	12
Figure 10: Data collection head attached to 100L helium dewar.....	13
Figure 11: Typical current vs. flux output for SQUID operation	15
Figure 12: Typical current vs. voltage and voltage vs. flux outputs for SQUID operation.....	15
Figure 13: Image showing necessary lab equipment.....	18
Figure 14: Voltmeter VI front panel.....	22
Figure 15: Voltmeter VI block diagram.....	22
Figure 16: Various common oscillators used for testing.	25
Figure 17: Frequency response (phase in blue) of a 5 MHz oscillator as measured by a HP89441A	26
Figure 18: Power ratio (red) and Absolute power vs. frequency	27
Figure 19: Source modes on plotted oscilloscope (50ms/div).	29
Figure 20: Comsols piezoelectric device equations for frequency domain operation	31
Figure 21: Original crystal oscillator model	31
Figure 22: 1-inch scaled quartz oscillator	32
Figure 23: Partial electrode and visualization of resulting displacement field distribution.....	34
Figure 24: Changes in electrical potential with respect to Phase.....	34
Figure 25: Displacement field at center point for important phases vs. frequency.....	36
Figure 26: Displacement field at center/avg. for important phases vs. frequency.....	36
Figure 27: Displacement field in the X-direction vs. coordinate in the x, mounted (green) vs. non-mounted	37
Figure 28: Displacement field vs. frequency.....	38
Figure 29: 3-nodal(x) operation.....	39
Figure 30: 3-nodal(y) operation.....	40
Figure 31: Peak displacement vs. applied voltage.....	41

Figure 32: External circuit for COMSOL model	42
Figure 33: Peak displacement of various Cs values vs. frequency.....	43
Figure 34: Peak displacement vs. capacitance	44
Figure 35: Water(blue) as seen atop QCM that is enclosed in a cell.....	45
Figure 36: Full surface water(blue) coverage approximation.....	46
Figure 37: Visualization of “submerged” QCM.....	46
Figure 38: Simplified Full width half max measurement illustration.....	49
Figure 39: Illustration of SQUID linearization setup	51
Figure 40: SQUID outputs as measured by a VSA.....	52
Figure 41: SQUID output vs input for various linearly operating oscillators	53
Figure 42: Illustration of test setup used for oscillator and QCM measurements.	55
Figure 43: Close-up photo of QCM used for final testing.....	58
Figure 44: Pressure acting on the QCM in N/m ² at phase = 270 degrees	60
Figure 45: Value of stress tensor x on the QCM in N/m ² at phase = 270 degrees.....	61
Figure 46: Maximum acceleration acting on the QCM in m/s ² , Max at phase = 270 degrees	61
Figure 47: Maximum velocity of QCM surface in m/s, max values seen at phase = 180 degrees	62
Figure 48: QCM resting in disassembled cell	64
Figure 49: QCM submerged in water cell (open top)	64
Figure 50: Closed and connected water cell for QCM	65
Figure 51: Effects of water on bare QCM device.....	65
Figure 52: Effects of water in cell testing	66
Figure 53: Partial water coverage as seen in ‘cell’ testing.....	68
Figure 54: Full water coverage approximation as seen in ‘water on bare QCM’ testing	69
Figure 55: Submerged QCM model approximation.....	69
Figure 56: Submerged QCM model semi-transparent midsection cutaway	70
Figure 57: Mechanical FRA for partial ‘cell’ coverage	71
Figure 58: FRA for Full ‘water on bare QCM’ coverage	71
Figure 59: Mechanical FRA for submerged QCM.....	72

List of Tables

Table 1: frequency tolerance of common oscillators	49
Table 2: Peak spread of common oscillators	50
Table 3: Trend line data for Figure 38.....	54
Table 4: Voltage and current measurement data for common oscillators	56
Table 5: Real data vs. digital model	57
Table 6: QCM Voltage and current: measurements vs. model Predictions.....	59
Table 7: Mechanical results of the digital model vs. modeled electrical values.	63
Table 8: Peak spread and Q-factors for water based testing	67
Table 9: Water models peak spread and Q-factors comparison	72

List of Equations

Equation 1: First Saurbrey relation	4
Equation 2: Second Saurbrey relation	4
Equation 3: COMSOL domain relations	30
Equation 4: SQUID linearizatiom equation	54

Chapter 1: Introduction and Background

1.1 Piezoelectric Effect:

Quartz crystal microbalances (QCM) are a relatively new application of the old and well explored quartz resonator technology. Using the precisely known properties of quartz and the piezoelectric effect QCM technology has been able to make mass measurements that are otherwise unavailable. Traditionally researchers have been forced to use precision analytical balances, which are many orders of magnitude less sensitive than what is possible with current QCM technology.^[1] Utilizing the knowledge of the underlying quartz oscillator, QCM technology has already been adopted in a number of settings across a few fields of study. In the material sciences it has been applied for monitoring the rate of deposition/adsorption or testing the viscoelastic properties of polymers. It has also seen use in biomedical study due to its ability to test the binding rates for proteins on activated surfaces, interactions between biomolecules, and biofilm or colony growth rates.^[2] To get this fine mass measurement, precise frequency measurements are made of the QCM during operation and using known relations thickness values of the sample are produced. Then with known density (which can also be inferred with QCMs), it is easy to reach a precise mass measurement. These measurements are extremely sensitive, but interpreting current modeling and measurements is very difficult for complex systems and has been limited thus far by a number of factors inherent in this new application, causing resulting data to be several orders of magnitude less accurate than is theoretically predicted.^[1]

Most if not all applications of QCM technology have been limited to properties derived from the measured frequency values and the Sauerbrey relations derived from previous quartz resonator research. Examining the QCM research pool turns up little to no information on how basic electrical properties such as voltage and current through the system are related to the system's mechanical behavior. The purpose of this project is to further the knowledge of quartz crystal oscillator systems by taking precision electrical measurements of QCM systems during operation in standard settings for the system including open systems and water cell operation. Using the electrical data, it is possible to compare commonly measured values and properties to digital models, in order to gain additional insight into the system and the relationship between the voltage/current and mechanical properties in piezoelectric resonators as described by current piezoelectric theory. This was accomplished through the integration of preexisting measurement techniques including a specialized "zero resistance" superconducting current measurement device and a probe layout scheme designed

specifically for low noise electrical data collection. These techniques, as of yet not been applied to QCM sensors, provided crucial electrical data that have not been explored in previous work. As no other results of this sort are available for comparison, three-dimensional physics models were produced in tandem to experimentation to provide understanding as to what mechanical effects would be produced in an identically modeled QCM and electrical environment.

1.2 Piezoelectric Effect:

The piezoelectric effect is the fundamental physical phenomenon describing a specific and direct relationship between the electrical and mechanical action within a system. The materials in which the piezoelectric effect may be observed include a number of solids, but are generally crystals that contain no inversion symmetry (symmetrical with its mirrored image).^[3] The piezoelectric effect is most often described as the generation of an electrical field upon the application of an external mechanical force, which has seen common application in a variety of places from microphones to lighters. However this electrical generation effect is reversible and as such they will generate internal mechanical strain when an external electrical field is applied. The mechanical strains generated, specifically in crystals create uniform shear modes depending on the orientation of the crystal or how it is cut as well as how the electronic field is applied. By examining the quartz crystal in **Figure 1** (quartz is the most common and relevant example), it can be seen than many different *orientations* may be cut from the source crystal and produce a large numbers of unique characteristics specific not only that material but that specific cut.^[5]

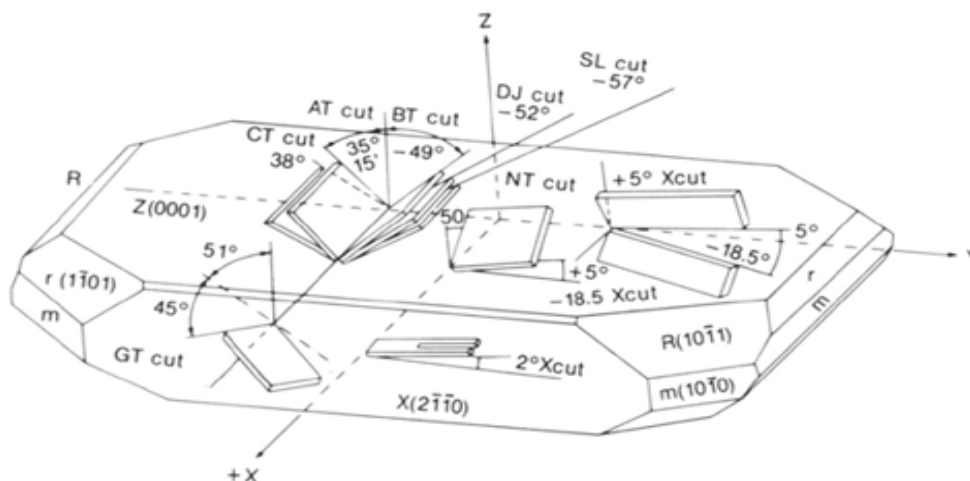


Figure 1: Illustration of various cuts possible from a quartz crystal. [3]

The wide variety of sensors and inherent usefulness of the piezoelectric effect has led to widespread use and marketization of devices for a large number of purposes. Currently, the largest application in terms of quantity is the market for portable high voltage sources^[4] using materials like quartz, which when provided sufficient strain can generate a potential of many thousands of volts. A common form of this application is electric (non-flint) butane lighters and stove tops, which use a spring-loaded hammer to strike a piezoelectric crystal, producing a sufficiently high voltage to allow a spark to leap across a gap in the element ignite the gas. This use has been named piezo-ignition and these types of devices range in size from small enough to fit inside small pocket lighters to several inches in devices meant to light much larger lantern/grills/stoves.

The second major use of these materials is for use in sensor and actuator applications. When cut and electroded to interface with electronic circuitry, it makes for a useful sensor for measuring pressure waves or other important strain inducing effects in a specific direction. Strain from the pressure variations on the crystals surface are converted into an electrical signal and can be read and translated by the relevant instruments, and as such they are commonly used in both microphones and as instrument pick-ups used in amplifying acoustic instruments. As this effect is reversible these materials may be driven by an electrical signal to create a pressure wave useful for certain speaker applications as well as for ultrasound devices. This last use is possible since these applications can be and often are combined into a single device called a transducer that performs both roles. An example of this type of device is the ultrasound device that doctors use for abdominal scanning which both creates the ultrasonic signal and then receives the returned waves to be analyzed.^[5]

The third major application of piezoelectric materials is using them (mostly quartz) as a frequency standard for radios and time keeping devices. Rigid materials vibrate preferentially (resonate) at particular frequencies creating standing modes of vibrational modes that can build, depending on the devices dimensions and dissipation characteristics. For piezo-active materials, at these resonant frequencies, mechanical energy and electrical potential energy are efficiently converted one to the other. These characteristic resonant frequencies are the basis for current quartz oscillator circuits, and the exactness (or quality, Q) of these specific frequencies in quartz is essential for keeping time and serving as an “invariant” radiofrequency reference. It is a mixture of these last two applications (frequency standard and transduction) in a device called a Quartz crystal microbalance which will be discussed next that is the focus of this research.^[5]

1.3 Quartz Crystal Microbalance

QCM Background

A basic quartz crystal microbalance (QCM) is an electronic oscillator circuit that utilizes the piezoelectric effect to drive the crystal sensor at mechanical resonance. Precise measurement of the frequency of resonance in the QCM and any changes allows the calculation of a mass and/or film thickness. A disturbance from the initial resonant frequency is caused by the addition or removal of a small mass causing an effective change in resonator thickness and the resonant acoustic wavelength.^[06,8] Two of the more simplified functions describing this relationship can be seen in equations **1, 2**.

$$\frac{\Delta f}{f} = -\frac{\Delta t}{t} \quad (\text{Eq. 1})$$

$$\Delta f = -\frac{2f_0^2 \Delta m}{A\sqrt{\rho_q \mu_q}} \quad (\text{Eq. 2})$$

Equation 1 shows that change in frequency (f) can be represented as simply a function of change in oscillator thickness (t). Equation 2 on the other hand shows the frequency shift from the fundamental frequency (f₀) of the oscillator as a function of mass (m), active area A), as well as oscillator density (ρ) and shear modulus (μ). This second equation is generally more useful as it makes it possible to determine changes in surface mass, but it is only valid for extremely thin films with mechanical rigidity and resonance exactly as that of the quartz. In practice this equation may be implemented with sufficient accuracy to most films <5% of the crystal's original mass, provided the film is also sufficiently rigid.

For greater accuracy outside of these limits analytical models of the fundamental voltage and current measurements are necessary. The development of new techniques for performing these measurements is a key goal of this project, allowing for accurate measures of many properties ranging from mass and density using Equation 2 as well as several other more complicated values such as viscoelastic properties when other relations and measures are applied.^[7] The most common material for this application is quartz and as shown in Figure 1, quartz resonators come in a variety of different 'cuts' of the source crystal, the cut orientation depends on desired the properties whose purposes are often specialized for specific conditions or tests. For brevity's sake the background discussion will focus on the AT-type utilized by QCM instrumentation which happens to be the "thickness shear mode" represented (though highly exaggerated) by **Figure 2**.

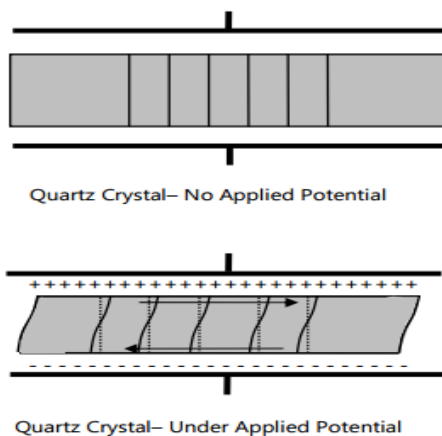


Figure 2: Illustration of thickness shear piezoelectric motion ^[8]

QCM operation

Traditional QCM sensors consist of the base quartz crystal wafer with deposited metal electrodes which usually cover only a portion of the surface, not unlike a standard quartz oscillator built with electrode access as a primary concern. The electrodes come in many arrangements but typically start on one edge of the crystal and extend inwards across each face from opposite directions; an example of this can be seen in Figure 3. ^[12-14] The region where the electrodes overlap is where the radio frequency current passes through the QCM and thus where the piezoelectric action is seen. This arrangement allows for connections from electrodes to the quartz on the sides such that they are causing minimal dampening or other impact on the motion of the system.

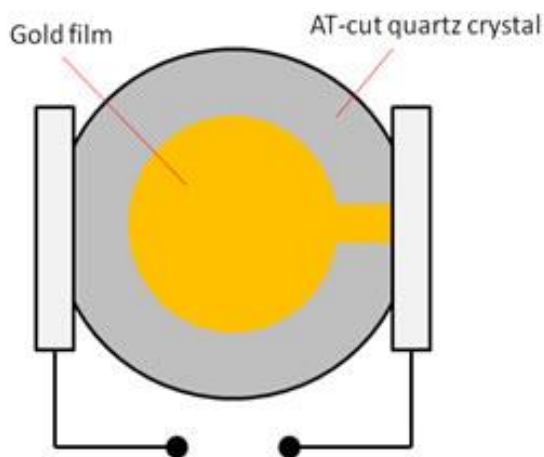


Figure 3: illustration of a typical QCM design and set-up ^[24]

In order for meaningful results to be obtained in a QCM measurement a thin film sample of uniform thickness must be adhered across the surface of the QCM sensor. Powders and polycrystalline substances like ceramics or other such materials often prove to be unsuitable as they may not properly adhere and mechanically couple to the QCM surface, resulting in unpredictable mechanical resonance behavior. This particular issue may be rectified in the future by using some form of modeling but their properties cannot as of yet be determined reliably. The behavior properly adhered films has been extensively researched by Hinsberg and others^[17] This research led to several methods being commonly used to prepare thin film samples for the QCM: dip coating, drop coating, spray coating, spin coating, and self-assembled monolayer (SAM) formation. This previous work shows that spin coating of thin films generally produced the greatest sample consistency and should be preferred if the process is possible with the film of interest.^[15-18] Once the sample is prepared on the quartz wafer, it is placed into a metal base that serves to both suspend and hold the wafer while applying power to the electrodes in a manner similar **Figure 3**.

Typical QCM instrumentation operates with the sensor as the resonant component in a basic oscillator circuit as shown on the following page in **Figure 4**. Such circuits are exactly the same as a basic quartz oscillator circuit, only the environmentally isolated, traditional quartz resonator is replaced with the sample-coated sensor. With a sufficiently low-loss sample film, the QCM wafer behaves just like a standard quartz crystal resonator, the oscillator circuit operates at resonance, and a high precision frequency counter (sub-PPM sensitivity) is used to determine the resonant frequency of the circuit and therefore the QCM sensor itself. This simplistic measure of frequency has been the sole value taken by the vast majority of QCM instruments thus far, though this is often the most important result, several other measurable values may be taken during QCM operation that have been overlooked.

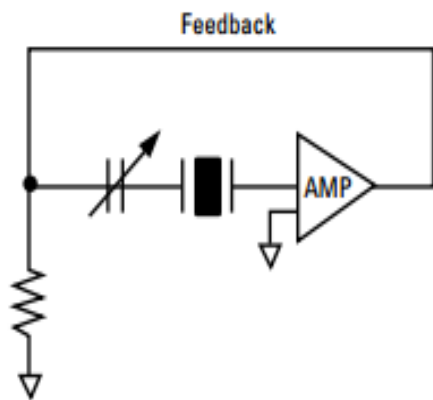


Figure 4: simple quartz oscillator circuit.

[25]

For greater precision, quartz resonators are characterized by transmitting radio-frequency power through the sensor and examining the transmitted and reflected signals. This allows for basic measurement of the frequency as well as signal reflection and dissipation to be determined. This power is most commonly delivered by equipment such as a vector signal analyzer (VSA) or other signal generators, providing fine signal shaping

and frequency control of the delivered RF signal should it be desired. Currently, a sinusoidal wave is typically used as the driving signal.

The electrical or mechanical dissipation in the sensor, gives valuable viscoelastic data for the thin-film when compared to the quartz's known dissipative properties.^[18] For the purposes of modeling for this project the voltage and current responses as well as their transfer through the crystal with relation to frequency, are some of the additional options provided by the VSA.

During these measurements temperature plays an extremely sensitive role, necessitating a thermal bath to stabilize or finely control temperature changes to the system. This control may also be used as part of a method to find extremely delicate or otherwise difficult information, such as when polymer thin films change phase. The result of this transition may be evidenced by a slight decrease in frequency as the density of the substance changes imperceptibly resulting in a thickness change, or a change to the observed dampening as the viscoelastic properties. Any and all of these changes will be evidenced by the extremely fine measurements that can be obtained by measurements taken of the QCM system.^[19] A general sense of the level of possible measurements can be seen by examining the conditions surrounding the adsorption of a monolayer onto the QCM surface:

QCM surface approximately:	$6.25 \text{ cm}^2 = 6.25 \times 10^{14} \text{ nm}^2$
Surface area used by N atom:	$0.15 \text{ nm}^2 / \text{atom N} \rightarrow 4.167 \times 10^{15} \text{ atoms in monolayer}$
Approx. weight of monolayer:	$4.167 \times 10^{15} / N_A * 14 \text{ g/mol} = 9.68 \times 10^{-8} \text{ g}$ or about 100 nanograms
Applying Sauerbrey relation :	$\Delta f = -(2f_o^2 \Delta m) / (A \sqrt{\rho_q \mu_q})$
For 10 MHz QCM ($f_o = 10 \text{ MHz}$):	$\Delta f = \text{approx. } \underline{\underline{3.6 \text{ Hz}}}$

This basic example shows that by applying the governing relations of the system to something as small of scale as the adsorption of and a gas monolayer, the QCM system should ideally produce results well within the measurable range of a number of lab scale devices. Many such instruments are capable of resolving frequencies down into the tenths of Hz range, and as such would seem to indicate that under ideal circumstances the QCM system would be able to make measurements of masses in the tens of nanograms range. As most systems make only one frequency measurement, this sort of mass sensitivity is something currently available only in highly controlled, single component ultra-high vacuum/ gas phase systems.

Issues with QCM Characterization

Though QCM technology has proven its usefulness, particularly in thin-film deposition, there are a number of issues with the technology that have kept these systems from being more widely adopted. These problems may be separated into systematic and externally caused problems. Of the external problems, most of these may be controlled through precise preparation or carefully monitored laboratory conditions, including strict temperature control, and extreme homogeneity in the thin film sample. Although all of these are of some concern to researchers, it is temperature control that occupies the position of largest practical concern.^[19] Operability at temperature extremes and temperature stability are fundamental problems with QCM technology. Operating at too high or low of a temperature or large variations during testing will affect the quality of data. What makes this problem different is that as opposed to the others which can be solved or minimized prior to any data being collected, temperatures are often set by the experiment and fine temperature control may not be a reasonable possibility.

The upper temperature limit for QCM operation is endemic to the material used (in this case quartz), specifically the Curie point or Curie temperature of the crystal. The Curie point is most often thought of as the temperature where a material changes from induced to permanent magnetism; however for piezoelectric materials this is the point at which all piezoelectric properties are lost. This is because electrically induced polarization is a critical property of these materials. When piezoelectric materials are warmed above their Curie temperature, the lattice structure becomes fully polarized and the effects of any external electrically driven changes disappear. While piezoelectric properties persist up until the Curie temperature is reached it is often advisable to operate below half of the material's individual Curie temperature to ensure that no permanent changes occur to its performance and consistently precise performance. In the case of quartz with its Curie point of 840°K would necessitate operation below ~ 420°K (280°C). This should be seen as the maximum operation temperature for quartz crystals so as not to cause long term changes to the QCM's operation, though operation at even lower regimes is recommended due to the large variation in behavior seen up to that point

The effect of temperature variations is limited in most laboratory settings due to the widespread use of the AT cut quartz with its temperature stabilized properties in QCM devices. The implementation of this specific cut allows for researchers to assume ideal behavior and ignore the

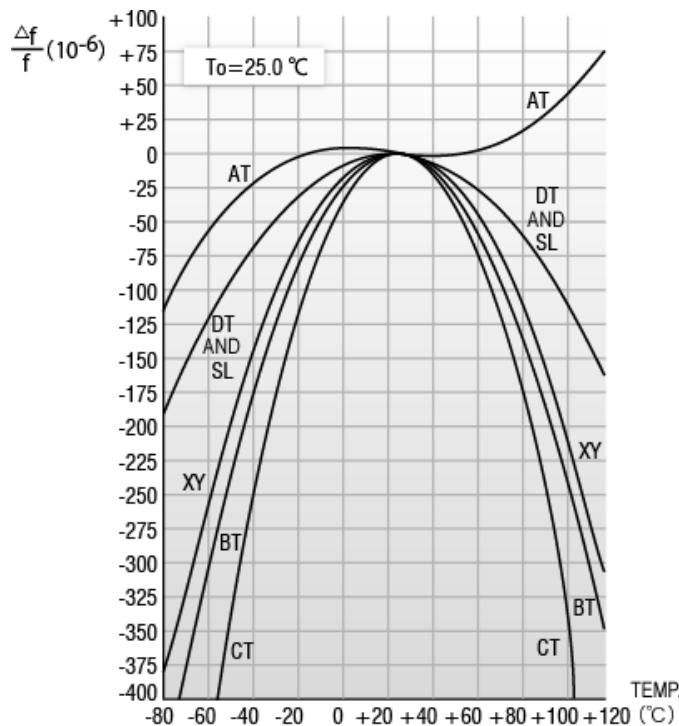


Figure 5: Temperature induced resonant frequency changes for various quartz cuts. ^[23]

effects of temperature variation within a rather wide range around room temperature (-20°C up to 60°C). Operation outside of this range is also possible with limited accuracy when using the known relations in frequency changes for each cut- as seen in the **Figure 5** below. The AT- cut is considerable more consistent with respect to temperature due to its orientation limiting the localized stress points within the crystal. This leads to a deviation in the crystal's innate resonant frequency from its original value. Since this value is used as a set-point for measuring frequency changes due to mass and/or thickness changes and can't be measured during/ after experimentation, it is crucial that this base resonant frequency does not change during a test's duration. Often this means that experimentation that might benefit from the

high level of accuracy cannot be performed, thereby significantly limiting the number of applications, where the QCM would otherwise be an excellent measurement tool. This issue isn't directly addressed by this project, but some interest has been gained in utilizing this work and applying it to possible high temperature piezo-material candidates, discussed in the future work section at the end of this paper.

The other problems associated with QCM devices are systematic issues, or involved with the QCM as a real world measurement device. Namely that the systems that better represent theoretical QCM equations and models are those which are arranged in configurations to simulate isolation. However, this type of idealized system uses measurements based on impedance analyzers or system decay methods utilizing equipment often requiring large capital investment and complex configurations and setup making it considerably less useful where portability or fast measurements

are desired.^[22] Alternatively, systems which provide adequate accommodations for reasonable simplicity may provide less accurate results due to the lack of vacuum, isolation, or possibly the sub Hz frequency measurements necessary for the maximum accuracy while measuring systems.^[20, 21]

The last problem that needs to be discussed also has to do with the actual process of measuring data and will be discussed at various points throughout this paper. The issue has to do with the ability of a measurement device to capture data influencing the measurement. Voltage drops to and from common measurement devices cause a disparity in the actual value from that which is measured (discussed in the next section). While this is generally of negligible concern with most standard electronics, when dealing with the level of accuracy accommodated by the QCM systems and the low level of currents dealt with in some QCM applications, even this often unobtrusive effect is something worth examining closely and trying to minimize. Accordingly a few methods of minimizing the effect were determined. As they happen to be partially physically implemented solutions, they will be discussed across the breadth of this and the next chapter.

1.4 4-point Probe

Despite a good deal of electrical noise and disturbances being eliminated with quality instrumentation, considerable amount of non-ideal effects, such as resistive voltage drops and other such phenomena, are still likely to occur within any electrical system. These effects may often be attributed to non-idealities in wires and fixtures connecting the device and instruments. Although this is not something that can be completely eliminated, efforts must be made to minimize the

impact on measurements being made by making changes to standard measurement arrangements.

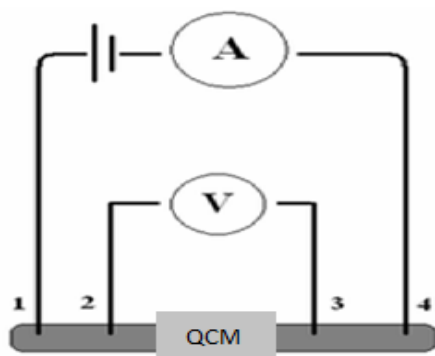


Figure 6: simplified diagram of a 4-point probe [26]

Towards this goal, this research implemented a measurement technique commonly used in low impedance (resistance) measurements, namely the 4-point probe method. This method uses separate pairs of probes that make individual connections to the system; one pair measuring the current and the other pair measuring the voltage. In a 2-probe method, the impedance would be measured by connecting to the

system in tandem with other instruments like a voltmeter and voltage drops in the leads themselves become an unintended part of the impedance measurement.^[27]

Splitting up the two is the key advantage of the system developed in this research and it largely eliminates the effect of the extraneous internal wiring and any additional wiring or non-ideal contact resistances. Specifically for our system the QCM will be mounted on electrically insulating plastic casing. The spring loaded pins will make connections directly to the leads feeding the system. This serves the purposes of separating the device from electrical noise as well as any small errant physical motion or external dampening. Above is seen a generalized example of the 4-point probe, with our system setup including QCM attached in the figure below. This probe makes two voltage measurements using distinct instruments that will be described in detail in the Experimental section.

Measurements of voltage at radio-frequencies are relatively common, and dedicated instruments for this purpose are commercially available. Radio-frequency *current* measurements, in contrast, are very rare outside of high current (much larger than one ampere) measurements taken at radio transmission stations. Our approach requires current measurements in the micro-ampere range, and this requires the use of unique superconductive measurement systems.



Figure 7: Voltmeter attachments to standard QCM sensor

1.5 SQUIDs (Superconducting Quantum Interference Device)

SQUID Background

SQUID is a seemingly simple circuit produced by including one or more superconducting loops containing two Josephson junctions (one on each side of the loop), that are placed in proximity to a current carrying wire from the system of interest. These Josephson junctions often consist of a thin insulating barrier, a short section of non-superconducting metal, or an electrical constriction that weakens or generally serve to interrupt the ideal current flow of the loop. *Any* magnetic field that penetrates the SQUID influences its behavior, in particular, the current passing through each branch

of the loop and the voltage across the SQUID. In order to control the state of the SQUID at any given time, external feedback coils (loops) are used. ^[28]

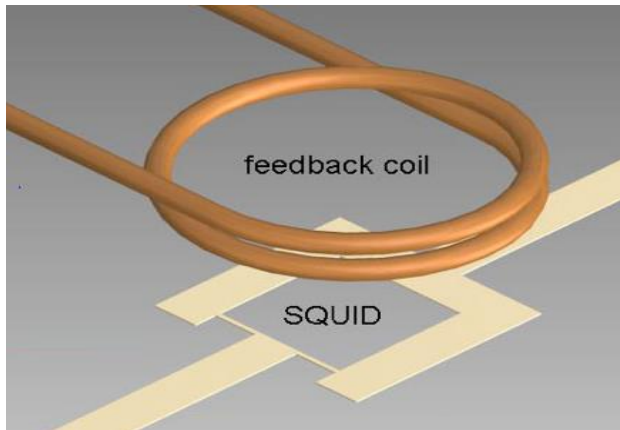


Figure 8: Simplified model of a SQUID.

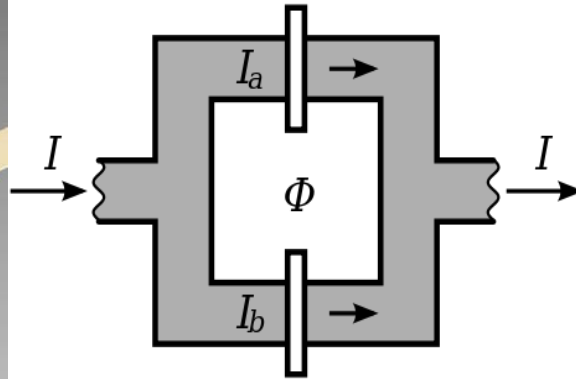


Figure 9: Visualization of flux vs. current

These external loops placed at a given distance and with a preset internal area to produce a specified amount of magnetic flux in response to current travels in the loop. This induced magnetic flux is projected outwards from the feedback coil and passes through the SQUID. This induces a new current in the SQUID, which can cancel external flux, as modulated by the Josephson junctions. A visualization of the device can be seen above.

The purpose of SQUIDs amongst other things is to serve as a sensitive magnetometer, and is generally the most accurate/low noise device available. However due to the necessity of low temperatures for materials to show their superconducting properties, even low precision SQUIDS must be cooled with liquid nitrogen while more accurate devices requiring much lower temperatures. The temperature requirements are given by the T_c value (or the characteristic temperature above which superconducting properties and behavior disappears) of the specific superconducting material. ^[28] In the case of the niobium SQUIDs being used in this experiment, it was necessary to chill the device in a dewar of liquid helium which can be seen in **Figure 10**.

Low T_c SQUIDs of this caliber are more than capable of measuring the magnetic fields as low as those produced by neurons firing and have seen considerable biomedical use. ^[31] However it is the low noise superconductor's ability to make measurements of electrical current (e.g. our QCM system) that is of interest for this research. Theoretically, SQUIDs contribute nearly zero resistance to

an electrical system, making them an ideal ammeter. This will increase the accuracy of the data available from the extremely precise QCM technology by reducing noise and other effects that are associated with measuring an electrical signal.



Figure 10: Data collection head attached to 100L helium dewar

SQUID THEORY

Since the measurements taken by SQUID are made entirely by feedback loop and superconducting loop a SQUID might reasonable be visualized by the simplified **Figure 9**. In its normal state of operation and without any external magnetic field, the input current splits equally between the branches. However if a small magnetic field penetrates the loop, a current is produced to cancel the applied flux. Depending on the direction of flux the induced current in one of the sides will be in the same direction as the initial current while the other branch's induced current will flow opposite. Representing the initial input current delivered to the SQUID as (I) and the induced current from the field as (I_f), then the total current in each side (side a and b as shown in **Figure 9**, becomes $I_a = I/2 + I_f$ and $I_b = I/2 - I_f$. At some point however the new current in one of these branches will reach

the critical current (maximum current that can readily pass through the junction) value for the Josephson junction ($I_c < I/2 + I_f$)

As soon as the current in either branch exceeds the critical current a voltage potential is formed across the Josephson junction as current is restricted. This potential difference formed across the junction due to the constricted flow creates a situation where continuing to increase the flux causes an increasing high and thus unfavorable energy state for the superconducting system. Since normal superconductivity is such a low energy state this drives the system to allow a certain amount of flux to enter the loop and become enclosed within. This entrapped flux called a flux quantum (ϕ_0) combats the external magnetic field allowing the loop to return to a lower non-critical current. Thus the critical current, which is reached as the induced magnetic field becomes greater than $\phi_0/2$ becomes reduced by a value corresponding to the decrease in the external field by a value of ϕ_0 . Accordingly the loop acts as if the external field has a flux of $-\phi_0/2$ causing the current in the superconducting loop to reverse to a value of $-I_c$. If the magnetic field continues to increase the reversed current will slow and begin flowing in the original direction until I_c is once again reached, and the process repeats. In a properly calibrated SQUID this quantization of flux gives a direct measure of the current flowing through the wire that is causing it. ^[32]

A SQUID is calibrated by setting a specific value for the input current (I), used in the previous equations. By examining those equations ($I_c = I/2 + I_f$) it's clear that by setting this value to some figure less than twice the critical current it's possible to directly affect the value of ϕ needed to reach the critical current. Note that despite it not being shown, for all input currents greater than the critical current the SQUID will not operate properly. ^[32] When this flux-current relationship is plotted in graph form as seen in **Figure 11**, you can see the current ratio in the loop (shown as I/I_0) drops to zero as the flux reaches its $\phi/2$ flux quantum, where ϕ_0 and I_0 are one flux quanta and the current induced due to a single flux quanta respectively. **Figure 12** shows the a generalized graph called a SQUID characteristic that gives you an idea of the amount potential generated during the cycles followed by its relationship with flux. ^[36]

Most commonly, a SQUID is controlled within a *flux-locked loop* (FLL), which maintains ϕ at zero by cancelling the *sensed* magnetic flux by passing current through additional feedback loops. The black data collection box seen atop the dewar in Figure 10 is the FLL and its feedback signals are recorded by the computer. Knowing the inductance of each feedback loop, the feedback current can

be directly related to the magnetic field being generated by the current passing through the QCM sensor. This provides the only direct measurement of sub-milliampere radio frequency currents available.

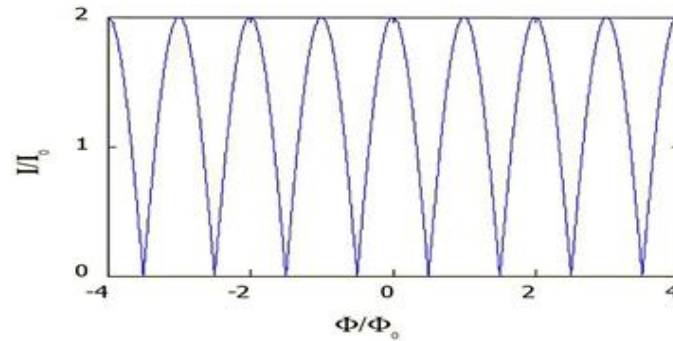


Figure 11: Typical current vs. flux output for SQUID operation ^[33]

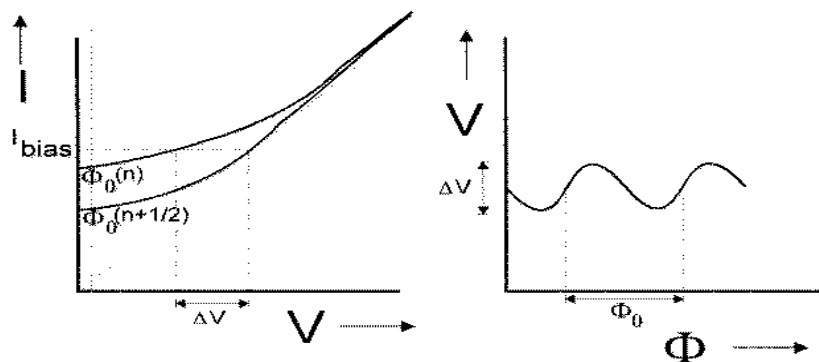


Figure 12: Typical current vs. voltage and voltage vs. flux outputs for SQUID operation ^[34]

1.6 LabVIEW

Though not part of the phenomena being investigated, LabVIEW software was integral to the monitoring of equipment as well as collection of data and as such is referred to multiple times in subsequent parts of this paper but may not be directly apparent what its overall role was. Accordingly the author thought it beneficial to include some small quantity of background information on the software and how it is implemented.

The Laboratory Virtual Instrument Engineering Workbench system or “LabVIEW” is a programming and device interface and operation environment developed by National Instruments. The

software itself involves the creation of a set of integrated programs and subroutines called virtual instruments (VIs).^[35] Each VI is usually programmed and developed to control a single instrument (though systems of VI's may be interconnected for ease of use), and consists of three components: a front panel, a block diagram, and a connector panel. The front panel is built using controls, indicators, and other interfaces for the direct operation of attached instruments and devices. These controls and inputs allow a user to supply information to the VI, while the indicators display the results produced or measured by the device based on the inputs given.

The “back panel”, which is a block diagram or a visual representation of the VI's source code, that is responsible for the proper functioning of all the front panels' indicators and controls as well as all the communication to and from the instrument itself. All of the objects placed on the front panel will appear on the block diagram as terminal blocks to be interconnected to perform the necessary operations. Collectively controls, indicators, structures and functions will be referred to as nodes, where they are referred to separately from other blocks which perform specific functions but do not represent any front panel equivalent. These nodes and functions are connected to one another using wires which represent the flow of information.

Finally each VI has “connector panel” which is used to represent an entire VI within the block diagram of another and may be thought as being separate from either nodes or functions. Thus a single virtual instrument can either be run as a single control program, with the front panel serving as a user interface, or when interconnected a whole chain of VIs may be operated, and a great deal of individual machines may be used in unison for a single goal, like taking several measurements as might be desired when characterizing system conditions. We will expand upon this in Chapter 2 as it pertains to this research.

1.7 COMSOL

Early on in the planning stages a desire for a method for increasing the understanding of the system by visualizing the crystal led to the decision to include a modeling section being added to the project. A considerable amount of this modeling was attempted prior to experimentation during the planning and setup phases of the project. The main purpose of which was to provide 3-D visualizations of the phenomena in the system as well as obtain predictions of the effects of changes made to certain aspects of the system and to help anticipate any problems that might occur. The program that was used for this modeling was COMSOL Multiphysics, which is a finite element physics solver that due to its wide range of included physics models (including those for MEMS systems)

made it a good choice. The program also showed itself useful for its ability to couple multiple areas of physical phenomena and their interactions within systems allowing us to simulate not only the piezoelectric effect itself but also the voltages and other electrical circuitry information is a surrounding imagined circuit. Though there are a great number of physics modules available for modeling systems, giving this software huge number of additional applications, in this case the being modules being used are obviously the MEMS and AC/DC modules. Since its purpose was specifically for the piezoelectric action induced by the voltage passed through the QCM electrodes. This coupling of just these two physics allows for the full modeling of the stress and displacement caused within the crystal without overcomplicating any solutions and increasing calculation time unnecessarily.

Chapter 2: Experimental System Setup

2.1 Equipment Configuration and instrumentation

In order to facilitate quick and easy collection of data for new or complicated experimentation it is important to know what needs are to be met and what equipment is most useful for meeting those needs. In the case of measuring the QCM sensor for the electrical information sought by this project, one might assume that little in the way of complicated equipment would be required. This is true for a majority of electrical circuits, since voltage and current information is easily accessible to anyone with a multimeter. However, underestimating the requirements in this case and using a less accurate alternative is likely to lead to comparatively low accuracy results. This point is critical as it is important to achieve high enough accuracy that the data would lend significance to modeling the behavior of the crystal on the same scale as its theoretical mass measurement range. Accordingly a number of devices aimed at making measurements with utmost accuracy were assembled. You can see many of the major instruments in **Figure 13**.

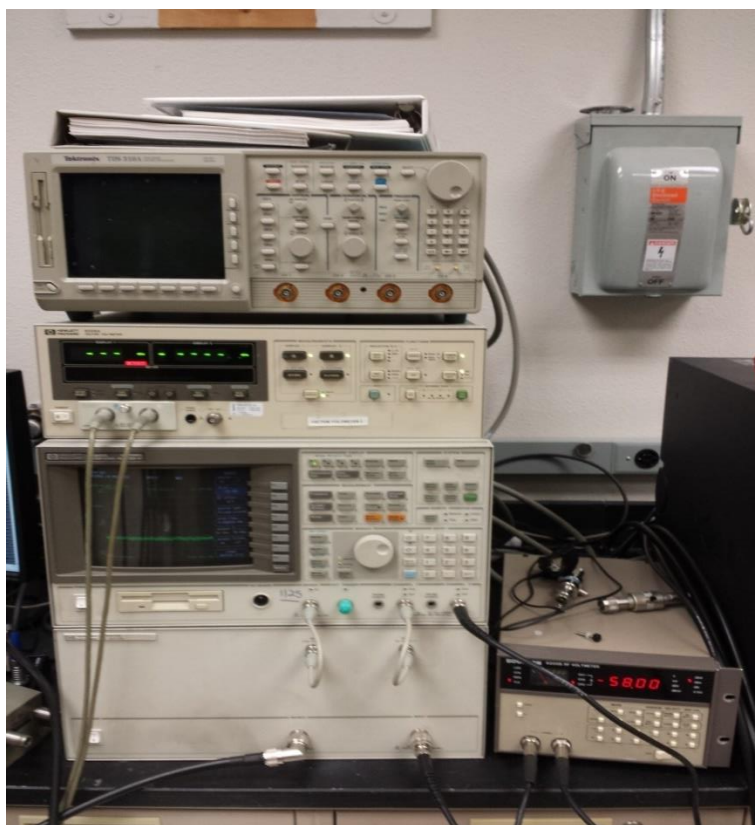


Figure 13: From top to bottom, Oscilloscope, Vector Voltmeter, vector signal analyzer, Boonton voltmeter (bottom left)

For the basic oscillator based QCM system a frequency counter is used to track shifting of the resonant frequency as given by the Sauerbrey relations. To improve on these measurements, toward our goal of investigating mass measurements on the tens of nanogram scale, an instrument capable of a full frequency response analysis (FRA) with the previously mentioned $1/10^{\text{th}}$ Hz resolution was needed. To fulfill this need a HP89441A model Vector Signal Analyzer (VSA) with the accompanying RF unit was

used. Although the instrument is capable of a variety of functions, the primary interest is its multi-channel and cross-channel measurements which allow for this FRA data to be collected.

Critical to this investigation of the QCM system are the voltage across and current through the QCM device at its peak resonance. These measured values are simultaneously the most important to our intended work in this area and the most difficult to measure with the needed accuracy. Their importance is due to their theorized relationship to several non-measurable mechanical properties of the system, such as face velocity and shear force applied to any added mass. However due to the extremely low power through the QCM system (often only a few μW) the measurement of the currents and voltages, particularly in the radiofrequency range is a considerable challenge.

Not only must the instrument be capable of making measurements on this scale (likely a few mV for the voltmeter) but the instrument must also make a minimum of disturbance on the electrical system as was mentioned earlier. In simple terms, the fact that devices such as voltmeter divert some current away from the system in order to measure voltages causes deviations between the actual and measured voltages as a direct result of said measurement. Though this effect is often not of significance in most circuitry applications, when making measurements on the scale in question, this effect will have a real and non-negligible effect. Not accounting for this effect may well make the intended determination of new and useful electro-mechanical measurements and long-term investigation of linear piezoelectric equations for the QCM system considerably more difficult or even impossible.

Therefore it is crucial that the voltage and current measurements be taken in such a way as to minimize these voltage drops. Accordingly an extremely high impedance Boonton dual channel voltmeter was obtained to take these measurements and hopefully reduce the diverted current and overall effect on the system. While quality DC pico-ammeters exist, they do not operate on radio frequency currents and this leaves a need where measurement of current is concerned. Should a current measurement not be included in the setup the only current values would come from direct calculation from other measurements such as the voltage and resistance of the circuit, which would provide little to no additional information.

The constraint of making high sensitivity current measurements at *radio frequencies* eliminated most options, resulting in the planned implementation of SQUID technology into the

system. Specifically the integration of a custom cryo-cooled SQUID manufactured by Magnicon in Germany into the electrical system was a major goal of this project. The superconducting nature of these SQUIDs (discussed previously) would allow for unimpeded current flow through the measuring device and act as an ideal ammeter. ^[32]

The integration of the SQUID along with the benefits that were discussed in Chapter 1 rely on the measurement of magnetic flux quanta passing through a receiver loop separated from the electrical environment. This involves using an oscilloscope as well as proprietary software from the manufacture to make initial calibrations. The implementation of this device was the largest hurdle during the course of the experiment due to extensive delays in the SQUID manufacturing and verification process and resulted in the inclusion of a modeling component to better understand the measurements taken. All testing and data will be discussed in subsequent sections and all graphed data can be found in the Appendix.

Once the accuracy of the equipment was assessed the next step was to make certain that consistency in measurements can be maintained. Due to QCM devices sensitivity to both external vibration as well as small disturbances such as added dust from frequent opening of its enclosure or similar, it is important that any and all possible tests are performed without disturbing system. By making sure that as many relevant measures can be taken simultaneously, internal consistency between measurements on a single device can be enhanced. Removing and changing attachments to the system would likely cause undue fluctuations to the fine measurements being taken even if the device itself wasn't moved as new connections and different cables with slightly different resistances were connected. Accordingly, all the machinery relevant to the system was attached to the system such that the system could be driven and measure by the various machines without connecting or disconnecting anything unless changing the QCM device itself. This was achieved through the implementation of a 4-point probe system and LabVIEW as they serve to better accuracy and streamline the process of taking measurements.

2.2 LabVIEW

Writing a LabVIEW VI

In order to properly communicate with and control an instrument using LabVIEW a VI must be written to accommodate any and all features that the user wishes to perform on said machine. Often times manufacturing companies or National Instruments itself has developed "drivers" or what is actually a premade VI created to perform extremely simple tasks on a given machine (often these

drivers will represent then commands given by a few button pushes on the physical machine). Without these self-contained tasks, the production of a comprehensive (allowing for every operation available to the instrument) user interface for it would require the creation of an extremely complex and difficult to follow block diagram for even the most simple of machines. In this case often the front panel may often be deceptively simple, belying the relative complexity of the programming involved. The example that can be seen below is for the operation of a relatively simple two channel voltmeter.

If the reader examines this example VI front panel shown below that was programmed to operate a fairly simple Boonton voltmeter. It consists of indicators, (graphs and tables and other indicators that simply display returned values) many of which are redundant and only serve to visualize the data in different ways. In fact the VI itself only contains two different controls and start/zero voltmeter options. The first of these controls only selects channel to make measurements on and the other control which consists of actual two knobs (one for each channel as it made it possible to collect two different measures simultaneously) selects the measurement type.

It can be seen despite this despite few controls and no complicated functionality the programming side can quickly become quite tortuous. In fact the program itself contains no less than 19 "IF statements" many of which are nested together and several of which were necessary to help route wiring and achieve proper data control for the dual channel system, so as to let LabVIEW display it in a coherent manner. The result is a complex and often difficult to follow arrangement of commands loops and wires, which without proper annotation would be nearly indecipherable for even the most adept users.

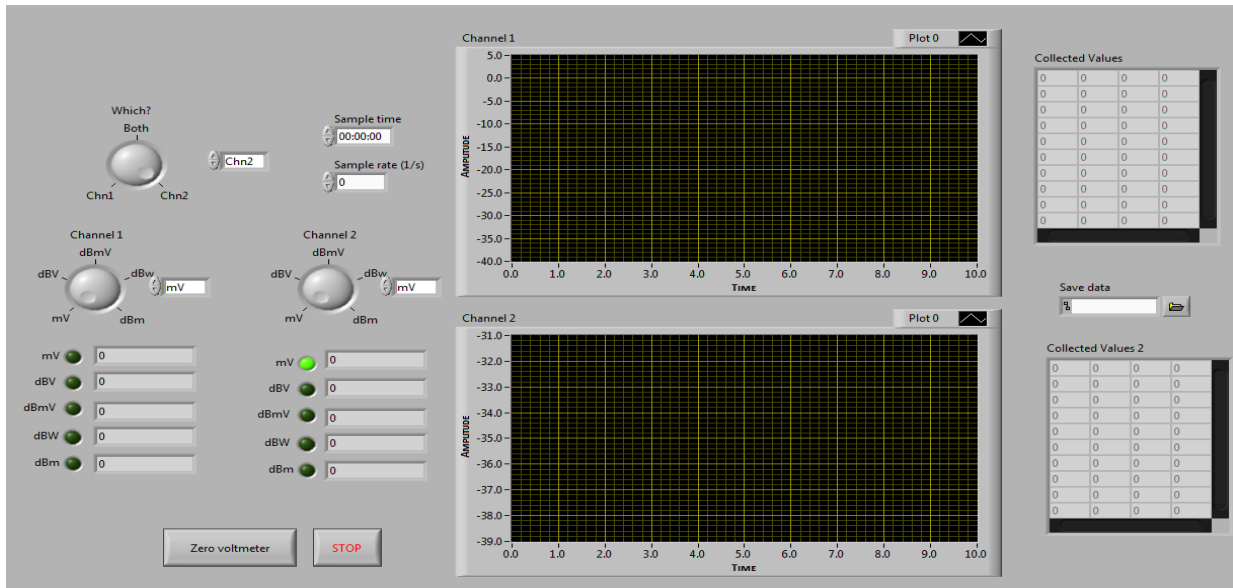


Figure 14: Boonton Voltmeter VI front panel

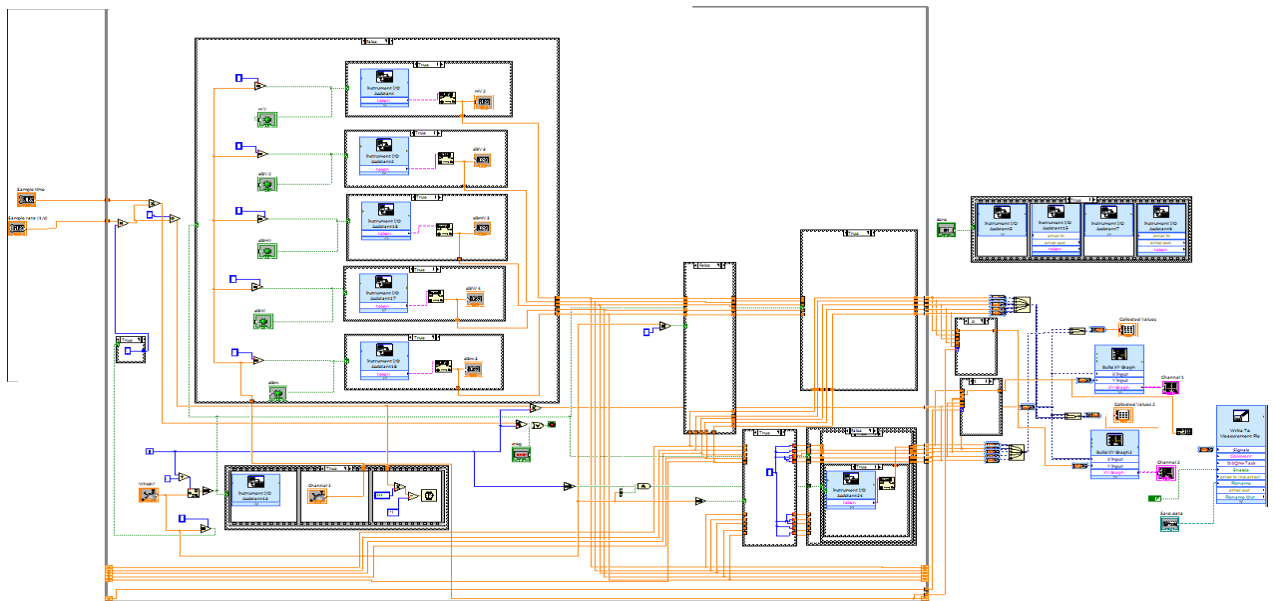


Figure 15: Voltmeter VI block diagram

In this case it would not be unreasonable to say that a more traditional programming scheme would be preferable. It would come down to whether the advance debugging modes (which proved to be very useful in making the above VI) and execution visualization features outweighed the benefits of a more familiarly structured text based programming format, which would come down to the user. If, however, if an instrument comes with prewritten connector panel drivers to assist in communicating with the instrument, the result is an objectively more streamlined process overall and a considerably modular yet easy to access and execute code. The block diagram will generally take the form of a single control attached to a small set of blocks consisting almost entirely of the connector panels.

This sort of programming runs much smoother, especially when troubleshooting by reducing individual tasks into discrete sections, reducing the overall clutter. Despite this fact many of today's instruments have any number of functions with an equal number of configurations options. To program a block diagram for such an instrument would require a front panel screen area similar to that of the machine itself if not larger and several times that for the block diagram. There isn't however a zoom feature included in LabVIEW, so a VI that consists of more than a handful of controls and graphs would become awkward to use and only serve to lessen one of the major benefits of the software, i.e. its ease of use.

In short, despite of any organization that may have been obtained through support drivers, it might still be necessary to split up the function of such a machine into a unified task list instead of a straight forward digital facsimile of the machine's physical front panel. Accordingly, for instruments like the Boonton voltmeter a single VI has been created that can control any operation possible of being performed by it. While a VSA such as the HP89441A being used is likely to have a considerable amount of unique processes and measurements may be performed, it would need a great deal of UI area to accommodate all the buttons on the front of the actual instrument. It is instead simpler to build up a catalog of "function" VI programs that represent all conceivably necessary functions to be performed, as it likely has many functions that may never be used during the course of the current project. In this way a single "library VI" might be built with all of the functions included. This library is meant to remain open and serve as a launching point for each task and streamline the process by opening the function VI in a separate window to perform measurements according to a set of adjustable parameters included within each sub-VI.

Upon reading the last few paragraphs one might wonder about the cost-benefit of spending what could be a considerable amount of time making several VI's for various machines that might simply be operated by hand on the instrument itself. Though this is a legitimate concern for many applications and is likely a primary reason why LabVIEW isn't more widely adopted, it is one of the software's not immediately apparent benefits that make it indispensable for this project. Once the programming portion the LabVIEW software has been completed all these machines can be operated simultaneously controlled and data collected by a single person, where the data can be easily stored and measures directly compared across instruments in real time.

LabVIEW Integration

Discussed previously, the LabVIEW environment is the point that ties the entire scheme together that it may be operated easily. LabVIEW allows for remote operation, measurement, and data collection from each of the instruments simultaneously, providing real-time collection of data for multiple measurements from multiple devices. These devices are interconnected to a central workstation via the fairly old, but widely used, IEEE-488 (or GPIB) interface due its common use in laboratory equipment and ability to stack multiple inputs without limiting throughput. Each GPIB cable was attaches a device to the central workstation where the cables meet and are input to an internal GPIB card inside the workstation. Using the custom and semi-custom LabVIEW VIs made, each device is controlled and measure are taken producing data that is stored digitally as text files along with timestamps and other identifying markers. This allows for the combining of the data contained in these files streamlining the process for more sophisticated analysis. Performing the tests in this manner allows data to be easily obtained and analyzed while also guaranteeing it to be from the same system in the same environment at the same time, ensuring the maximum amount of accuracy with the minimal amount of time and labor.

2.3 QCM Measurement Setup

Focusing only on the instrumental aspect of the operation; the characterization of a QCM device is still a complicated and multistep process that entails the coordinated functioning of a number of instruments to make the necessary measurements. The next paragraph will briefly discuss the steps involved in setup as well as basic measurements schemes and resulting measures. In order to utilize a QCM device it must be powered by external source in order for the quartz to exhibit the oscillatory mechanical behavior. In this case the QCM system will be powered by the VSA due to its versatility in allowing for the creation of signals with a wide variety of possible variations from the

ability to create any number voltages and powers at any specific frequency to more complex changes such as signal shaping.

By producing a range of periodic driving signals of varying frequency at constant voltage or power after passing through the QCM device the *frequency response analysis (FRA)* can be collected. Employing the frequency response features of this VSA, its second channel can measure the response power, more literally the power flowing through the quartz as it changes with frequency. When the power response is plotted against frequency, the resonant frequency can be trivially determined, currently the defining measurement of current QCM systems. Using a number of common oscillators (seen in **Figure 16**), with similar operating frequencies as the QCM to calibrate it; the VSA showed itself to be quite capable of collecting frequency data with sufficient accuracy to use as a comparison for more novel or complicated measurements.



Figure 16: Various common oscillators used for testing.

In **Figure 17** below, a graph representation of the sort of data recorded by the VSA for a standard oscillator used in general electronic applications. In this case you can see the power ratio and phase shift across through the QCM plotted against the driving frequency of the signal for a common sealed 5 MHz oscillator. There are a number of ways to display this same data each with different advantage, which means reporting several closely related data simultaneously might be considerably more informative each on its own. As an example, when the power ratio that was plotted on a log scale is instead put on a linear scale of absolute power, it becomes perhaps less visually descriptive of the system as whole but better shows how peak frequency shifts of the resonant and *anti-resonant* peaks might be much more easily tracked.

Examining **Figure 17** directly, for a majority of the frequency spectrum a very small amount (less than 0.0000001%) of power is being passed through the oscillator and the phase shift in the signal across the resonator is a fairly consistent 90° during those frequencies. As the frequency approaches the resonant frequency for the crystal, the amount of power allowed through increases dramatically until that peak where in this case more than 30% of the power delivered to the oscillator is passed through. Starting very close to the resonant peak (within about 1000 Hz) the phase shift across the resonator begins a 180° flip to -90° , such that the phase is equal to 0° at resonance.

These effects are repeated in reverse forming an anti-resonant peak at approximately 5.01 MHz. This anti-resonance resonance is due to the capacitance of the quartz itself and suppresses the amount of power allowed through the system to figure very nearly 0 (actually $1e-10\%$). Due to this extremely low power being measured by the system the data becomes fairly noisy (especially in the phase measurement) until the amount of power increases to a more reasonable figure as it approaches the background levels.

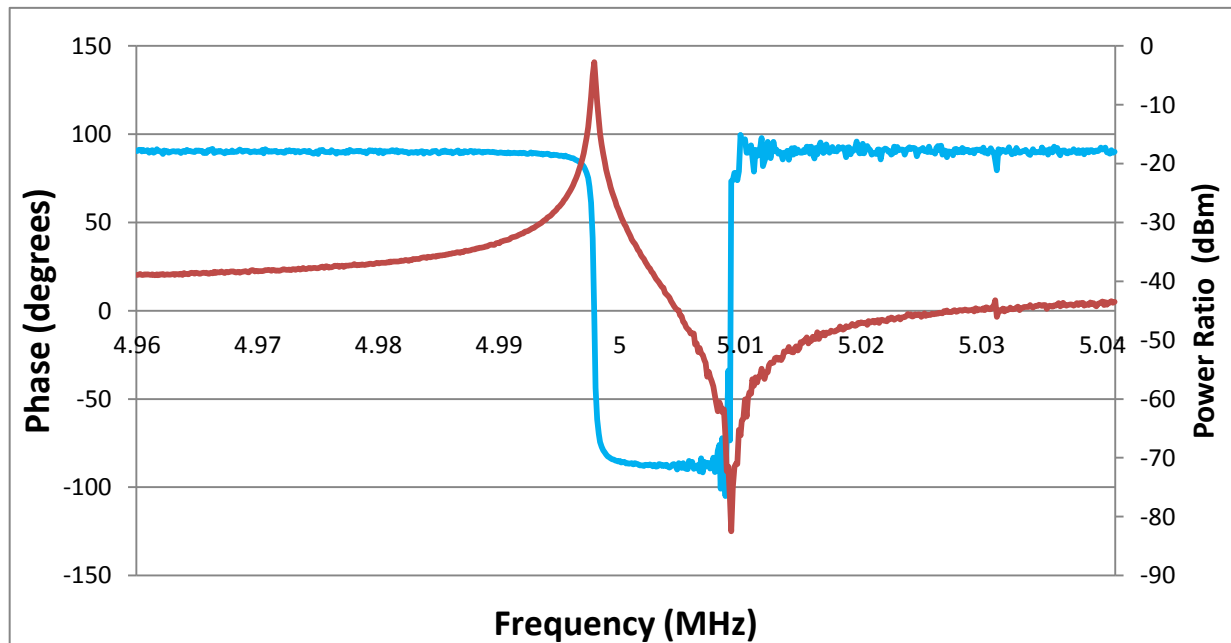


Figure 17: Frequency response (phase in blue) of a 5 MHz oscillator as measured by a HP89441A

As seen in **Figure 18**, the peak frequency on the linear scale aligns exactly with the peak power ratio (@530 μ W and -3 dBm) as would be expected since they are based on the same set of data, but the rest of the plot becomes values so small as to show up as approximately 0 W for the

rest of the graph. What this shows is that relative to a vast majority driving frequencies, at only one frequency does any real amount of power flow through the system. This frequency happens to be the resonance point of this common quartz oscillator whose nominal resonance is 5 MHz but whose actual resonance is approximately 4.99775MHz. This sort of data is extremely useful since it gives a good idea of the tolerances in the common devices. Doing a few of the other tests on these common oscillators as well gives a general idea of how the more sensitive QCMs will react to some additional test that were performed such as operation in liquid which will be discussed in their respective results sections. Frequency responses for the other test oscillators can be found in Appendix A.

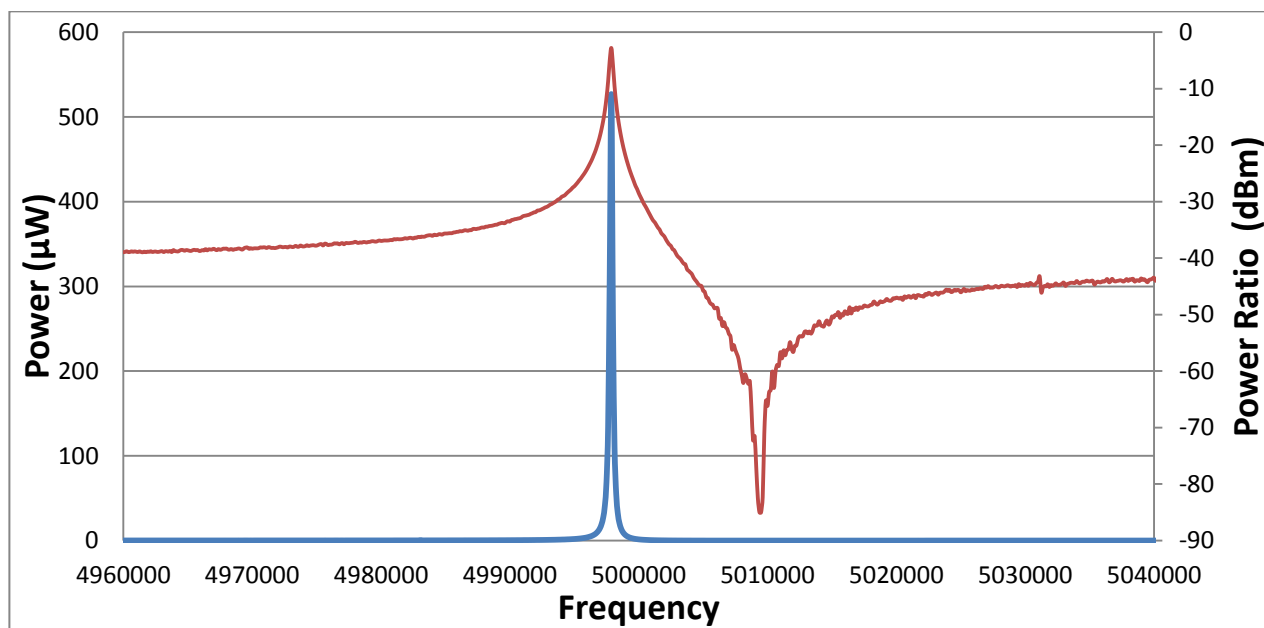


Figure 18: Power ratio (red) and Absolute power vs. frequency

The powering of the QCM and the measurement of the FRA done by the VSA represent can be thought of as input and output of the QCM sensor. However, FRA is not the most fundamental measurement of QCM systems but serves as a baseline or comparison measurement method to this project, which seeks to gain better understanding of the basic electrical parameters for the QCM through the 4-point probe arrangement. The measurements taken from FRA data indicate with good accuracy the frequency at which the maximum amount of power can flow through the individual QCM device in its given configuration. Powering the circuit using a signal of that frequency assures a QCM system operating at peak resonant frequency and thus all of the precision electrical measurements taken will also be representative of resonance.

From an understanding of the piezoelectric effect as well as the Sauerbrey relations it is clear that these peak values that are directly measured by the instruments are in some way related to the mechanical resonance being created. By measuring the “bare” system carefully and by taking measurements with a variety of known systems, will be possible to significantly better model the relationship between electrical measurements and the much less measurable mechanical changes, such as shear force and velocity, at the surface of the QCM sensor.

2.4 SQUID Measurement Setup

To prepare for the arrival of the SQUID a 100 L liquid helium dewar was prepared to house the active superconducting portion of the SQUID during operation, however a few issues with inserting a device such as the Magnicon SQUID needed to be solved. Firstly, the as-purchased measurement head did not seal the top of the dewar, presenting an issue for liquid helium due to its extremely high boil-off rate. An unsealed top would intensify this issue further exacerbating this boiling and shortening the window in which the SQUID was available for collecting data. The solution to this was a custom machined aluminum fitting (seen in **Figure 10** between the data collection head and the dewar) that served to both seal the dewar using O-rings, while also securing the data collection head to the dewar. Once this fitting was attached and it was successful test fit with the SQUID, an order for liquid helium was placed.

After a short supply related delay, the dewar was filled and returned for use, which is where the second issue was encountered. When lowering a room temperature object into a low temperature fluid such as liquid nitrogen, a number of safety precautions must be taken. After donning the proper safety gear including thermal gloves, the object needs to be inserted slowly both to prevent splashing from the increasingly violent boiling and to prevent any damage that might be sustained due to thermal shock. These issues that are present with the 75° K liquid nitrogen are amplified when working with liquid helium and its boiling point of only 4° K. Since it was feared that leaving the dewar open for an extended period would waste a large portion of helium as well as the perceived danger of damage from lowering the room temperature SQUID in directly, the SQUID was first pre-chilled in liquid nitrogen. This served to not only to lessen the necessary time the dewar was unsealed but also lowered the possible temperature gradient experienced by the SQUID.

As with any piece of instrumentation, a custom piece of technology like a SQUID needs to be calibrated in order to operate as expected. Magnicon performed extensive in-house calibration with device-specific bias settings in order to operate at a neutral point and avoid giving biased readings

based off of the noise from any measurement and external magnetic noise. In order to develop fundamental expertise in SQUID sensors at the University of Idaho, basic calibration of the SQUID was conducted through a LabVIEW VI to dial in each of the several bias values as detailed by Magnicon documentation

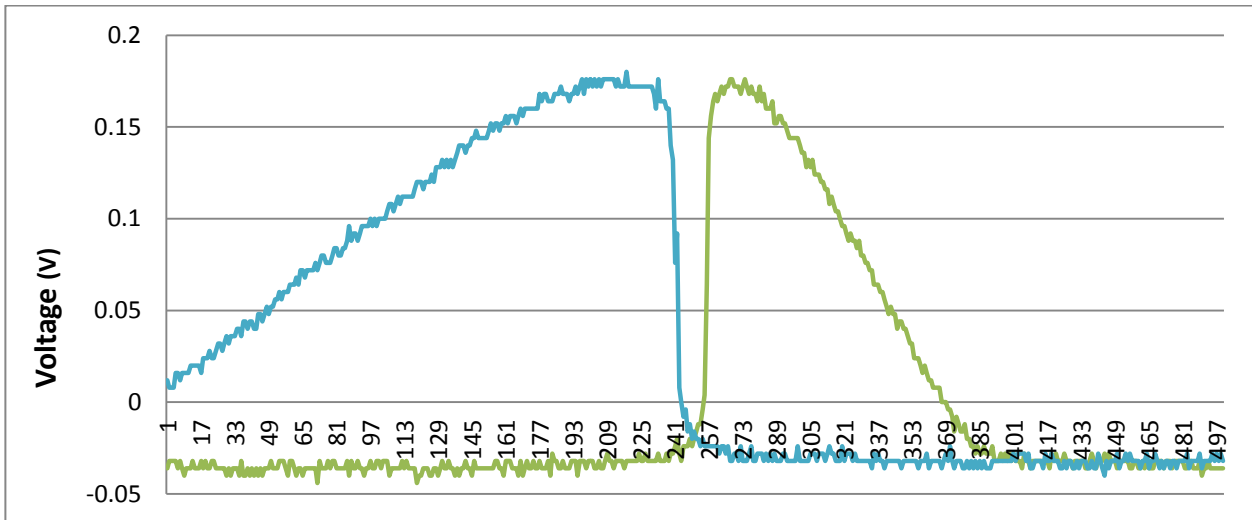


Figure 19: outputs from Lb (green) and Phib (blue) source modes on plotted oscilloscope (50ms/div).

The resulting calibrations proved to be useful, since as was suspected the preset custom settings by Magnicon were slightly off. Two of the bias values (Lb and Phib) needed small changes to their operation values for our system operate ideally. If you examine **Figure 19** you can see that the source modes input on the first two channels on the oscilloscope are not properly aligned horizontally with each other and the vertical segments parallel, all such that the curves bottom is at 0 V. After a few minor adjustments the ideal settings were achieved. With this final piece of equipment setup and everything calibrated a large number of testing that had been unavailable due to the shipping delay was then possible. All tests and results are discussed later in the results section.

Chapter 3: Digital Modeling

3.1 Model Design

The modeling of QCM systems was initiated by first studying an extremely useful model included by COMSOL in the software's "model library". In this library an extremely simplified example of a 5 MHz quartz oscillator as used in a number of electronics was found (as seen in **Figure 21** below), it provided a useful albeit exaggerated (exaggerated depiction of mechanical displacement for better visualization of the effect) example of the sort of shear thickness piezoelectric action seen in QCMs. Though this model is extremely small (1.6 mm in diameter) and idealized, it provided a useful starting point for the learning how the each of the COMSOL physics sections worked together, and through analysis of this simplified it became possible to expand upon the procedure to produce systems that more closely resemble the conditions of a QCM crystal. To produce these models it is important to make small yet distinct changes to the conditions of the model.

As discussed previously the models in Comsol are based on individual physics modules to solve various system phenomena under test. For these models there are model-level and domain-level equations being used, where the domain level equations describe the coupling between the strain and the electric field at a given point within the system and the model level equations describe the model level effects and interactions of each of the domains. The domain level relations used by Comsol for the piezoelectric interactions are the relations:

$$\mathbf{T} = \mathbf{c}_E \mathbf{S} + \mathbf{e}^T \mathbf{E} \quad \text{and} \quad \mathbf{D} = \mathbf{e} \mathbf{S} + \epsilon_s \mathbf{E} \quad \text{Eq 3}$$

Where, \mathbf{S} is the strain, \mathbf{T} is the stress, \mathbf{E} is the electric field, and \mathbf{D} is the electric displacement field in the domains. The other terms are material parameters stiffness (cE), the coupling matrix (e) and the permittivity (ϵS). These quantities are tensors of rank 4, 3, and 2 respectively, and are generally included in the database of properties for piezo-active materials represented as large matrices in Voigt notation. In addition to the piezoelectric equations, the equations of solid mechanics and electrostatics must also be solved within the material. The electrostatic equations describe how the scalar potential V is related to an electric field (\mathbf{E}) as $\mathbf{E} = -\nabla V$. and with Gauss's law gives the form Law Gauss' law, gives the form $-\nabla \cdot (\epsilon \nabla V) = \rho$. Where ϵ is the permittivity of the material and ρ is the space charge density given by either initial conditions or in our case modeled external circuitry for the system. The solid mechanics within the system are extremely simple and

related by the equation $-\nabla \cdot \rho = Fv$, where ρ is the density of the material and v is the Poisson's ratio. All of these relations are combined into the piezoelectric model as are each of these domains iterations (seen in figure) and these relations are applied to the system when being solved.

$$\begin{aligned} -\rho\omega^2\mathbf{u} - \nabla \cdot \boldsymbol{\sigma} &= Fve^{i\phi}, \quad \boldsymbol{\sigma} = \mathbf{s} \\ \nabla \cdot (\mathbf{D} + \mathbf{J}_i(i\omega)^{-1}) &= \rho_v \\ \mathbf{s} - \mathbf{s}_0 &= c_{\mathcal{E}} : (\boldsymbol{\epsilon} - \boldsymbol{\epsilon}_0) - \mathbf{e}^T \cdot \mathbf{E} \\ \mathbf{D} - \mathbf{D}_r &= \mathbf{e} : (\boldsymbol{\epsilon} - \boldsymbol{\epsilon}_0) + \boldsymbol{\epsilon}_S \cdot \mathbf{E} \\ \boldsymbol{\epsilon} &= \frac{1}{2} [(\nabla\mathbf{u})^T + \nabla\mathbf{u}] \\ \mathbf{E} &= -\nabla V \\ \boldsymbol{\epsilon}_S &= \boldsymbol{\epsilon}_{0,vac}\boldsymbol{\epsilon}_{rS} \end{aligned}$$

Figure 20: Equations given by Comsol's piezoelectric devices module for frequency domain operation

The first step in this process was to produce models with crystal sizes one might normally see in use. Accordingly the diameter of the model was changed in several separate models to reflect crystals of 0.25, 0.5 and 1 inch, while retaining all other property values for the system (quartz wafer thickness of 334 micrometers). The following figures represent the post-processed output of the simulation.

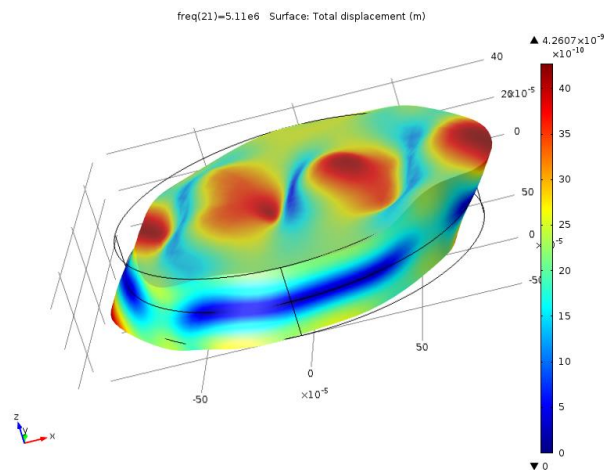


Figure 21: Original crystal oscillator model (displacement not to scale)

These three individual models were produced to ensure that when scaling along directions not associated with the shear wave's mode (z-direction) and holding thickness constant, any effects adverse or otherwise might be seen. These models despite a moderate decrease in the peak frequency (approx. 100 KHz when doubling the diameter) all act functionally identical, one of which can be seen below, and show that the displacement caused by the shear mode through the thickness of the crystal still acts as expected with a similar wave in the x-direction of the model causing the same wave type pattern seen before with the only differences being the number of "waves" coming about due to the increases in diameter and due to the original modal operating at a multi modal frequency which will be discussed later.

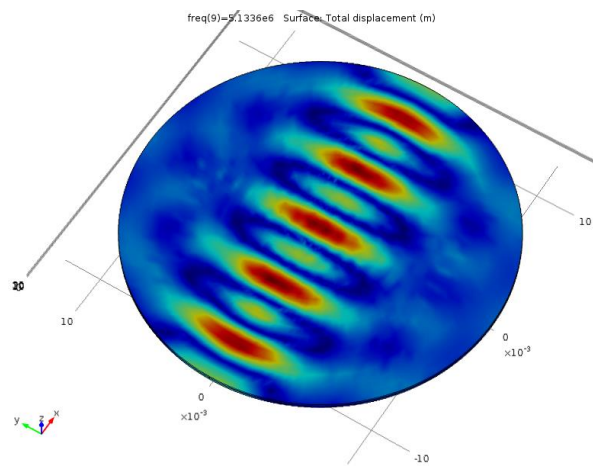


Figure 22: 1-inch scaled quartz oscillator

Once a solid understanding of the diameter scaling was gained, the next prudent step was to add the thin metal electrodes such as might be seen on real devices, but those were lacking on the included model to the surface of QCM oscillator model. To accomplish this, thin (250 nm) gold electrodes were added to the full surface of the top and bottom.

Although full surface electrode configuration is unlikely to be seen in actual systems, adding more complex configurations was deemed too large a departure for a single step. Since the implementation of these electrodes is meant to be a part of the system as a whole but not participate in any piezoelectric action. Comsol deals with these added masses by applying structural mechanics relations to that domain exclusively instead of the full set of equations. Giving the equation $-\nabla \cdot \sigma = \rho_V \omega^2 \mathbf{u}$ to represent the mechanical effects of this domain on the system, effectively allowing the material to apply its respective structurally resonant properties or lack

thereof to the system during operation. Despite the new changes to the model, it was quickly shown that COMSOL was capable of simulating the charge flow through materials not involved in the piezoelectric effect while being a part of the calculations for the governing electrical circuitry module (AC/DC module) and structural behavior. The slight increase in thickness in the z-direction from the gold electrodes results in slightly lower operation frequency as would be expected when considering the first Sauerbrey equation which directly relates the two values. After a bit of calculation based searching the wave form pattern displayed in the electrode-free oscillator were replaced with models operating at a more uniform full face single node displacement (1,1,1 modal) as is most commonly used with face shear AT-cut QCMs. ^[41]

After it was determined that there would be no simulation problems associated with adding non piezo-active materials into the electrical system, further tailoring of the modeling was continued. The goal was to shrink the overall size of the electrodes to a partial surface/centralized similar to something to that might be seen in real world examples including symmetrical and asymmetrical (top electrode larger than bottom) examples. The results obtained by this step are reasonably expected, as the shrinking of the electrode geometry results in a very obvious centralization of the piezoelectric effects seen, as well as some rather interesting changes in the distribution of charge over the course of each phase cycle.

The electrical potential distribution across the QCM is seen in **Figure 23** at resonance (~5MHz), with positive electrical potential being represented as red and negative potential as blue with the centers of the models showing a flat color due to it representing the peak, zero, or trough of the sine wave of the electrical driving signal during each moment captured. This sort of electrical potential cycling inside the crystal is seen only at resonance peaks as the maximum amount of power is passed through the system and is clearly related to the mechanical displacement happening at that frequency. As with the cycling the displacement seen in **Figure 24** which is quite high at peak resonance (on the order of 10^{-8} m) is essentially not seen at other frequencies.

*Since the models shown in the following figures are test models made during the modeling process they are not directly representative of any of the oscillators or QCMs tested and serve to help the reader visualize the phenomena being discussed.

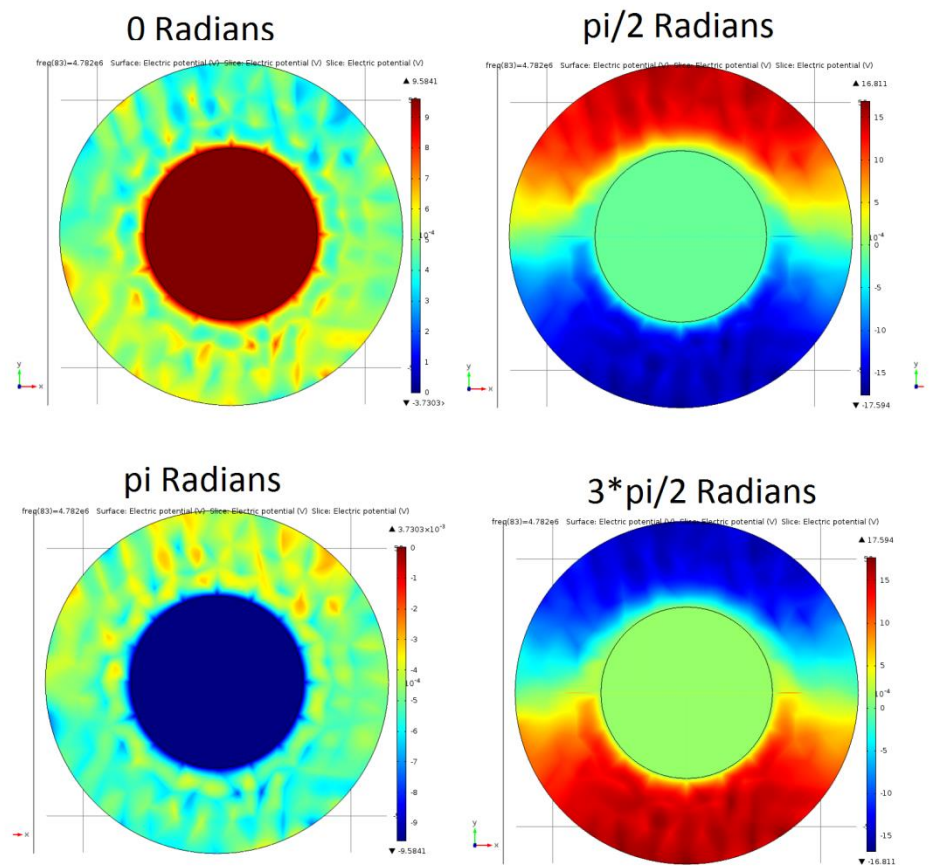


Figure 23: Changes in electrical potential with respect to Phase

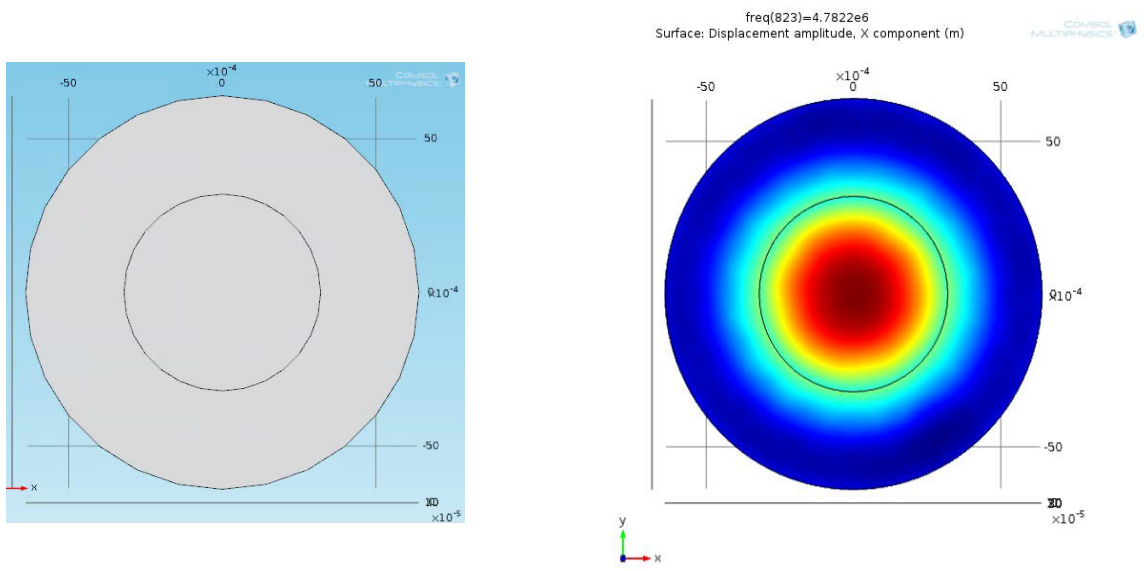


Figure 24: Partial electrode geometry and visualization of resulting displacement field distribution.

3.2 Model interpretation and Analysis

Basics properties at resonant peaks

With the reasonable approximation of a real world QCM successfully modeled as described above, it's possible to start full-scale analysis of operational results gained from the models of uncoated (operating without a sample to be measured) oscillators as a comparison to control values obtained by the oscillators in the lab. Since all later measures to be taken during actual experimentation with treated devices will be compared to the real world control values, it is important that similar model baseline values be analyzed for consistency with the real world controls. In this way we might reasonably compare models of treated devices to their real counterparts with some level of confidence, such that any differences between them might lead to useful insight and lend credibility to the end results.

First, since many small changes to the overall size and dimensions of the model were commonly made during modeling, it often became prudent to solve a small range of frequencies surrounding the anticipated/calculated resonance peak to ensure that the ideal values might always be found. This resulted in the extraction of several useful charts from the full simulation output, including responses such as plots of induced displacement fields and resulting instantaneous total displacements which are calculated with respect to frequency and electrical phase. Total displacement values are calculated assuming a zero displacement starting point and measuring the displacements produced by the incident displacement fields over the course of a single cycle. These types of plots are a quantitative description of the essential phenomena and lend a good counterpoint to the more qualitative 3-d images shown above. These plots lend considerable insight into these systems. A few of these figures are seen and described in further detail below:

From **Figure 25** it can be seen that the instantaneous displacement fields is dictated by the phase angle as might be expected since the QCM device completes a full forward and back displacement each cycle. While near the resonant peak, this phase relationship produces the largest displacement fields at a phase of $\pi/2$ and $3\pi/2$, and zero field at phases of 0 and π . At frequencies away from resonance this trend changes, producing reasonably large displacement fields at a phase of 0 and pi radians. This phenomenon prolongs the duration of each cycle where displacement fields are acting on the surface, effectively increasing the amount displacement field produced at frequencies other than the peak. This produces a lower displacement fields for a longer period of

each phase, effectively promoting changes toward the peak for frequencies between the secondary peaks frequency shown below.

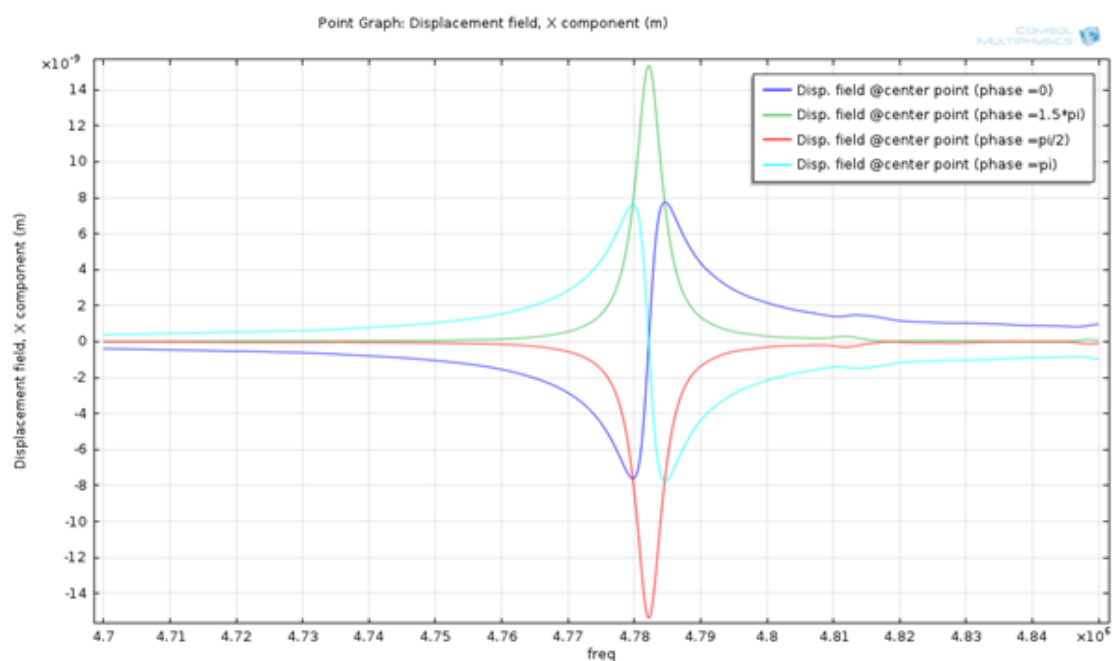


Figure 25: Displacement field at center point for important phases vs. frequency

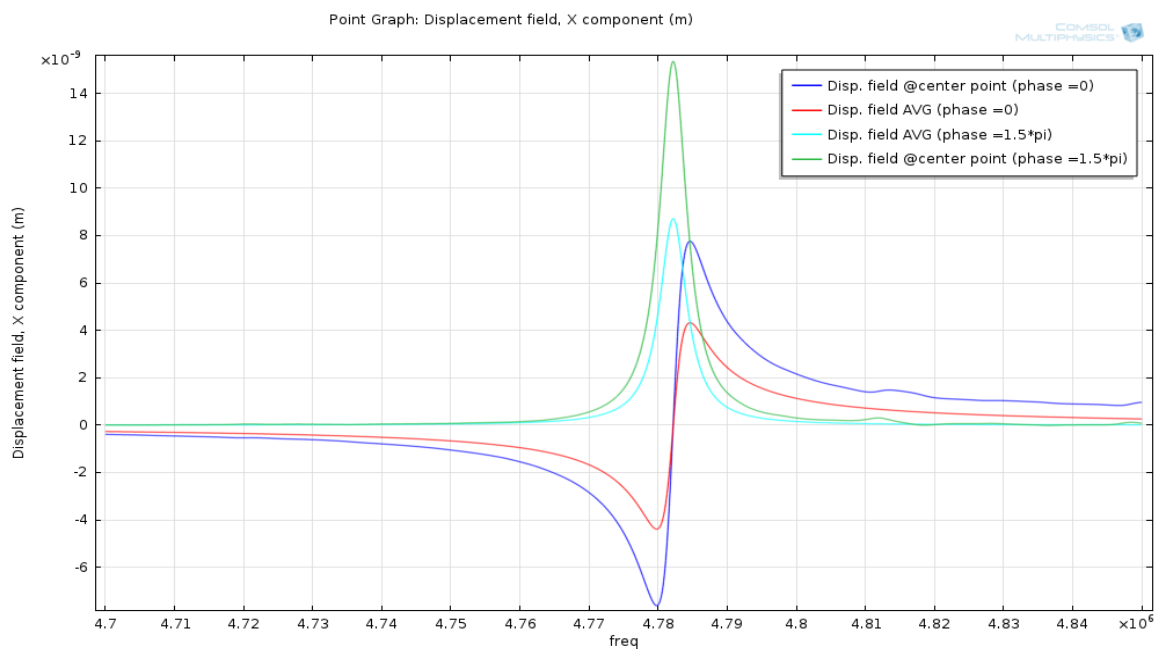


Figure 26: Displacement field at center-point / full electrode avg. for important phases vs. frequency

In the next figure (#27) as well as by referring to **Figure 24** it becomes apparent that the relative distribution of the displacement field effect and thus all the other piezoelectric effects is not spread evenly across the surface or even the electrode area. In fact values at the center point of a given side are more than double the average value of the entire area covered by the electrode (seen in **Figure 26**). This effect is something not seen in the full-surface electrode models which showed even distributions across the surface.

This centralization of the displacement fields to the area under the electrodes is almost certainly caused by a damping effect from the non-energized bare crystal that surrounds the electrodes. This effect is seen in real world QCMs as well, and is likely done purposefully due to the necessity of mounting the crystal in such a manner that the mounting might have a minimal effect on the resonance. By mounting the crystals along its edges with partial electrodes the mount would see considerably less resonance from the crystal and likewise have a lower overall effect on the system. In the case of **Figure 27**, you can see the basic profile of the displacement field in the x direction vs. the x coordinate at which the measure is taken for a mounted and non-mounted model. The model was “mounted” by assigning a zero displacement boundary condition for each end of the mounted crystal on the x-axis.

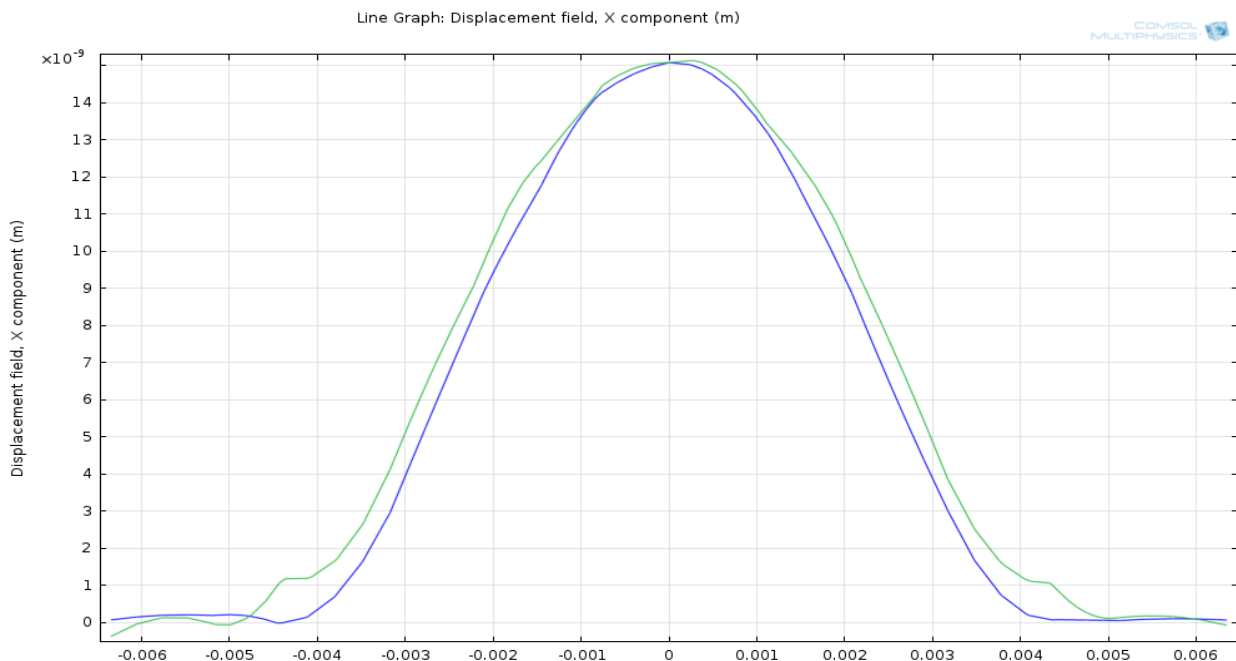


Figure 27: Displacement field in the X-direction vs. coordinate in the x, mounted (green) vs. non-mounted

The general distribution being discussed can be seen in **Figure 27** as well as the effect of mounting the crystal along its sides as is most commonly seen in quartz resonators. Discounting relatively minor deviations induced in the x-directional displacement field, there is high similarity between the two indicating little effect from the mount. The only major differences in the graphs are a sort of plateau type aberration (seen @ approx. .0045 on both sides) beyond the area that would be covered by the electrode (-.003 to +.003) but not quite to the edge of the crystal, it seems safe to assume clear that this effect is most likely produced by some sort of reverberation of the displacement motion wave off the mount causing destructive interference with the next induced displacement creating a standing wave type effect. The plot of these changes shows that despite a region of low motion along the outside of the crystal that bracing the system still produces noticeable deviations from ideal behavior. The significance of the difference between mounted and unmounted is arguable, but this difference which is never larger than ~7% of the peak displacement field magnitude is something that can be accounted for when comparing between modeling and real result. Additionally 7% isn't large enough to affect the main purpose of the model, which has always been to serve to give visualization to the system as well as serve as a sanity check to compare results.

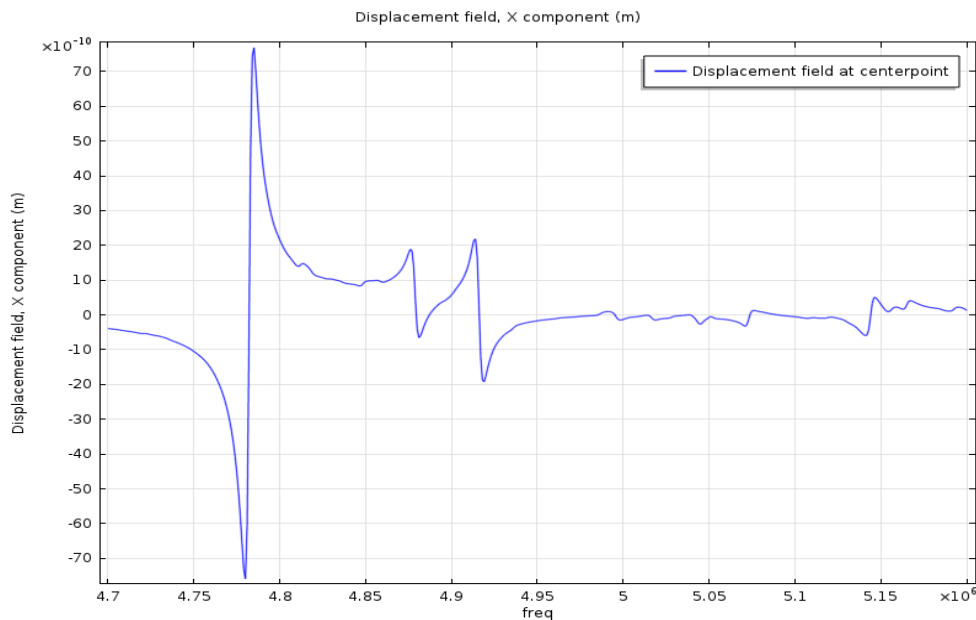


Figure 28: Displacement field vs. frequency at sensor center

When examining the response of the system outside of the peak frequency several other local extrema in the displacement vs. frequency plots can be seen in **Figure 28**. These local extrema (seen at approx. 4.88 and 4.92 MHz respectively), though considerably lower in magnitude (producing only about 25% the value of the first peak), represent the modes with 3-nodal resonance in the x (1,1,3 mode in **Figure 29**) and y (1,3,1 mode in **Figure 30**) direction and are followed by resonant peaks of increasingly high number of nodes at lower displacement values.^[41] As can be seen with the 3-nodal mode shown below, there is a similar centralization of effect and when the displacement is plotted on a coordinate graph the also show the symmetry seen above. The difference between these two similar 3-nodal modes is subtle but a subtle stretching in the x direction of the models produces different effects between the node orientations. This effect is more clearly seen in the graphs which show that the width of the central node is considerable less than in the other pattern.

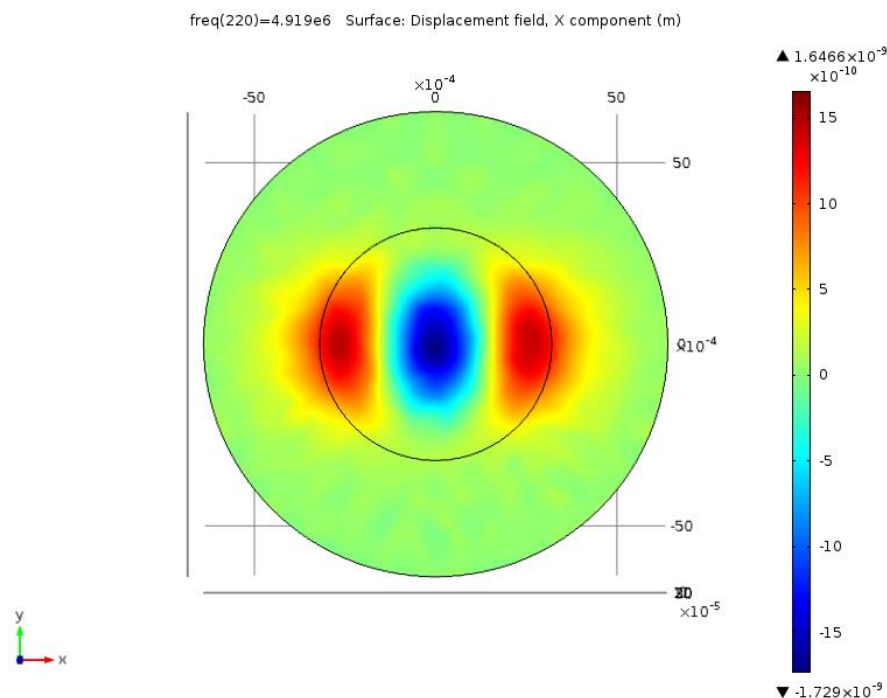


Figure 29: 3-nodal(x) operation

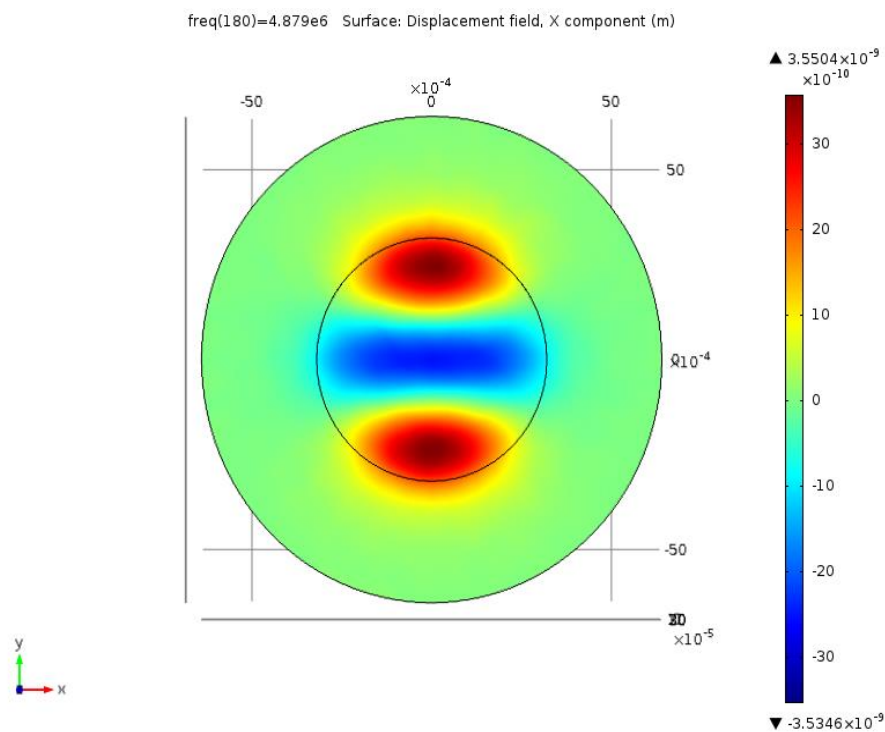


Figure 30: 3-nodal(y) operation

Occasionally these multimodal operational states may have additional benefits or unique measurements depending on the desired application, but are not used in most applications as the determining the local behavior of the higher mode regimes becomes extremely complicated, and the power return becomes quite low leading to ever higher signal to noise values. A number of plots have been made for several interesting multimodal QCM states found using the model, and are included in Appendix B along with other relevant figures.

3.3 Effects of Variations in Driving Circuit and Signal

To further understand the effects of systemic variables on the QCM system a number of additional simulations were conducted to illuminate the relationship between the electrical sources powering a QCM device and the resulting mechanical response. Accordingly a few iterations of modeling were performed whilst making simple changes to the electrical system to collect data on the effect that these values would have on a system. The first of these was a simple iteration of the previous model varying the source voltage and finding the resulting effects on the system. As can be readily seen from **Figure 31** below, as the voltage through the system increases, the magnitude of the

displacement field increases linearly. Upon close examination the increases in magnitude are quite regular and indeed should the magnitude of the displacement at the resonant peak be plotted vs. the voltage it is shown to be exactly linear across a large range of voltages. This direct sort of correlation is not unexpected by any means, but instead is rather encouraging as definitive evidence of linear relationship between electrical and mechanical properties gives hope that simple yet rigorous analytical model might be found, providing greater understanding of the system. Extrapolating from these electrical results it seems evident that the voltage and current through the QCM would both scale linearly with the input as well.

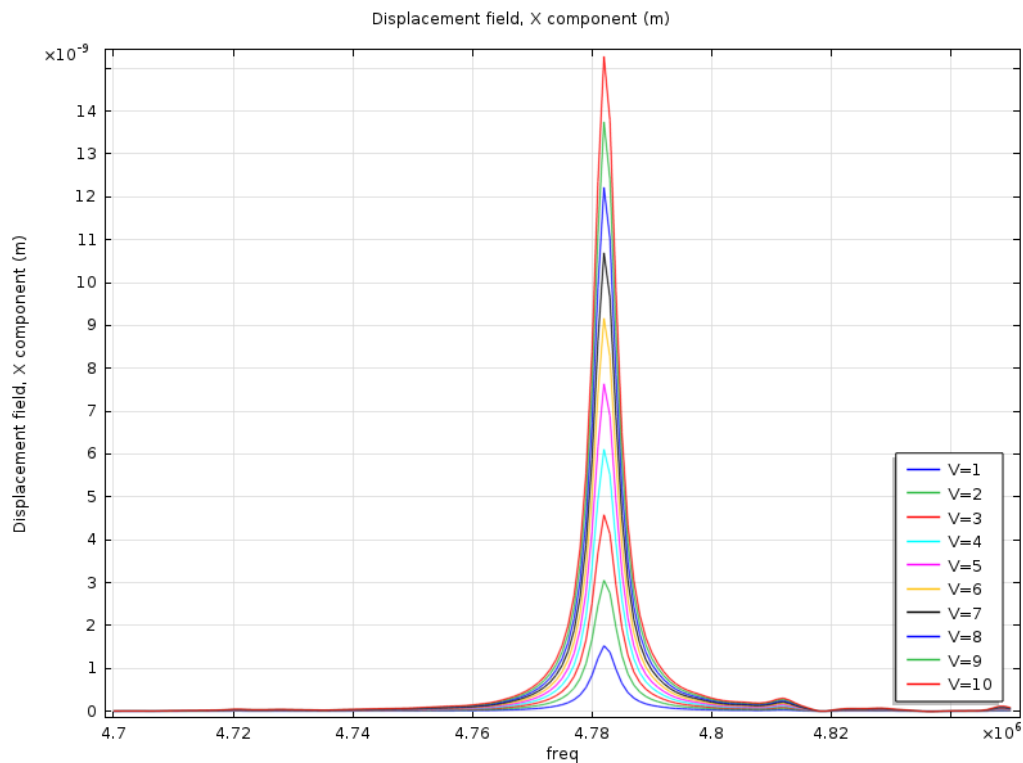


Figure 31: Peak displacement vs. applied voltage

In addition to the voltage vs. displacement models it seemed prudent to investigate other features of the electrical system being modeled around the QCM itself by the COMSOL program, chief among these is the inclusion of a series capacitor in line with QCM itself in a manner similar to

the **Figure 32** shown below. This is not something done in a general QCM system but was a relic of the initial source Comsol model, obtained from the COMSOL model library. In the brief description^[37] of said model little to no information was given on the reason for its inclusion other than that “captures the charge generated by the circuit”. Accordingly the effect of the designated capacitance on the operation of the QCM was investigated.

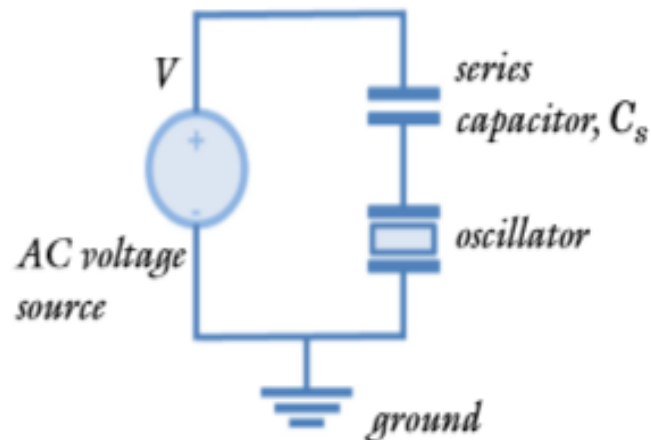


Figure 32: External circuit for COMSOL model

The results of that investigation show some rather curious effects associated with shifting capacitance values. Firstly the capacitor was removed entirely, and it was seen to increase the magnitude of the mechanical displacement field without any other noticeable effect. With the capacitor in place and varying the capacitance you see the same variation in magnitude trending downwards with lower capacitance, which is to be expected since there would be a corresponding change in the voltage delivered to the QCM at any given time and that is in fact the effect on the system you see associated with a voltage change in the driving signal.

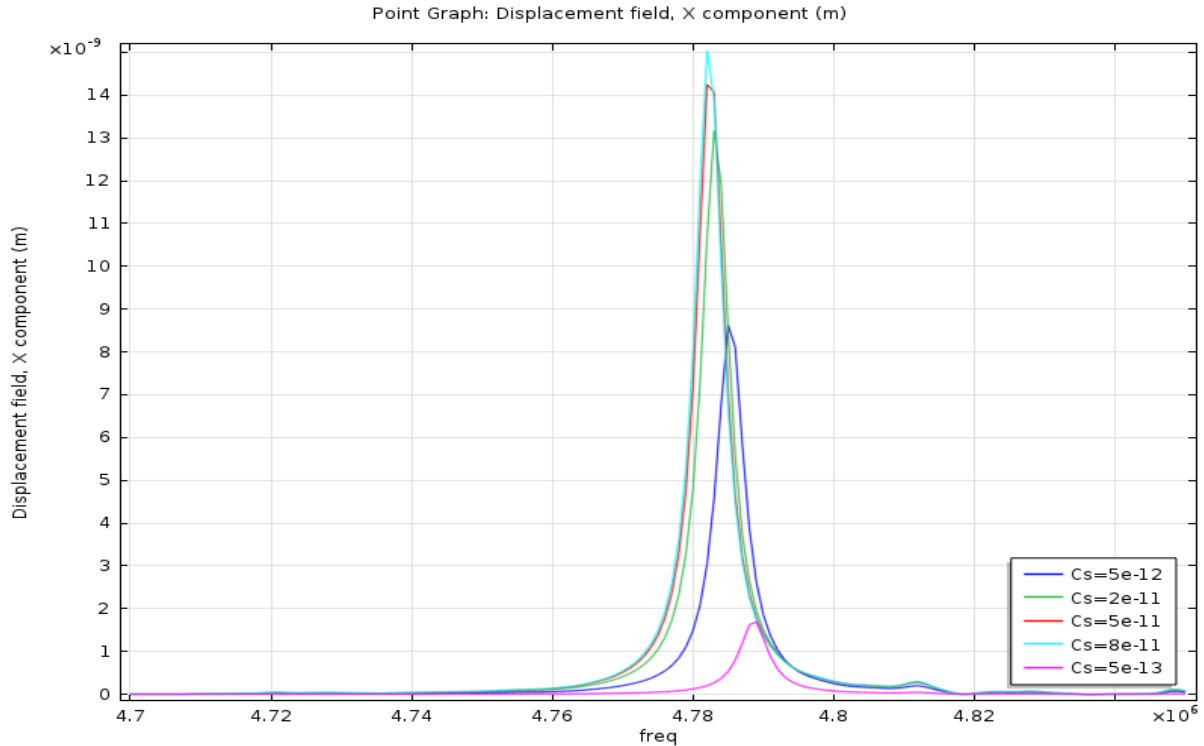


Figure 33: Peak displacement of various Cs values vs. frequency.

Unlike the variation of voltage, it can be seen that when the peak displacement field at each capacitance is plotted against the capacitance its relationship is considerably logarithmic in shape as can be seen in **Figure 33 and 34**. This is due to the impedance of a capacitor being $\frac{1}{\omega C}$ meaning a lower capacitance will directly reduce the power reaching the QCM sensor to produce displacement, leading to this nonlinear trend.^[38] A secondary effect seems to include the shifting of the resonant peak to higher frequency values as the capacitance decreases. Given the lack of sufficient electrical engineering knowledge to reliably explain this particular phenomenon and since this value has shown itself to have a large impact on the system, the capacitance was set to specifications for load capacitance provided by the QCM device's manufacturer such that the model would reliably match the model despite the lack of explanation for the effects.

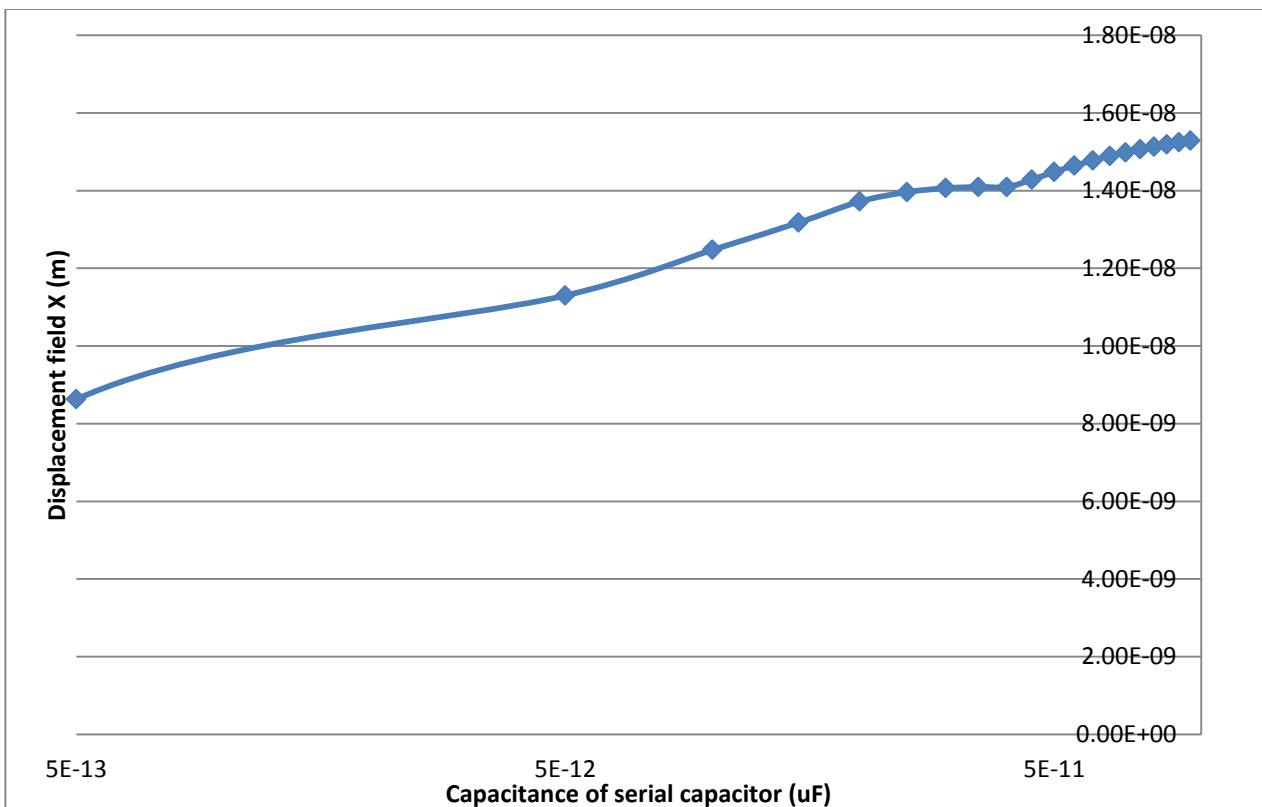


Figure 34: Peak displacement vs. capacitance

These variations in both electrical configuration and driving properties in the model have clearly shown themselves to be important criterion for determining the output of the system. This being the case, great care was taken to base the model on its real world counterparts during each test in order to make projections that appropriate comparisons for the measurable results. The final values of these properties will be discussed in depth when comparing these two in the results section of this paper. Additionally models for a large number of tests including QCM operation in water and will be compared to the real world test results as each is discussed below.

3.4 Effects of Operation in Water Based Testing Environments

Towards the end of this project some effort was put into getting similar electrical data for operation of QCM systems in the kind of environments that QCMs have seen the most recent application, namely water and aqueous based testing from the biomedical field. To accomplish this a few new models were needed to recreate similar conditions. Firstly by partially covering a single surface to recreate the conditions of water cell based testing (reference **Figures 48-50** in the results

section) the by applying water to the entire single surface to simulate the application of water onto a bare QCM, and finally making a large water domain that entirely surrounds the QCM model to simulate a submerged QCM. These models required the addition of a Fluid structure interaction module solved simultaneously to simulate properly, and had a large number of geometry issues with the solver. Needless to say these models also took a great deal longer to simulate than the previous models and in the case of the submerged model utilized 6-fold more elements.

To create these models water was added in cylindrical domains, to facilitate the use of a swept meshing mode to cut down on the number of corner and border elements needed. While this is a reasonable representation of the water-cell/partial water coverage operation seen in **Figures 35 and 49**, it only approximates the more complicated hemispherical geometry observed in the water in the “water atop a bare QCM” testing due to water’s surface tension effects, the model itself can be seen in **Figure 65**. These models were quite simple in comparison to the submerged model however, which due to Comsol’s solver’s reluctance to solve domains that had interactions with multiple sides of the QCM device (even having a distinction between the electrode and the rest of the top of the device) required the additional of 4 additional domains to then all be modeled as water. A visualization of this model can be seen in **Figure 37**.

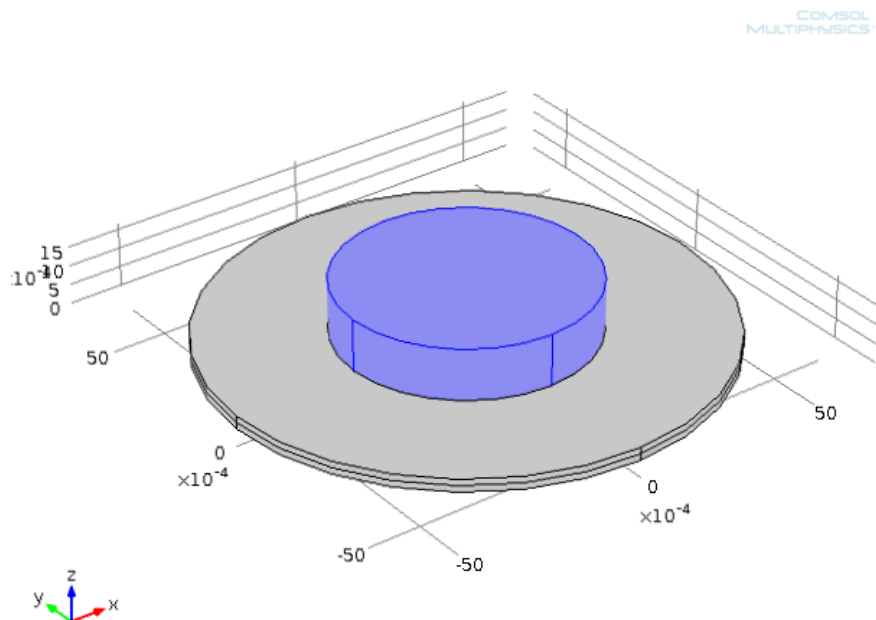


Figure 35: Water (blue) as seen atop QCM that is enclosed in a cell

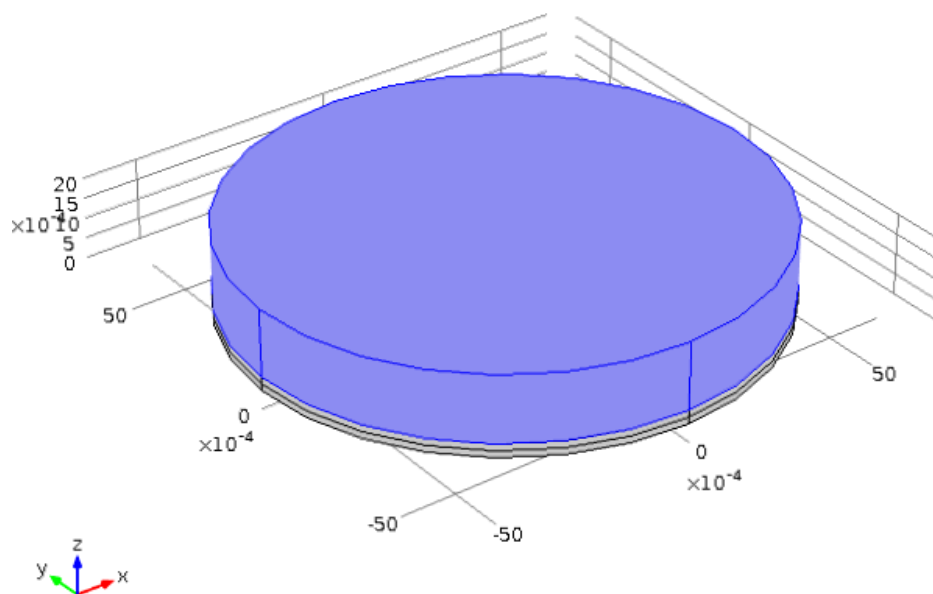


Figure 36: Full surface water (blue) coverage approximation

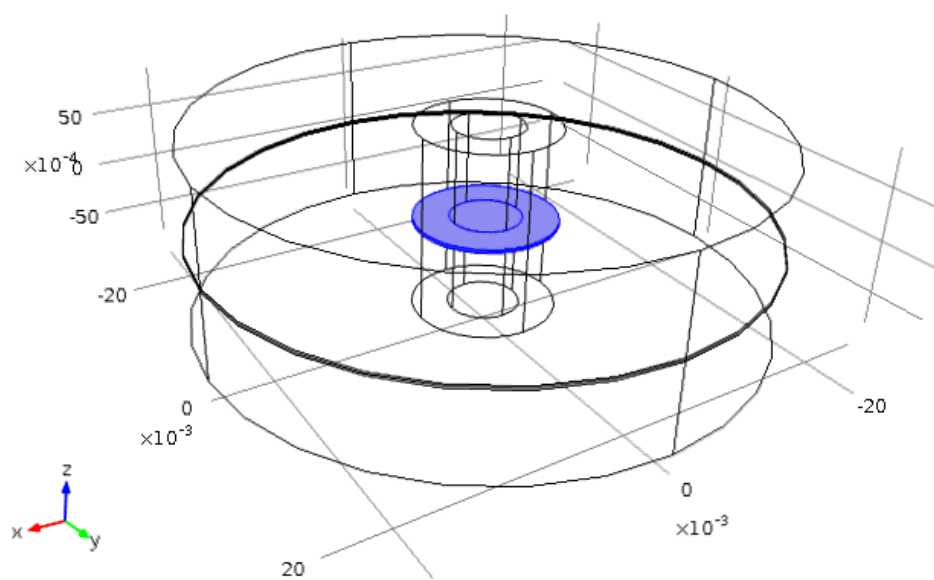


Figure 37: Visualization of “submerged” QCM, water domains are transparent, quartz and gold (QCM) domains in blue.

Once the models were created and would solve properly in the COMSOL modeling environment calculations were performed to estimate their operational frequency regimes while loaded with water enabling us to take the same frequency response data collected for the other models and discussed in the results section.

Chapter 4: Results

4.1 Frequency Response Analysis (FRA)

Analysis of common oscillators

All FRA tests were performed on a common set of crystal oscillators to increase the generalizability of the results and also served the purpose of testing the efficacy of our measurement techniques, while allowing any last minute adjustments that were necessary. This set of mounted and sealed commercial oscillators ranged in frequency from 5 KHz to 5MHz including multiple oscillators at several frequencies where a variety of different oscillators were readily available. These oscillators were the first thing tested and provided the baseline for further studies in which the sensor environment is variable. For these relatively short measurements, temperature control outside of the laboratory HVAC facilities was not found to be required.

To start off the testing, a basic frequency response analysis (FRA) was performed on each of the oscillators. These results are similar to **Figures 17, 18** from Chapter 2 and you can see an example of the output below and the rest of the output in Appendix A. This includes FRA data for the 5.8 KHz oscillator which shows a FRA response with an extremely noisy signal, and was not used in subsequent data analysis. The noise in the signal is likely due to a large amount of signal reflection but may be the fault of the some of the equipment's ability to measure the rather low frequency oscillator, specifically the vector voltmeter which refused to produce any voltage measurements for that oscillator.

The goal of these tests was to provide peak resonant frequency information for each oscillator (blue line) as would normally be collected during measurement of the average QCM device. This is important not only as the values are necessary for comparison for later data but also because it gives us a good idea of what can be expected for the manufacturing tolerances. The tolerances become visible when aggregating the peak frequency values from the absolute power data and comparing it to the intended operational frequency as can be seen in Table 1. Since these common oscillators come from a variety of manufacturers and come in various varieties, instead of model numbers this table includes a simple description of each oscillator. (Large means the oscillator is approximately 1"x1", and small being approximately 0.25"x 0.25", see **Figure 16** for more information)

Table 1: Frequency tolerance of common oscillators

Oscillator Nominal Frequency	Oscillator Description	Actual Frequency (Hz)	Percentage Difference
5 MHz	Small	4,998,300	-0.03400%
	Large, open case	4,994,125	-0.11750%
	Large, sealed case	4,997,877	-0.04246%
4 MHz	Small	3,999,979	-0.00053%
3 MHz	Large, glass case	2,999,992	-0.00027%
	Small	3,000,015	0.00050%
2 MHz	Large	1,999,992	-0.00040%
1 MHz	Large	1,000,010	0.00100%
100kHz	Large	99,928	0.07200%
5.8174 kHz	Large, double tall	5,815.25	0.03696%
Average tolerances	-	-	-0.00847%

Another key measure derived from this data is the peak dispersion values, or how wide and spread out the peaks are. This value is found by taking a full width half-max measure for the power ratio. Larger values of this measure are generally indicative of larger amounts of dampening caused the oscillator's case and environment, leading to a broad or "muddled" peak instead of a single sharp resonant peak.

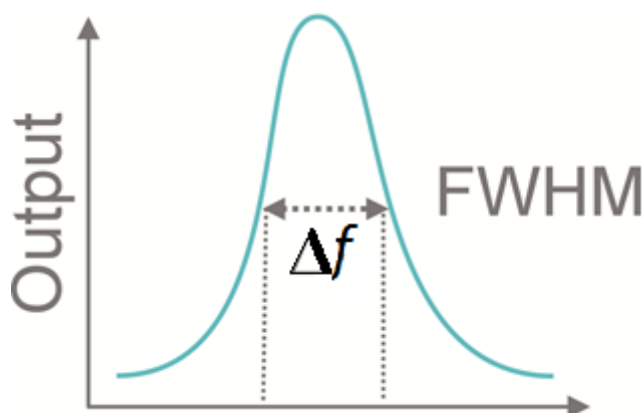


Figure 38: Simplified Full width half max measurement illustration.

In fact, this dampening or dissipation is a key limit for measuring thick, viscoelastic films. A sharp resonant peak is essential when the QCM sensor is incorporated into a basic oscillator circuit. If the peak is too broad, the circuit never locks on to the resonant peak, and there is no data to collect. A second way to discuss the sharpness of the peak is the quality factor, Q , (peak frequency / halfmax spread) which should be at least 1000 for the oscillator to lock properly. In this context the

dissipation, D , is given by $1/Q$, and is used extensively in the discussion of QCM of soft films in liquid environments.^[43]

Table 2 below shows all these data as well as a ratio of spread vs. frequency of operation, such that the different oscillators might be compared. This data is particularly useful as it gives a theoretical limit to the prediction power of the data taken from the common oscillators when using them for comparison purposes.

Table 2: Peak spread of common oscillators

Oscillator Nominal Frequency	Actual Frequency (Hz)	Power Ratio halfmax Spread (Hz)	Dissipation (D)	Q factor
5 MHz	4,998,300	2150	0.000430	2324.79
	4,994,125	2450	0.000490	2038.42
	4,997,877	2460	0.000492	2031.66
4 MHz	3,999,979	800	0.000200	4999.97
3 MHz	2,999,992	585	0.000195	5128.19
	3,000,015	1075	0.000358	2790.71
2 MHz	1,999,992	306	0.000153	6535.92
1 MHz	1,000,010	133	0.000132	7518.87
100kHz	99,928	45	0.000450	2220.62
5.8174 kHz	5,815.25	1.175	0.000202	4949.15
Average tolerances	-		0.000311	3215.43

Since there are two frequencies where a few different common oscillators were available for testing of each. It is possible to see from this data that neither important measure (deviation % and spread ratio) show any strong relation to the size of the oscillator though the sample size isn't large enough to say for certain. This is an important point, since there are few trends visible when examining the electrical data discussed later. What is apparent however is that the two values (peak deviation and peak spread) seem to contribute to each other in some manner, even having a fairly strong correlation considering the large variety of oscillators.

What is also clear is that while the frequency tolerance percentage varies quite a bit over several orders of magnitude (.1-.0001%), the spread/ frequency ratio is much more consistent. This indicates that despite any cross contribution between the two that the tolerances on the casing and

environment are likely much more tolerant to small differences than the growing/cutting/shaping process involved in the quartz crystal itself. Regardless, the FRA data itself provides no direct prediction model possibilities but does provide necessary insight to create the model in the next section.

SQUID Linearization

With all the equipment fully set up and calibrated for proper functioning, it was still necessary to ensure linear response of the SQUID's output with respect to the input voltage for the range of voltages that would be applied. This range started at 100 microvolts and initially extended up to about 100 mV peak (70.7 mV rms) since there are concerns over damaging the oscillator at higher of voltages. During operation the SQUID acts much like a current to voltage transformer passing the test signals through a 10 kΩ dummy resistor to the SQUID's feedback coil so that it could be measured by the superconducting loop which produces a proportional response. What is needed a correlation to find the exact output voltage for a given current measurement (due to its various electrical biases and internal resistances necessary to properly calibrate the SQUID).

Therefore, data were taken to determine the correlation between reported power from the SQUID and the current delivered through the SQUID. Accordingly a few iterations of testing were performed at a variety of frequencies correlating to the nominal frequencies of each common oscillator crystal and at various input voltages, spread across the likely operational zone from the lower detection boundary of our voltmeters up to the maximum safe operational voltages for the crystal. The value of -20 dBm is specifically included as a convenient comparison because that was the input power used during FRA measurements. (See previous results subsection) These tests were run by removing the oscillator from the circuit and directly powering the SQUID's sensing feedback loop using the VSA at precise frequency and voltages (verified by voltmeters) and the response measured by attaching the

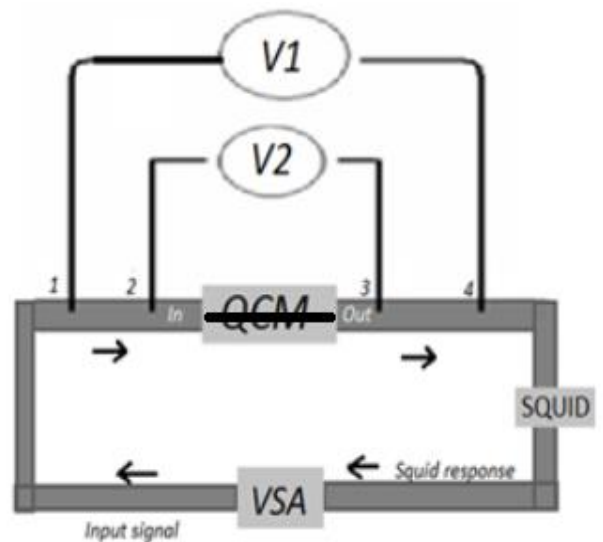


Figure 39: Illustration of SQUID linearization setup

response to the VSA's input channel. Using the redundant measurements taken of the input signal (in dBm) it is relatively easy to obtain a voltage value for the signal given that $P (W) = 10^{((P_{dBm}) - 30)/10}$, i.e. A Power ratio of -20 dBm would be $P (W) = 10^{((-20 - 30)/10)} = 10 \mu W$. With known power being delivered and a known resistances in the circuit finding the voltage or current being delivered is trivial given the Ampere's law in the following forms $P = I^2 * R$ and $P = V^2 / R$. With these a reasonable measure of the current delivery to the squid can be determined for use in calibrate the SQUID. A simple visualization of the test setup is shown in **Figure 39**. Accordingly it was recorded in the VSA's standard frequency based x-axis format. A graph of the output for one of the 5 MHz crystals is shown below in **Figure 40**, with a data table containing the peak data collected from each of the test for use in linearization in Appendix C.

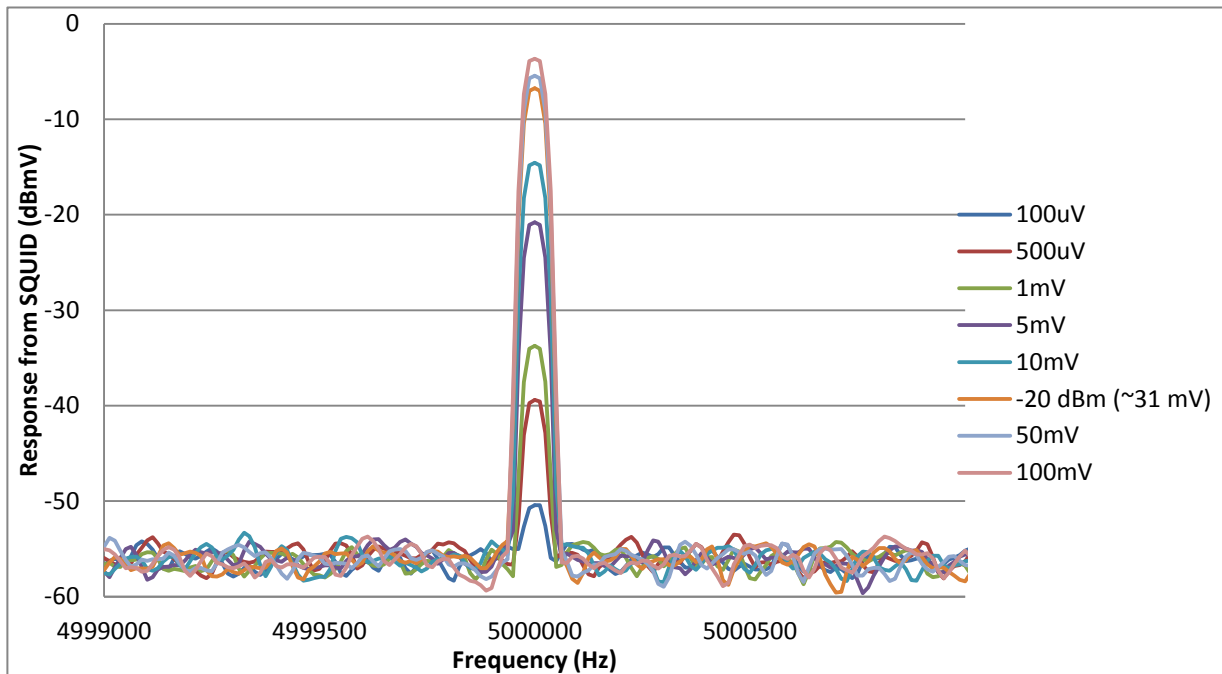


Figure 40: SQUID output voltages as measured by a VSA.

Due to this application of SQUID technology being extremely novel, little to no information was available to help determine what if any relevant information about the SQUID might be garnered as to what the shape of and distribution of the SQUID output peaks might contain. However the desired information was provided by the peaks themselves. When the peak maxima are plotted against the input current as in **Figure 41** you can see the linear increase in voltage output by the SQUID as a result of the increase of power being delivered through the system. This linear trend is

steady through several orders of magnitude up until -20 dBm where the trend flattens in the horizontal. Since over-volting crystal oscillators in extreme cases can lead to fracturing of the crystal due to the internal stresses involved, (which is why the data was limited to 100mV initially) and the SQUID stops operating linearly just short of this value, to simplify the linearization process only power values up to -20 dBm were used. After data collection was completed it became apparent that the data provided by the 5.18 KHz oscillator provided extremely inconsistent data with an extremely poor fit when compared to the trend line data of the other oscillators. This inconsistent data could be due to a number of factors, but is almost certainly exacerbated by the designed operational regime for the SQUID being 5 MHz range far away from the 5.18 KHz used during that oscillator's tests. Seeing how poor this data fit to the rest of the data and considering that QCM operation in the KHz regime is extremely unlikely it was decided to remove this data from the correlation. Discounting those fringe high power results, and the extremely noisy and unserviceable 5.8 KHz data provides a much clearer relationship between the voltage output from the SQUID and the current it is being fed.

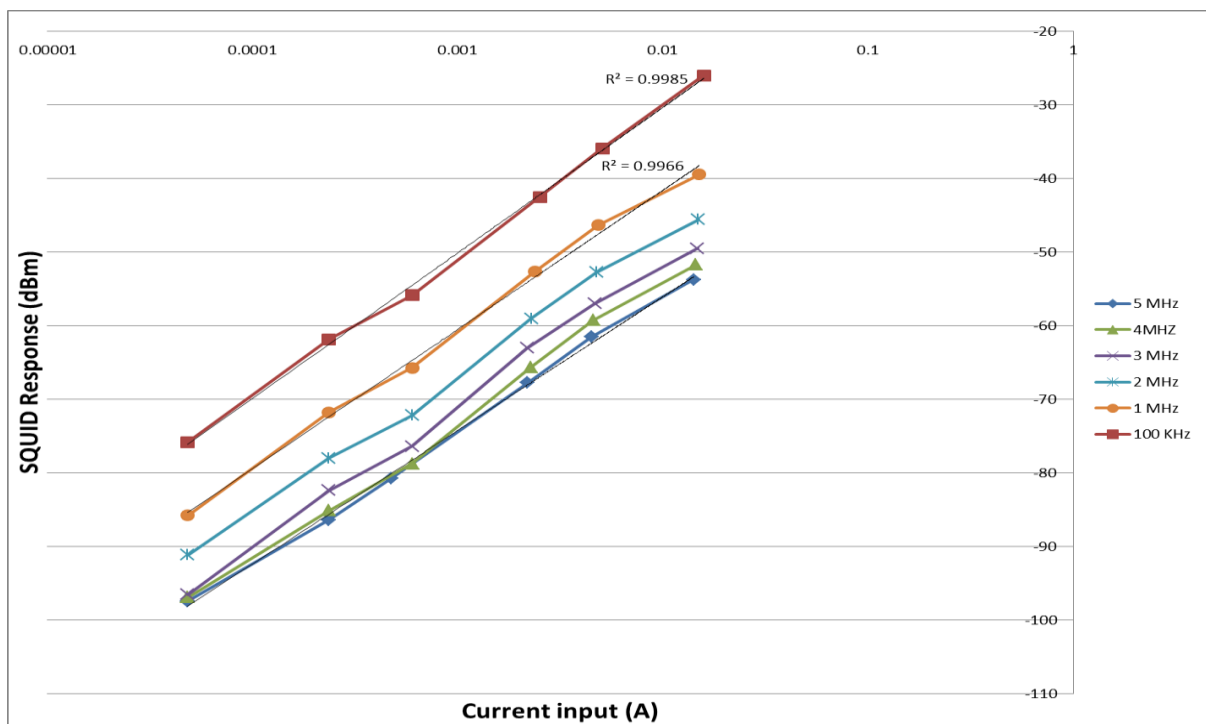


Figure 41: SQUID output vs. input current signal

Table 3: Trend line data for Figure 38

Frequency of operation	Factor(a)	Exponent(b)	R ²
100 KHz	0.0128	0.1171	0.9942
1 MHz	0.0528	0.1208	0.992
2 MHz	0.112	0.1213	0.9963
3 MHz	0.1397	0.1173	0.9889
4 MHz	0.2193	0.1201	0.989
5 MHz	0.3068	0.1249	0.9976

With a considerable amount of time and effort going into streamlining the recording of data, it seemed prudent to take these data and form a predictor equation to verify the validity of future data rather than trying to rectify the accuracy of the data with a large table or graph. Since a large number of measures are taken in dBm, trend data was formatted in a current vs. dBm (current values by ohms law, input voltage /50 ohms) arrangement instead of the current vs. dBmV shown in **Figure 41**. Examining the trend line data from the squid linearization in **Table 3** (which takes the form $y=a*e^{(b*x)}$), it can be seen that although the exponent (b) is unrelated to the frequency of the input signal is signal there is some contribution in the front term (a). therefor the equation produced to describe the SQUID's behavior is in terms of power in dBm and frequency in Hz is:

$$\text{Current} = (6E-08 *(freq.) - 0.0053)*e^{\wedge (0.1192 *(SQUID output))} \quad \text{(Eq. 4)}$$

This equation can of course be converted into an equation for voltage if necessary by simply applying ohms law with the impedance of the system set at 50 ohms. It could also be converted to an equation for power should the input power be required, however most of that data will be collected during measurement. Due to the model being based on trends with an R² values less than 1, the model is not a perfect fit but serves to predict output voltage values given the corresponding current inputs from the source data with accuracy greater than 98% in all trial cases. It's difficult to say for certain what the accuracy will be for measurement but it should be close to this value. It should be stated here that for future current testing using the SQUID that this relationship should be

considered to have and insufficient quantity of data points (with this trend data consisting of approximately 75 individual points, numbers of at least 3 times as many are recommended) likely leading to the somewhat low R^2 values during the trend line fitting. Collecting additional data points would likely have increased the accuracy of the equation in this case however the brevity of the measurement window for using liquid helium led to this discovery too late to make a changes to that. Regardless, further research and data collection in this area is certainly warranted.

Four-Point Probe Tests

Once the final preparation step for the SQUID was completed it became possible to perform the main round of testing for the common oscillators. This testing took the form of taking the FRA and SQUID linearization data to operate each oscillator at its resonant frequency while collecting the resulting electrical data. The results produced are the power output from the SQUID which gives the subsequent current values, and the voltages collected by the voltmeters to determine values such as voltage drop across the oscillator and the potential that remains.

The SQUID output/current information is provided in a similar manner as in the linearization step, with the key difference being the inclusion of the oscillators between the VSA and the SQUID as shown in **Figure 42**. With the SQUID and voltmeter operating in the 4-point probe configuration, a -20 dBm sine wave was generated by the VSA, as used in the FRA steps and included in the linearization. The resulting data provided by Table 4, and includes the voltage drop (difference between measurement points 1/4 and 2/3) across each oscillator as well as the voltage potential after the crystal (Voltage at point 3 and 4). The table also includes current measures from the SQUID as well as values calculated from power data from previous FRA data (for comparison) for each of the common.

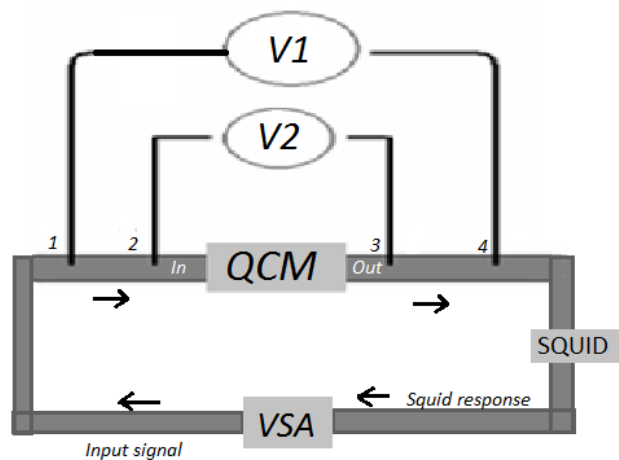


Figure 42: Illustration of test setup used for oscillator and QCM measurements.

Table 4: Voltage and current measurement data for common oscillators.

Oscillator Info		Voltmeter Measurement (mV rms)		Current Throughput (mA)	
Nominal Frequency	Description	Voltage Drop	Voltage after Osc.	VSA Measurement	SQUID Measurement
5 MHz	Small	11.714	18.449	0.320	0.377
	Large, open case	3.716	22.105	0.386	0.465
	Large, sealed case	8.165	19.792	0.342	0.406
4 MHz	Small	16.629	17.021	0.303	0.326
3 MHz	Large, glass case	2.399	22.776	0.405	0.461
	Small	26.696	9.988	0.178	0.191
2 MHz	Large	16.252	16.449	0.308	0.313
1 MHz	Large	30.295	8.112	0.151	0.163
100khz	Large	45.074	2.185	0.032	0.040

When examining the previous table, the first thing that is noticed is the large variances in the voltage drop / voltage throughput and current data, including values seemingly greater than the voltage provided to the system itself (22mV rms). This large potential drop is the result of a signal reflection and interference occurring in some of the lower frequency and smaller sized crystals. This reflection is generally caused by poor crystal quality causing ringing (or peak frequency ripple) that prevents the oscillator from settling into its fundamental resonant mode. [39] As might be imagined, this causes a good deal of noise in the electrical environment and this reflection effect cause too much noise in FRA data because the large amount of reflection caused a large signal to noise ration across the entire sweep, which is a large reason why the 5.8 KHz oscillator it was rejected for continued analysis.

The second thing noticed in this table is the current portion, in which it is clear that the VSA calculated data derived from the FRA is at all measures less in magnitude then the measurements taken by the SQUID, where the values from the VSA fairly consistently ~85% those taken via SQUID . This is difference was expected between common current measurement systems and the SQUID due to the resistance added to the line necessary for most instruments to take the measurement causes a voltage drop in the circuit. This error caused by the decrease between the measured current and the actual current at low amperages is the reason the SQUID was initially added to this project initially.

This increased accuracy will be extremely important as there are few external checks when relating the data to the digital models.

Comparison to Digital Models

Utilizing the digital models created previously and adjusting the specific parameters to match the individual oscillators being tested, including dimensions and electrical driving voltage, the digital results can be directly compared to the recorded electrical data results as in **Table 5**.

Table 5: Real data vs. digital model

Nominal Frequency	Description	Current (mA)	
		Measured SQUID	Model
5 MHz	Small	0.377	0.443
	Large, sealed	0.406	0.447
5 MHz	Small	0.326	0.432
3 MHz	Large	0.461	0.445
2 MHz	Large	0.313	0.440
1 MHz	Large	0.163	0.447

It is apparent from this table that although the digital models do a reasonable job of predicting behavior in the higher quality oscillators, specifically the ones with the lower voltage drops during testing. However, since the model does not account for the non-ideal electrical behavior exhibited by the smaller and lower frequency crystals, and fails to adjust for the reflection effects in the system, instead giving predictions for the crystal as if it were acting ideally. Accordingly it predicts ideal transmission through the crystal which is quite different from the reality. This may be something that be corrected for, either in the models external circuitry that is being simulated or when analyzing the results of later investigations.

However given that reproducing the basic properties of each oscillator in in model form able to produce results reasonably close to the measurements taken by the instruments (as shown by table 5). Even despite a number of unavoidable differences, due to unknown electrode material/thickness and mounting method in the sealed oscillators. It should be reasonable to take these models and use their advanced physics models to provide a considerable amount of direct

insight to the electro-mechanical behavior of the higher quality QCM with its well-known parameters.

4.2 Electrical Output of QCM Devices

The QCMs used for our testing were 0.538" diameter, 5 MHz nominal resonance quartz crystals, shown below in **Figure 43**. The QCM is mounted with especially thin wire braces as opposed to the more rigid aluminum arm type mounts used in the common oscillators to help isolate the crystal from environmental noise, and is coated using gold electrodes for gold's preferable electrical properties when compared to other common electrode materials. Several QCMs were ordered and on hand in case one was damaged in any way so that we did not have to continue collecting data, from a flawed device. However that problem never arose and so all was collected from the single QCM pictured below. Applying all the information gained throughout the course of investigation and the same testing procedure used in testing the other oscillators, Investigation of the QCM itself went very smoothly.

As expected the high level of manufacturing for the QCM produces the cleanest and most ideal results yet achieved during experimentation. The results produced by the uncoated QCM tracked very closely to the digital model whose properties were matched to its specifications. Much closer in fact than any of the other oscillators even after accounting for any potential of error in the models.

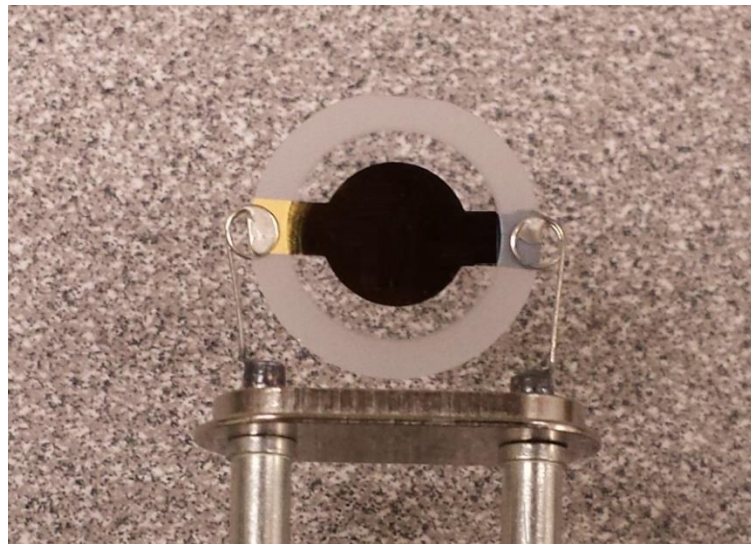


Figure 43: Close-up photo of QCM used for final testing.

Table 6: QCM Voltage and current: measurements vs. Predictions for 0. 583” QCM model

Oscillator Info			Voltmeter measurement (mV rms)		Current measurement (mA)	
Nominal Frequency	Description	Actual Frequency	Voltage Drop	Voltage after QCM	VSA/SQUID	Model predicted
5 MHz	QCM	4,997,600	1.033131	20.56	0.4113/0.48169	-
5 MHz	Digital model	4,997,600	-	21.531	-	0.5106

Since the QCM shares a good deal in common with the largest 5 MHz common oscillator, the digital model required only a few changes to bring the build specifications in line, and some small adjustments to match the models peak frequency to the peak frequency of the QCM. That being the case, the predictions between the 5 MHz large oscillator and the QCM models is extremely close. Something different however is how close the QCM device’s performance is to the model predicted behavior. Looking back to Table 5, you can see that the results for the large 1” diameter 5 MHz digital model are much closer to the 5 MHz higher quality QCM than for the regular oscillators.

The difference between the voltage values measured at the point after the QCM (points 3, 4 in **Figure 42**) is about 5%, while the difference in current is also low at approximately 6%. It’s difficult to say for certain whether this amount of error might be reduced further by better linearization of the SQUID before measurements or if a majority. A good deal of additional testing was performed producing a full set of data for full-width half-max measurements for all of the oscillators and the QCM. This was performed by using the previous sets of data and powering the oscillators at each half max frequency and measuring the response. It is likely that this data, although not utilized directly by this project may be useful in future work and so the half max peak data sets have been included in Appendix D.

The reasonable accuracy of the common oscillator systems as well as the high accuracy of the QCM based modeling results lends a considerable amount of credence to the variety of other possible measures derived from the 3-D physics model. As mentioned previously, the models primary module is MEMS based physics module, and as such takes all relevant electromagnetic, mechanical, and piezoelectric effects into consideration. The result is outputs for a large number of mechanical measures taken either globally within the model or at important points on or inside said model. Included in this data are values for a variety of things, from direct mechanical measures such as huge

number of stress and strain measures in the crystal, as well as a variety of values more directly useful for measurement like face velocity and acceleration.

These values are likely to be the most important for future development of complex relations for the QCM, due to the direct relation of these values to the force being applied to any samples applied to the surface. Shown below are visualizations of the distribution and intensities of several basic mechanical properties, as well as a table relating the electrical and mechanical properties in the direction of induced motion (x-direction). Seen below is a discussion of the force acting on an “added mass”, in this case using the electrode to illustrate how these values might be applied to a sample of known density. For ease of visualization the **Figures 44-47** displayed represent the either the amplitude or maximum of each value per cycle and actual values vary with phase. For example face velocity reaches its peak at a phase of 0 and 180 degrees (0 and pi radians), while acceleration peaks at 90 and 270 degrees, so displaying both at 180 degrees would no show significant acceleration.

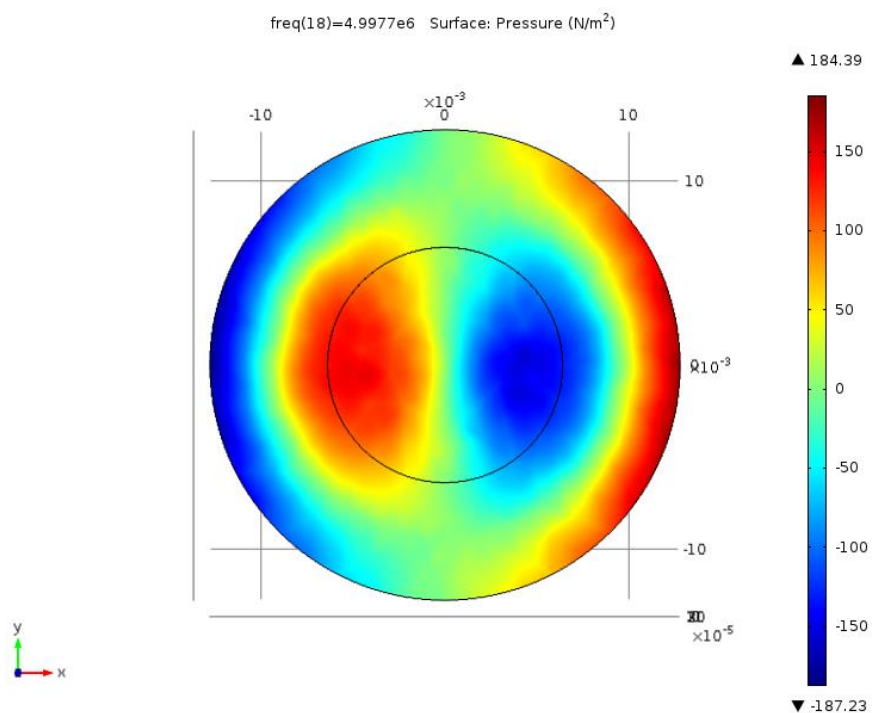


Figure 44: Pressure acting on the QCM in N/m² at phase = 270 degrees

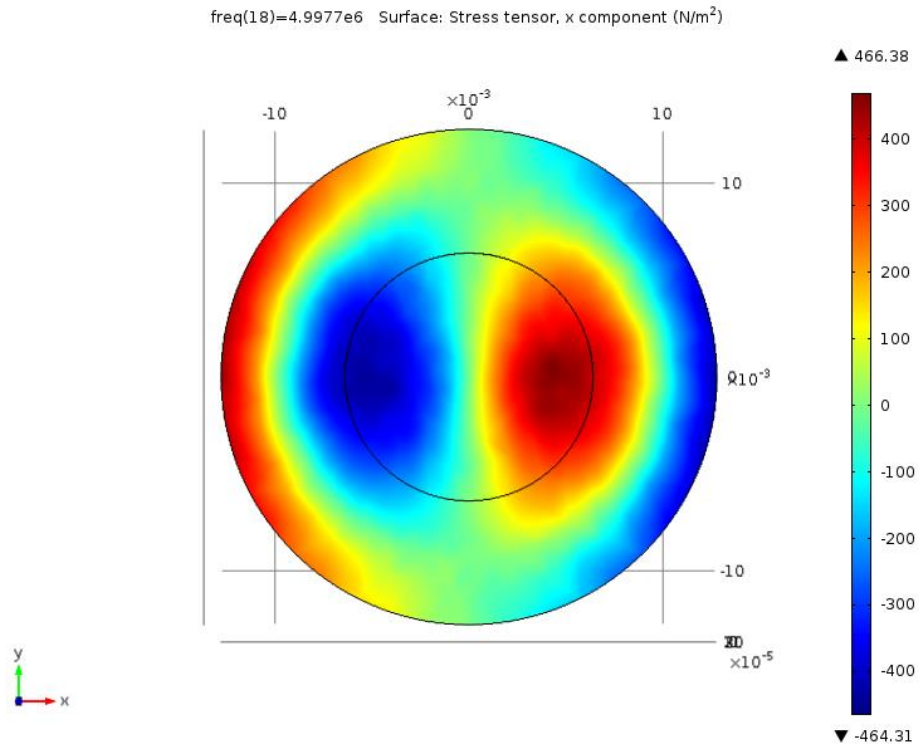


Figure 45: Value of stress tensor x on the QCM in N/m² at phase = 270 degrees

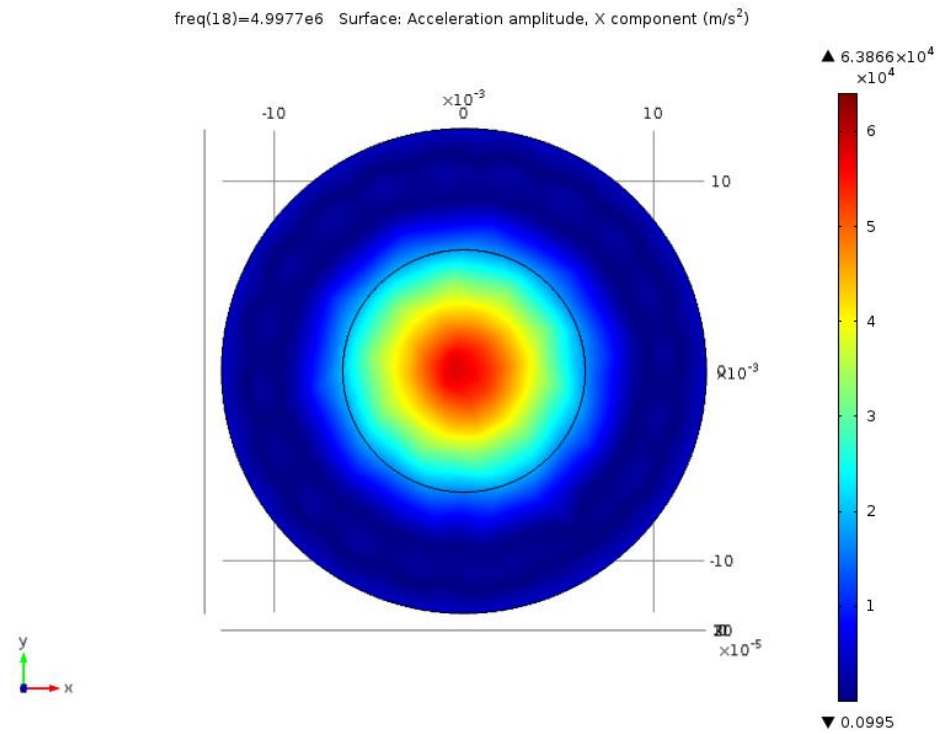


Figure 46: Maximum acceleration acting on the QCM in m/s², Max at phase = 270 degrees

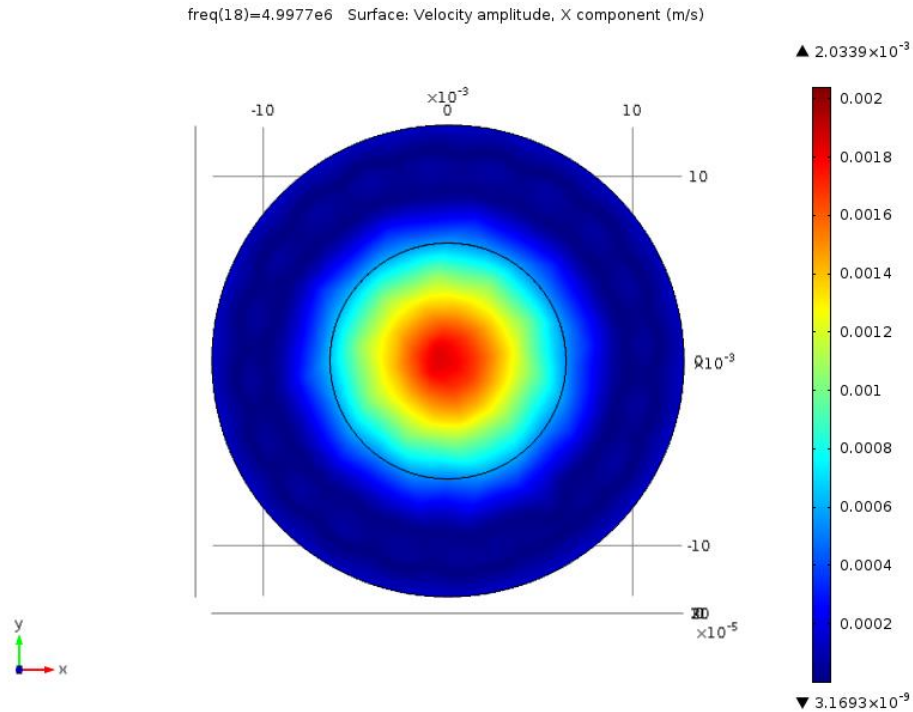


Figure 47: Maximum velocity of QCM surface in m/s, max values seen at phase = 180 degrees

Table 7: Mechanical results of the digital model vs. modeled electrical values.

Measure	Frequency	Voltage	Current	Stress tensor x	Acceleration	Velocity
Unit	MHz	mV rms	mA	N/m ²	m/s ²	m/s
Value	4.9977	21.56	0.5106	466.38	57,634	1.84E-03

As you can see in **Table 7** the maximum stress and acceleration coincide at a phase of $\pi/2$ and $3*\pi/2$, resulting in a maximum velocity at 0 and π . At first glance values of hundreds of newtons per meter² and accelerations in the tens of thousands of m/s² (nearly 6000 g's) seems quite large, but considering the scale of the oscillator (approx. 0.0005m²) and the frequency (~5,000,000 cycles per second) these figures seem more reasonable. It seems overwhelmingly clear that the ability to relate these values directly back to the simple electrical properties of the system in operation without the use of computationally intensive finite-element modeling such as the ones used in this project would provide a large boost in utility and accuracy of the QCM. It is also extremely likely that such relations

would provide for a number of novel applications for these systems such as measurement of surface cohesion, since these values should be possible to obtain from the values of surface acceleration once mass and thickness values are obtained.

For example, given the modeled electrodes are gold of 250 nm thickness and 0.5 inch diameter. The electrode surface area is 0.00012667m^2 which gives a volume of gold of $3.167\text{E}-11\text{ m}^3$ and a mass of just over 0.6 mg per electrode. Given the acceleration provided above, this means that the electrode is experience a momentary force of about 0.03522 N. Given know surface area and forces as well as a slew of other measurements, new applications such as this are likely to find use of these relations.

4.3 Water and Cell QCM Operation

Since much of the QCM based research of late has been in the biomedical field, with experimentation in a water cell or submerged in water or other liquid solutions, it seemed prudent to perform additional testing in setup more generalizable to that work. This was performed in two manners, by applying de-ionized water directly to the surface of a new QCM and by placing the new QCM in a pre-made testing cell such as the on seen in **Figures 48-50** and filling the cell with DI water. A separate QCM was used from the previous testing so as not to accidentally effect performance of the QCM that contributed most of the data from previous experiments incase retesting anything was necessary. Using the bare QCM as a reference this course of testing produced three full sets of distinct results that will now be discussed. FRA and electrical data for the wet QCM, the cell (dry), and cell (wet).

The results produced are extremely predictable given background knowledge of the piezoelectric effect and oscillators. These effects include the expected peak shifting and response dampening (peak rounding and overall magnitude decrease) from the water addition,^[42] as well as a much larger amount of dampening from the O-rings bracing the QCM during the cell testing. These effects are clearly visible in the FRA data in **Figures 51, 52**. As adding water to the surface of the bare QCM was difficult several trials were done using visually similar quantities of DI water, cleaning and drying the QCM with Kimwipes between each run. As you can see in **Figure 52** there was also significant variation caused by how tightly the cell was sealed onto the QCM (effect seen between run 1-2), but this effect was easily negated nearly entirely by making sure to use a set procedure for tightening thus creating a repeatable and uniform pressure on the QCM (wet cell runs #2-3 lie right atop one another).



Figure 48: QCM resting in disassembled cell



Figure 49: QCM submerged in water cell (open top)

Figure 50: Closed and connected water cell for QCM measurement

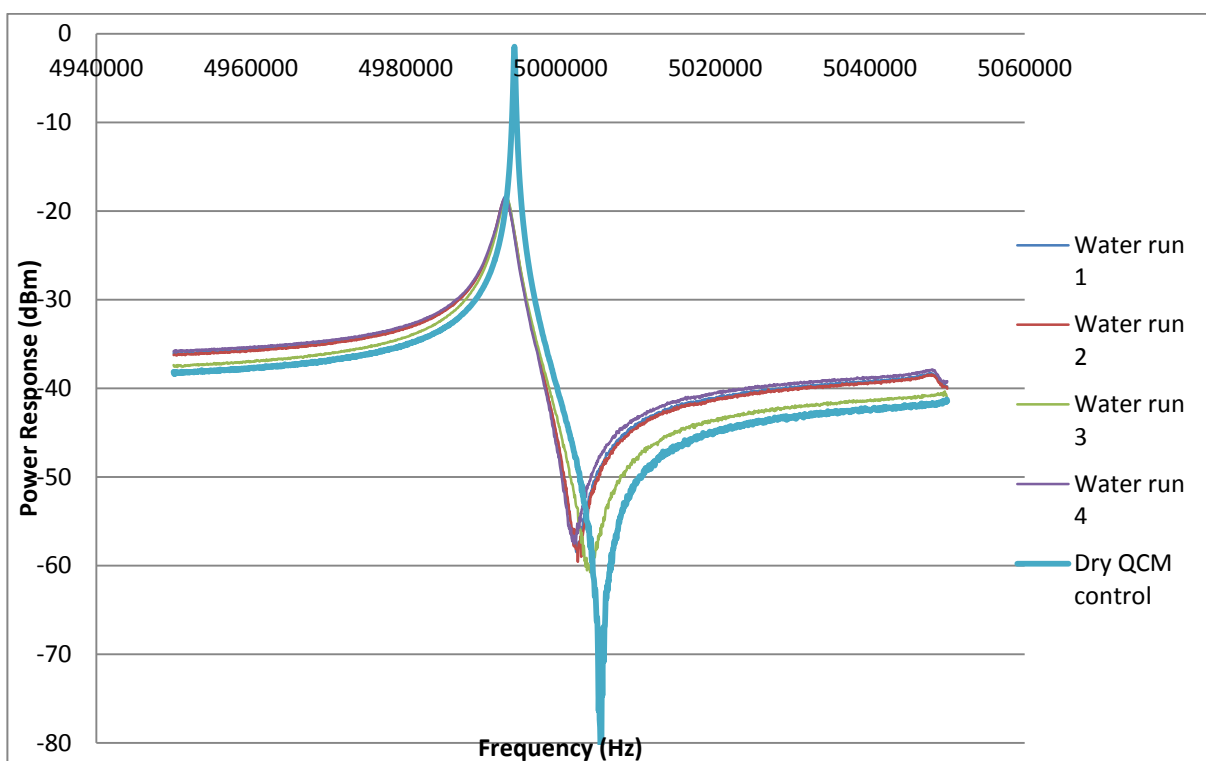
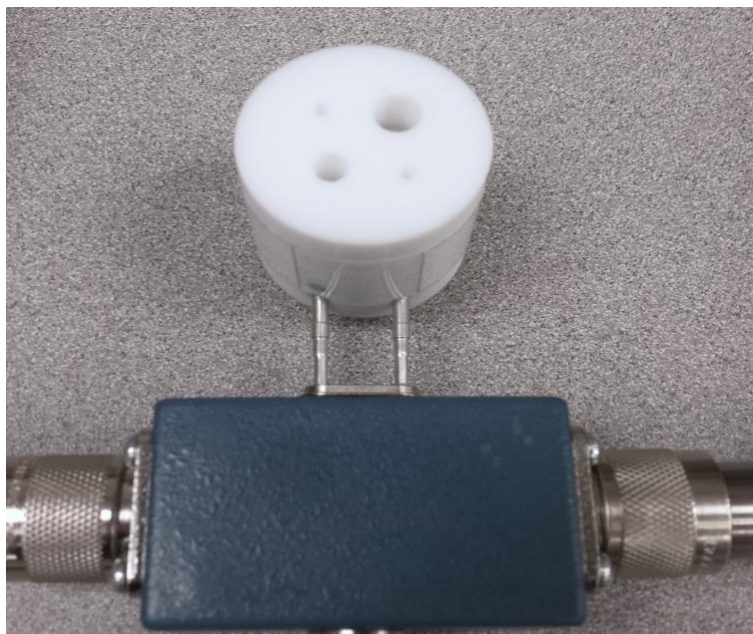


Figure 51: effects of water on bare QCM device

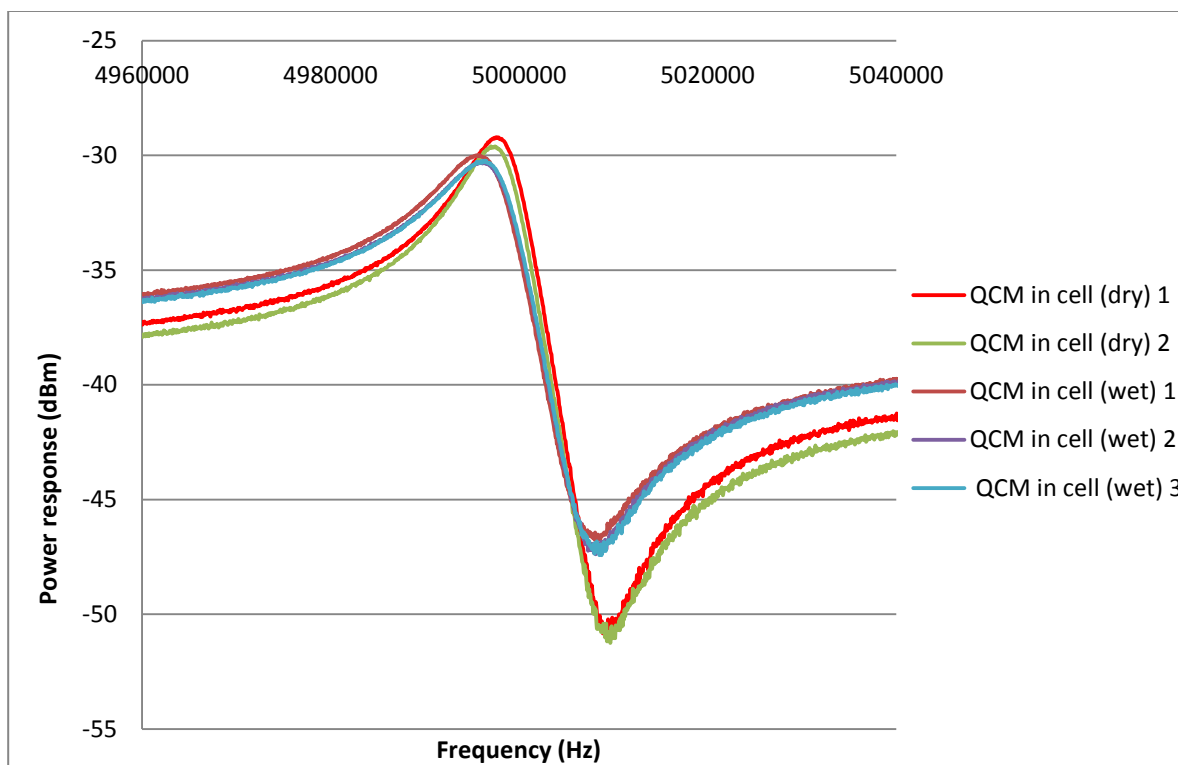


Figure 52: Effects of water in cell testing

When examined all of the rounds of water testing, it is clear that cell-based testing and water-based testing in general contribute nothing more in the way physical or electrical effects than what might be obtained by adding a large amount of any mass to the surface. However, this in and of itself seems to represent an issue for the accuracy of current methods of QCM testing in water. As was discussed in the beginning of this paper, current measurements are based around the use of the Sauerbrey equations, and include the fundamental limitations that these equations entail. This specifically means that due to the Sauerbrey's equation modeling all additions as added quartz thickness it becomes increasingly inaccurate after adding >5% of the QCM's mass. As is shown by the FRA data, simply the addition of the water and especially the cell testing cause considerably more dampening than would be appropriate for using these relations.

But there are more difficulties than just the accuracy of the applicable relations, the poor peak resolution seen in the FRA data creates an additional hurdle. This broadening that is caused by viscous dampening and by physical constraints of the rubber O-rings in the cell, is most visible in the FRA data shown in **Figures 51** and **52**. This trend carried through into the absolute power metric used

to make traditional measurements. It causes what would normally appear to be a single sharp, high-Q spike to become widened considerably, thus making it difficult to resolve the actual resonant frequency as precisely or accurately.

Table 8: Peak spread and Q-factors for water based testing

System Description	Run #	Peak Frequency (Hz)	Peak power (dBm)	Power Ratio halfmax Spread (Hz)	Dissipation (D)	Q factor
Dry QCM control	0	4,994,063	-1.44	2350	0.000470559	2125.133
Water on bare crystal	1	4,992,938	-18.33	6267.5	0.001255273	796.6394
	2	4,992,875	-18.58	6312.5	0.001264302	790.9505
	3	4,993,000	-18.51	6300	0.001261766	792.5397
	4	4,992,875	-18.56	6100	0.001221741	818.5041
Air cell	1	4997812.5	-29.215681	14187.5	0.002838742	352.2687
	2	4997625	-29.657204	14862.5	0.002973913	336.2574
Water cell	1	4995750	-29.9886	17125	0.003427914	291.7226
	2	4996187.5	-30.298101	16187.5	0.00323997	308.6448
	3	4996375	-30.232172	17250	0.003452503	289.6449

While these large dissipation and low quality may not be as serious of an issue for some biomedical applications, with proteins and cells being made of huge numbers of atoms each and measured in the hundreds or thousands of cell and thus the changes to the peak frequency quite large; The difficulties regarding applying Sauerbrey relations accurately would likely be increased, since the masses which are already above 5% limit for applying the relation would have a decreased frequency resolving ability than one might expect with other applications. This means that unless additional calibrations steps are taken, such as using precisely (at least on the same scale as desired measures) known quantities the signal of low level mass measurements will become lost in the noise.

Comparison to digital models

Examining the digital models for these experiments only serves to confirm what the lab collected FRA data suggests, namely that water based testing serves to significantly decrease the accuracy of the system. Although it was not possible to reproduce the conditions of the water based testing with the same level of accuracy as in the earlier models; due to the inclusion of complicated

geometries or non-measurable damping values from the test cell. The models produce results in line with expectations of these systems based on observed behavior in real testing.

Examining the exterior of each model in **Figures 53-55** which show the peak displacement experienced at any point in the system at its resonant peak, it's not difficult to see that there is a significant amount of energy being transferred away from the system and into the water inducing a significant loss as all the forces are dissipated by the fluid. Even without direct electro-mechanical correlations it seems quite obvious that there is a loss of mechanical motion and energy involved in moving the water in this fashion. This effect along with water's nearly zero energy retention would be translated into the change in electrical responses shown in our lab FRA measurements. There is also a general decrease in the amount of motion visibly apparent on the surface of each model as the amounts of water is increased as seen in the maximum values atop the scale bar on the right side.

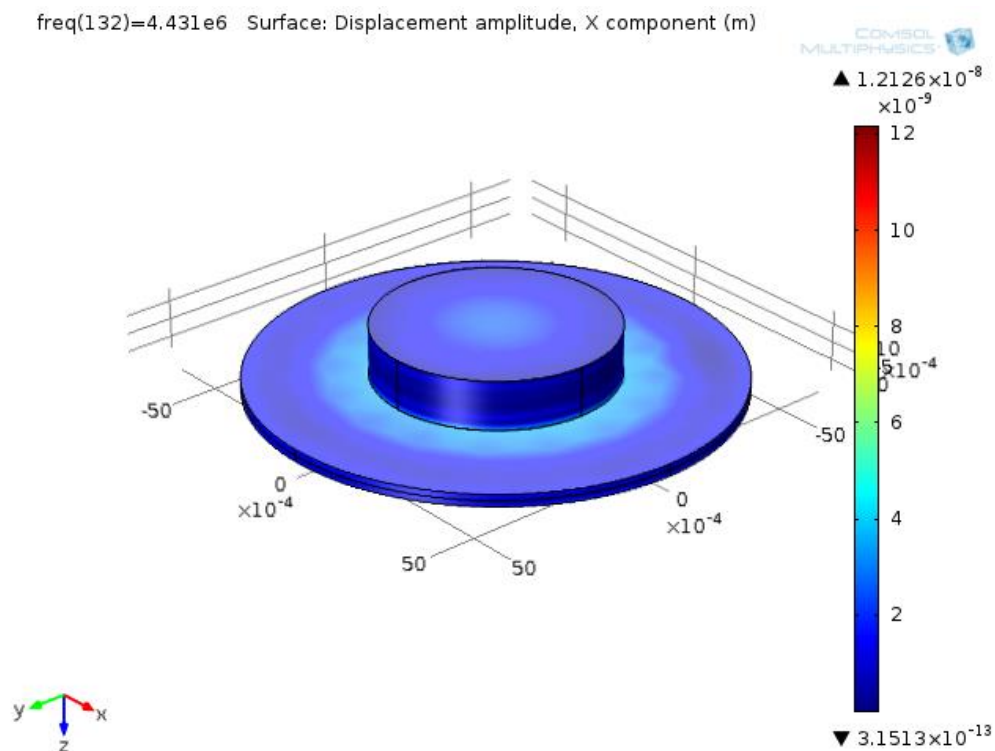


Figure 53: Partial water coverage as seen in 'cell' testing

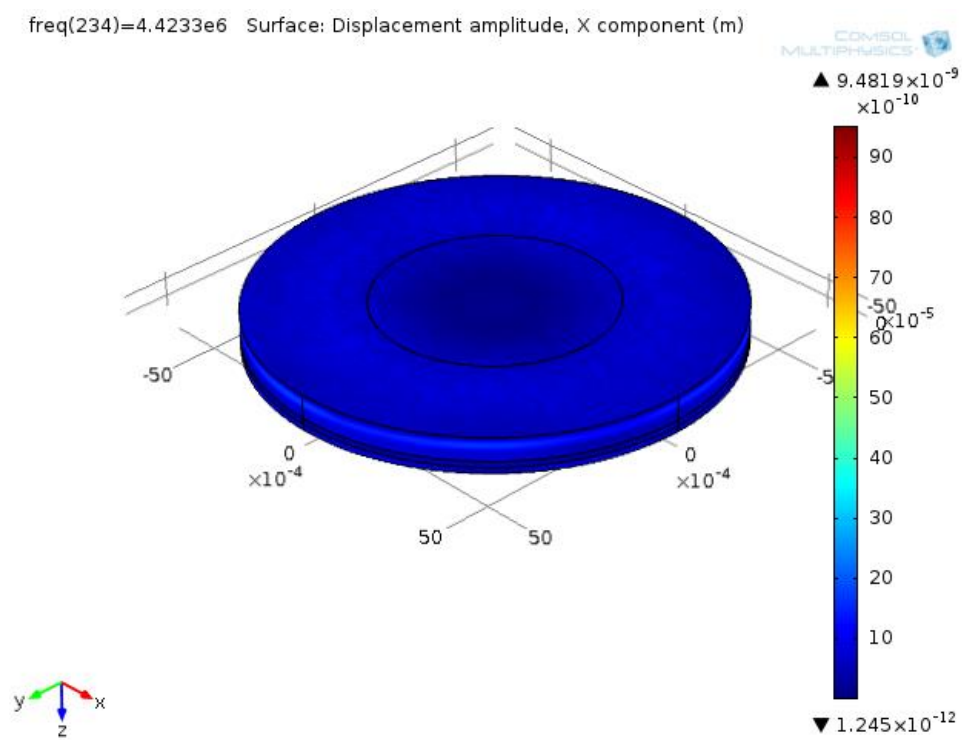


Figure 54: Full water coverage approximation as seen in 'water on bare QCM' testing

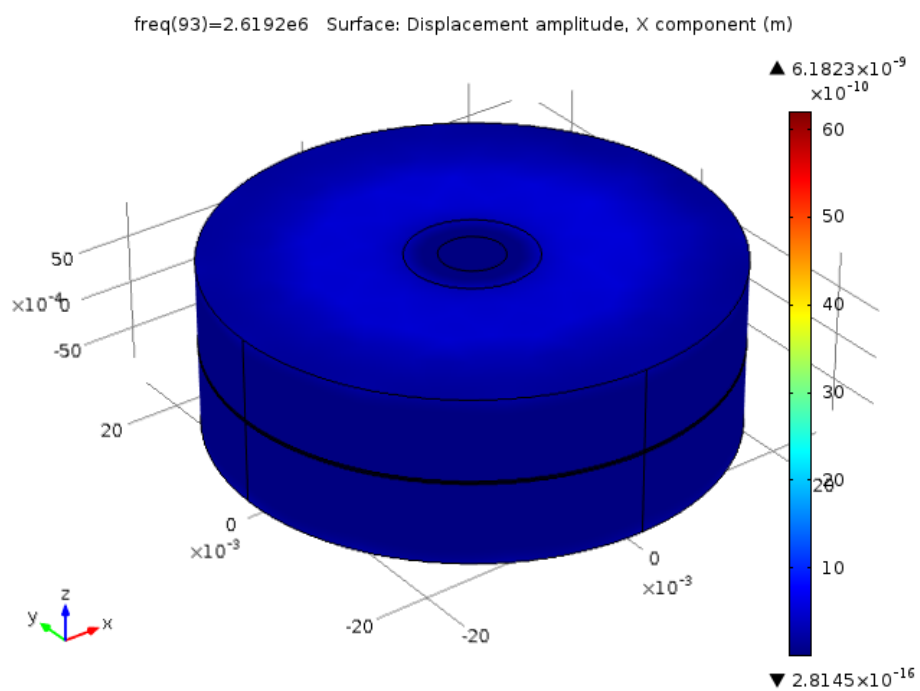


Figure 55: Submerged QCM model approximation

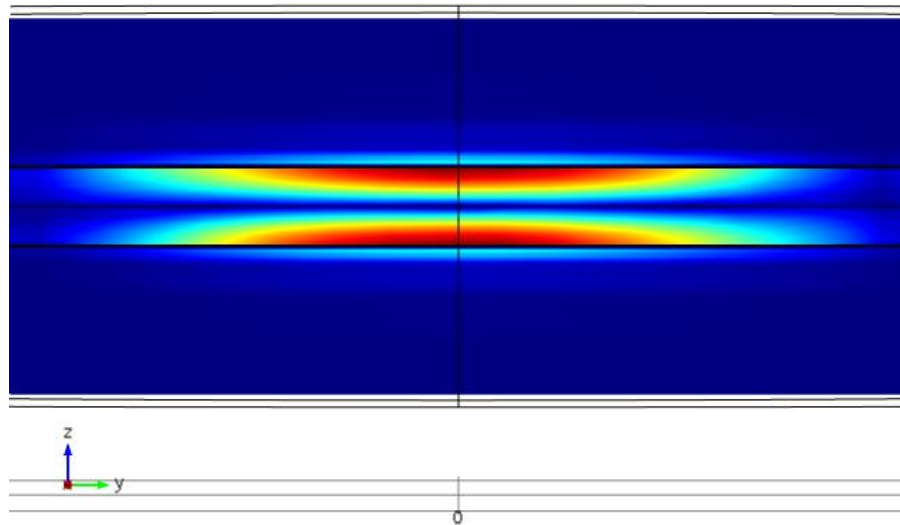


Figure 56: Submerged QCM model semi-transparent midsection cutaway

Tracking the dissipation of this motion gives a good visualization of the losses in energy associated with the water. A trend which plays out in the two dimensional graphs shown below, in fact the effect is so strong that in the submerged model (**Figure 55**) it's difficult to see any displacement at all due to the damping and large amount of energy lost in the intervening water unless you view the displacement value nearer the surface of the QCM. It's difficult to illustrate the full effect in good detail without being able to interact with the model itself but the midsection cutaway shown in **Figure 56** does a reasonably good job at illustrating how the induced motion quickly dies out extremely quickly in the water due to the lossy behavior of the fluid, dropping in magnitude nearly 90% within 2 micrometers.

When examining the mechanical FRA data for the models in **Figures 57-59** (in displacement field (m) vs. frequency (Hz), instead of power ratio (dBm)) you can see that though the resonant frequency shifts are somewhat different than the electrical FRA data obtained during testing due to the number of unknowns; the general outline of the curves with the rounded peaks are much the same when compared to **Figures 51, 52**. The damping and peak spread behavior is seen once again lending some confirmation to the measurement.

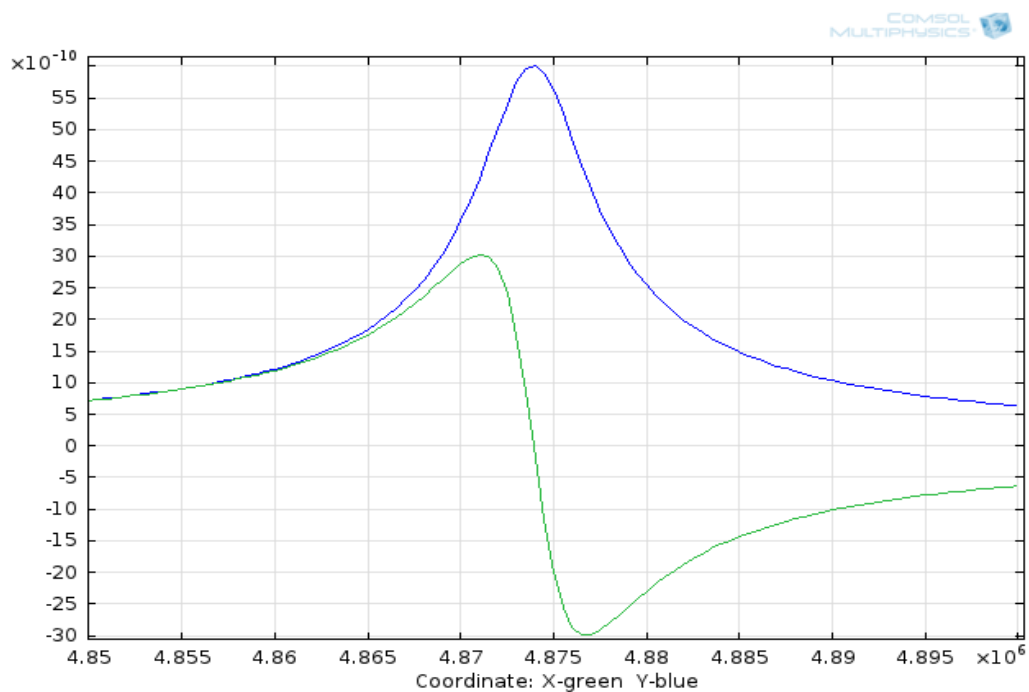


Figure 57: Mechanical FRA for partial 'cell' coverage (displacement amplitude (m) in blue, displacement field (m) green)

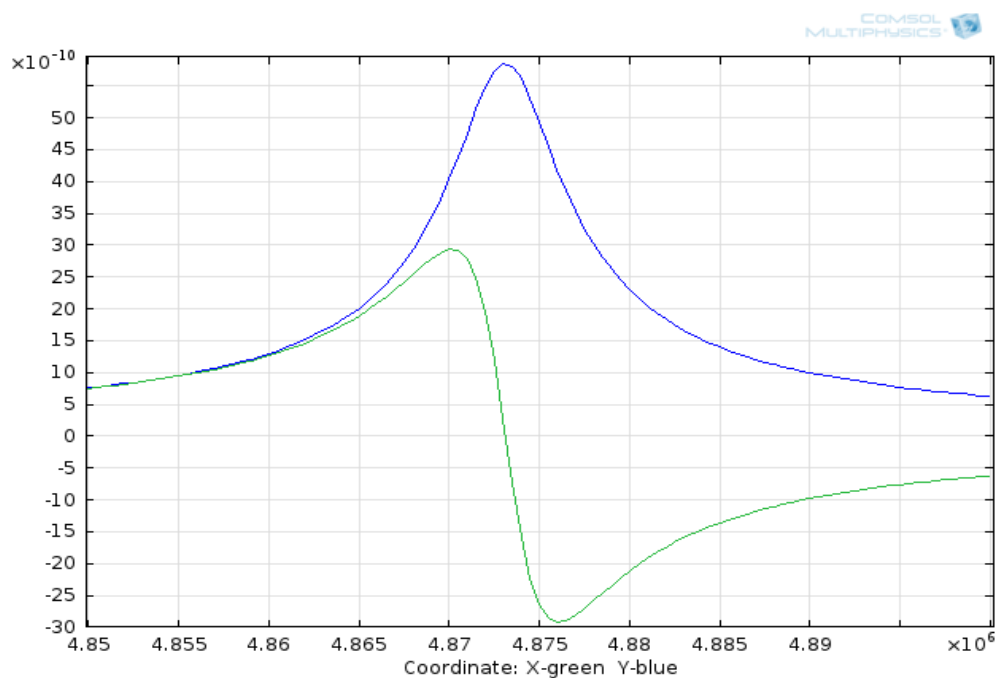


Figure 58: FRA for Full 'water on bare QCM' coverage (displacement amplitude (m) in blue, displacement field (m) green)

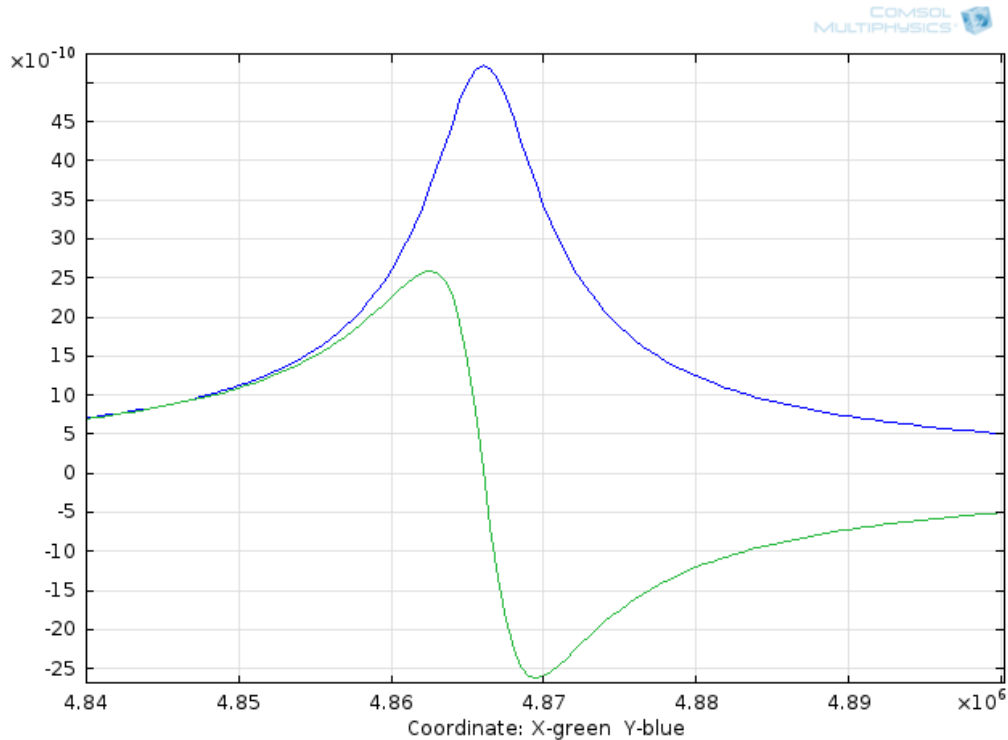


Figure 59: Mechanical FRA for submerged QCM(displacement amplitude (m) in blue, displacement field (m) green)

Table 9: Water models peak spread and Q-factors comparison

System Description	Halfmax Spread (Hz)	Dissipation (D)	Q factor
Dry QCM control	2350	0.0004705	2125.133
Water on bare crystal	6267.5	0.0012552	796.639
Full surface model	5600	0.0012660	789.875

Comparing the full coverage model in **Table 9** (since the only model that is directly comparable to a real world counterpart, no real submerged model/ unknown damping from cell) and putting the other two models aside you can see that despite the small geometry differences in the water on the surface the model predictions share extremely strong similarities to measured peak spreads and Q-factors measure from the ‘water on bare QCM’ measurements, as well as both producing noticeably larger peak spreads and lower Q-factors when compare to the dry models both real and modeled. This is something that was expected from the early stages of experimentation due

the general nature of piezoelectricity as well as the poor properties of water in this application; so this data serves to confirm this idea that QCM devices would likely produce lower accuracy measurements, and hopefully spur interest in the area or movement to a different measurement technique.

Despite this water testing not directly producing any surprising or novel result, this testing along with the small amount of confirmation achieved via modeling, illuminated the merit of providing this area additional attention. Currently due to the high levels of damping in water systems, this area seems to be a low priority for further high accuracy mass measurement investigation. However, further investigation into the effects of water cell testing and the exact relationship between the voltage/current and the velocity and force applied to/by QCM devices in general may one day help this sort of water testing approach a similar accuracy as other applications.

Chapter 5: Conclusions and Future Work

Project Conclusions

The purpose of this project was to further the knowledge of quartz crystal oscillator systems as they are applied in the quartz crystal microbalance. This involved:

1. Developing an integrated 4-point probe measurement system for radio frequencies using a custom SQUID-based ammeter showing linear response into the megahertz range
2. Taking precision electrical measurements of QCM systems during operation in common measurement environments.
3. Producing and simulating digital physics models of those systems.

By performing the testing as outlined by the goals of this project a considerable amount insight has been gained into the oscillator systems and much more insight into how to continue investigations for this project and the QCM system in general.

The measurement of these systems, as performed by this experiment, though not nearly as conclusive as they might have been given a larger sample of more ideally behaving common oscillators, have shown a reasonable evidence for some basic conclusions about the QCM system. There are a few trends apparent in the data including the relationships for frequency and size to the voltage and current transmitted through the system at resonance. Firstly it seems clear based on the testing, specifically when comparing the 3 and 5 MHz oscillators that although Tables 4, 5 particularly seem to show some correlation with the electrical behavior, these results were due to non-ideal behavior and other results including digital modeling tend to provide evidence that the frequency has very little to do with the amount of Voltage and current passed through the crystal.

The second relationship that seems clear from that set of data is that the size of the oscillator, at least where common oscillators are concerned, is a strong predictor of the quality of performance of the crystal where signal reflection is concerned. These results in a large voltage drop and current passed through the system. The last major insight gained into this system has to do with the ability of the digital model to adequately represent the systems being investigated. In the tests that produced a large amount non ideal behavior, the results from the digital model deviated from the recorded values by a significant margin which could have been misinterpreted without close attention.

The issue discovered with the digital modeling process is in how it is unable to deal with any non-idealities that show up in the real world counterpart. The most relevant example of this was the model's inability to replicate the signal reflection phenomena exhibited at least in small part by all of the oscillator but especially the lower quality and lower frequency crystals. The issue isn't something that can be said to be endemic to the software, but instead appears to arise from a how the specific physics modules used by COMSOL for these systems. More specifically, the issue is caused by how the two distinct physics modules are not directly intertwined as the effects are in reality but instead are solved in a more sequential manner.

In many other situations such as a transport phenomenon based system the heat, mass, and energy values are fundamentally intertwined. In this case, at least with its current design, COMSOL solves the AC/DC module first,^[37] then uses that set of predetermined electrical data from before the oscillator and models the effects seen in the crystal as well as the voltage and current passed through the crystal based on those values. This in effect models the system in an ideal manner, which has been shown to be an extremely poor assumption for all except high quality crystals including the QCMs.

Though this has been an issue for this project, it is not a something that represents a major hurdle to further study of the electrical environment of QCM operation. Since furthering knowledge of QCM systems does not necessitate comparisons using the common oscillators that caused the issues, but was simply a choice made early in this project; further experimentation using a number of additional QCMs of varying resonant frequencies would lead to large scale improvements in the linearization and digital comparison parts of the project. This concept represents a critical point in continuing this research. Accuracy in measurement has been a major theme throughout the project and without sufficient accuracy both from how the digital modeling represents the real world examples as well as measurement, significant improvements in the QCM system may remain elusive.

Better understanding the coupling of the fundamental piezoelectric properties to the functioning of the QCM sensor is the goal toward which this project has taken a step. Ahead lie a large number tests using not only a variety of films added to the surface, but on a number of different QCMs designed for operation in even higher and more accurate frequency regimes and using different cuts and material oscillators.

Next Steps

Despite a considerable amount of headway being made into improving the characterization of the QCM system, there are a number of additional steps that need to be taken towards gaining a more complete understanding. The first step is to perform additional testing, especially where the SQUID was concerned. Collection of a much larger pool of data before making correlation equations for the SQUID would have made for a more rigorously accurate model for interpreting the SQUID's response. Although the SQUID showed itself to be likely more accurate than the traditional alternative (by consistently making measurements of current proportionally higher than the alternatives such that it seems to account for the losses one would expect from the system), increasing the linearization pool would help correct for any error, in linearization. The previous linearization despite having more than 35 initial data point, suffered due to the removal of some of the end data as well as the 5.8 KHz, due to some of the low frequency limitations of the equipment. The limitation in sufficient data points that this caused led to trend line data that likely was not as accurate as what may be achieved.

Now that there is sufficient background data to work from, the second step towards furthering investigation in this area would be to make additional measurements for coated QCMs. Thus far measurements that have been taken have been for the bare QCM or water cell systems to serve as a basis for future investigation. However, any future empirical modeling will most certainly need to have data that includes mechanical properties from which to build. This entails the coating of QCM devices with films of known thickness (mass) and preferably also known viscoelastic properties, such that digital models and accurate electrical measurements can be paired with mechanical properties and the mechanical properties predicted from said models. The resulting data may well lead to an in-depth characterization of not only QCMs but possible also generalizable relationships for other piezoelectric sensors. Once all the all desired testing has finished, a large scale data and statistical analysis project that would analyze the electrical data as well as the digital models mechanical data, to search for trends relating these phenomena. In doing so it may be possible to find and simplify numerical models for correlating the mechanical behavior of a system given any number of electrical circuitry conditions.

The coupling of these fundamental properties is the goal toward which this project has taken a step. Toward that end lies a large number of this sort of testing using not only a variety of films added to the surface, but on a number of different QCMs designed for operation in different

frequency regimes and possibly using different cuts and material oscillators as well. Needless to say, this would involve a large commitment of not only time and labor but likely also a significant investment as far as funding is concerned.

Long Term Goals and Project Application

This project has focused on developing a better set of instrumentation to understand the physical behavior of QCM sensors and other piezoelectric systems. However, in addition to such potential applications as are mentioned previously there are a number of future piezoelectric sensor applications that would benefit from additional insight into these systems. Many of these applications have to do with an area where traditional QCM are seen to be inappropriate.^[40] As discussed in the Introduction, high temperature surface science studies are inaccessible to the QCM. This research has led to new proposals to break this barrier through the use of new resonator structures.

This research would likely see large scale use in industrial applications such as combustion sensing and material processing as well as several film deposition processes where temperature limitations have previously prevented their use. A variety of industrial processes that require high temperatures would also benefit greatly from an increase in mass detection sensitivity. Creation of high temperature piezoelectric sensor systems using materials such as lithium niobate are currently being tested, but as there are no high temperature mass sensors of commensurate sensitivity they have little to no verifiable empirical data towards their accuracy in these high temperatures. A predictive model as well as any other insight into these systems would likely prove to be a boon to this research as well as relevant industries. While this would involve a large commitment of time, labor and money, there is the potential to study catalytic and surface reactions with an unprecedented level of detail and may well lead to novel uses for this technology.

References

- [1] Zimmermann B., Lucklum R., Hauptmann P., Rabe J. and Buttgenbach S. "Electrical characterization of high-frequency thickness-shear mode resonators by impedance analysis", *Sens. Actuators B* 76. 2001, 47-57.
- [2] Matthew A.C., Fedor N.D., Minson T., Victor P.O., Abell C. and Klenerman D. "Direct and sensitive detection of a human virus by rupture event scanning", *Nature biotechnology*. 2001, Volume 19.
- [3] Schwartz, Alan. "Novel Equivalence Principle Tests." Eotvos and. N.p., 1 Jan. 2005. Web. 10 May 2014. <<http://www.mazepath.com/uncleal/eotvos.htm>>.
- [4] "Piezoelectric Generators: Applications | Piezo Theory." Piezoelectric Generators: Applications | Piezo Theory. APC international, n.d. Web. 3 Apr. 2014. <<https://www.americanpiezo.com/piezo-theory/generators.html>>.
- [5] Gautschi, G (2002). "Piezoelectric Sensorics: Force, Strain, Pressure, Acceleration and Acoustic Emission Sensors, Materials and Amplifiers". Springer.
- [6] Korotcenkov, Ghenadii. "Chemical Sensors Comprehensive Sensor Technologies" Volume 4 Solid State Devices. Momentum Press, 2011. 386-400. Print.
- [7] Buttry, Daniel. "The Quartz Crystal Microbalance as an In Situ Tool in Electrochemistry." The Defense Technical Information Center . University of Wyoming, 05 Jul 2002. Web. 25 Mar 2013.
- [8] "Basics of a Quartz Crystal Microbalance." Gamry Instruments, 14 Feb 2012. Web. 25 Mar 2013.
- [9] Arnau, Antonio. "A Review of Interface Electronic Systems for AT-cut Quartz Crystal Microbalance Applications in Liquids." *Sensors*. 8. (2008): 370-411. Web. 25 Mar. 2013.
- [10] Kremer, Felix, et al. "Detection of phase transitions in thin films with a quartz crystal microbalance." *Solid Films*. (1996): 436-438. Print.

- [11] Rodahl, Michael, et al. "QCM Operation in Liquids: An Explanation of Measured Variations in Frequency and Q Factor with Liquid Conductivity." *Journal of Analytical Chemistry*. 68 (1996):
- [12] Thostrup, Rebeca. "Quartz Crystal microbalance." Interdisciplinary Nanoscience Center. Aarhus University. Web. 25 Mar 2013.
- [13] Rodahl, Michael, et al. "Quartz crystal microbalance setup for frequency and Q-factor measurements in gaseous and liquid environments." *Revision of Scientific instrumentation*. 66.7 (1995): 3924-3930.
- [14] Wang, Juan, et al. "Piezoelectric pH Sensors: AT-Cut Quartz Resonators with Amphoteric Polymer Films." *AC Research*. 65. (1993): 2553-2562. Print.
- [15] Bartosz Wyszynski, Daeho Kim, Takamichi Nakamoto, Stabilization of coating for QCM odor sensors with liquid GC materials supported by lipopolymers and lipids, *Sensors and Actuators B: Chemical*, Volume 179, 31 March 2013, Pages 81-86,
- [16] Heitala, S.L., et al. "Pore Structure Characterization of Thin Films Using a Surface Acoustic Wave/Volumetric Adsorption Technique." *Langmuir*. 9. (1993): 249-251. Print.
- [17] Hinsberg, W, et al. "Characterization of Reactive Dissolution and Swelling of Polymer Films Using a Quartz Crystal Microbalance and Visible and Infrared Reflectance Spectroscopy." *Macromolecules*. 38. (2005): 1882-1898. Print.
- [18] Čavić-Vlasak, Biljana A., and Jubinka V. Rajaković. "Application potential of liquid-phase acoustic wave devices as chemical and biochemical sensors." *Fresenius' Journal of Analytical Chemistry*. 343.4 (1992): n. page. Print.
- [19] Zheng-peng Yang, Chun-jing Zhang, "Designing of MIP-based QCM sensor for the determination of Cu(II) ions in solution, *Sensors and Actuators B: Chemical*", Volume 142, Issue 1, 12 October 2009, Pages 210-215,
- [20] An-Hua Wu, Mei-Jywan Syu, "Synthesis of bilirubin imprinted polymer thin film for the continuous detection of bilirubin in an MIP/QCM/FIA system", *Biosensors and Bioelectronics*, Volume 21, Issue 12, 15 June 2006, Pages 2345-2353,

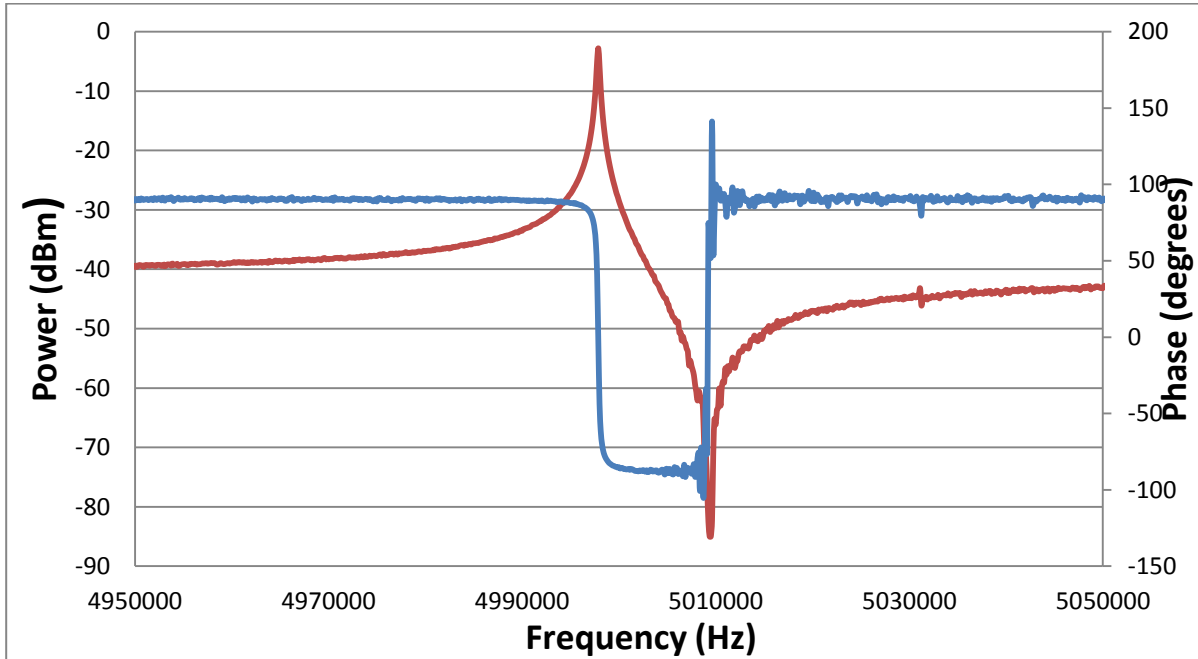
- [21]Xiao Fan, Binyang Du, "Selective detection of trace p-xylene by polymer-coated QCM sensors", Sensors and Actuators B: Chemical, Volumes 166–167, 20 May 2012, Pages 753-760,
- [22]Wimmer, L, et al. " New method of measuring vibration amplitudes of quartz crystals." Revision of Scientific instrumentation. 55.4 (1964): 605-609. Print.
- [23]Correlation between Crystal cut and Frequency vs. temperature characteristics. 2013. Graphic. Citizen Finetech Miyota Co.Web. 15 May 2013.
<http://cfm.citizen.co.jp/english/product/cvo_character.html>.
- [24]"Surface Plasmon Resonance Technology | Principle of SPR Detection | Quartz Crystal Microbalance."Surface Plasmon Resonance Technology | Principle of SPR Detection | Quartz Crystal Microbalance. Biosensing Instruments, 1 Jan. 2006. Web. 3 June 2014.
<<http://www.biosensingusa.com/Application103.html>>.
- [25]Hewlett, Packard. "Fundamentals of Quartz Oscillators." Electronic Counters Series 200: n. pag. Web.
- [26]"Four-point" by User:Vessels42 . Web. - <http://en.wikipedia.org/wiki/File:Four-point.png>.
Licensed under Public domain via Wikimedia Commons -
<<https://commons.wikimedia.org/wiki/File:Four-point.png#mediaviewer/File:Four-point.png>>
- [27]Chan, James . "Four-Point Probe Manual." . EECS, 1 Jan. 1994. Web. 18 May 2014.
<http://www-inst.eecs.berkeley.edu/~ee143/fa10/lab/four_point_probe.pdf>.
- [28]Clarke, John, and Reinhold Kleiner. "Superconducting quantum interference devices: State of the art and applications." Proceedings of the IEEE: 1534-1548. Web. 27 may. 2014.
- [29]Chiorescu, Irinel. "On-chip SQUID measurements in the presence of high magnetic fields."Nanotechnology 21: 405504. Web. 3 Aug. 2014.
- [30]Miraceti "DC SQUID" Licensed under Creative Commons Attribution-Share Alike 3.0 via Wikimedia Commons
<https://commons.wikimedia.org/wiki/File:DC_SQUID.svg#mediaviewer/DC_SQUID.svg>
- [31]Clarke, John. "5254950 DC superconducting quantum interference device usable in nuclear quadrupole resonance and zero field nuclear magnetic spectrometers." Magnetic Resonance Imaging: XXIV. Print.

- [32]Clarke, J.. *The SQUID handbook*. Weinheim: Wiley-VCH, 20032004. Print.
- [33]Finkler, Amit. "SQUID on tip sensors." . Weizmann Institute , 1 Nov. 2012. Web. 30 Jun. 2014. <<http://www.weizmann.ac.il/condmat/superc/SOT.html>>.
- [34]"IV curve" by Janolaf30 - Own work. Licensed under Public domain via Wikimedia Commons <https://commons.wikimedia.org/wiki/File:IV_curve.jpg#mediaviewer/File:IV_curve.jpg>
- [35]"LabVIEW System Design Software." NI LabVIEW. National Instruments, n.d. Web. 15 June 2014. <<http://www.ni.com/labview/>>.
- [36]"High-performance low-noise dc SQUID sensors." . Magnicon, 1 Mar. 2011. Web. 27 Feb. 2014. <http://www.magnicon.com/fileadmin/download/datasheets/Magnicon_Squids.pdf>.
- [37]"Thickness Shear Mode Quartz Oscillator." Thickness Shear Mode Quartz Oscillator. COMSOL Multiphysics, n.d. Web. 1 May 2013. <<http://www.comsol.com/model/thickness-shear-mode-quartz-oscillator-4707>>.
- [38]"QCM100- Quartz Crystal Microbalance Theory and Calibration ." . Stanford Research Systems, n.d. Web. 14 June 2014. <<http://www.thinksrs.com/downloads/PDFs/ApplicationNotes/QCMTheoryapp.pdf>>.
- [39]Wenzel. "SWR, Return loss, and Reflection Coefficient ." . Wenzel Associated, 1 Jan. 2011. Web. 1 Jan. 2014. <<http://www.wenzel.com/documents/swr.html>>.
- [40]Tittmann, Bernhard R. "High temperature ultrasonic transducer up to 1000 °C using lithium niobate single crystal." *Applied Physics Letters* 97: 232901. *Applied Physics Letters*. Web. 7 Feb. 2014.
- [41]Slavov, S. H., and A. V. Apostolov. "Frequency Spectrum and Modes of Vibration in Circular, Convex AT-cut Bevelled-design Quartz Resonators." *Applied Physics A Solids and Surfaces* 7 (1974): 173-75. 1 Jan. 1974. Web. 6 Aug. 2014.
- [42]Caruso, Frank, Elke Rodda, D. Neil Furlong, Kenichi Niikura, and Yoshio Okahata. "Quartz Crystal Microbalance Study of DNA Immobilization and Hybridization for Nucleic Acid Sensor Development." *Analytical Chemistry* (2008): 2043-049. 1 Apr. 2008. Web. 2 July 2014. <http://www.egr.msu.edu/~hashsham/courses/ene806/docs/Final_Report_for_QCM--by_Chang_and_Zhao-revised.pdf>.

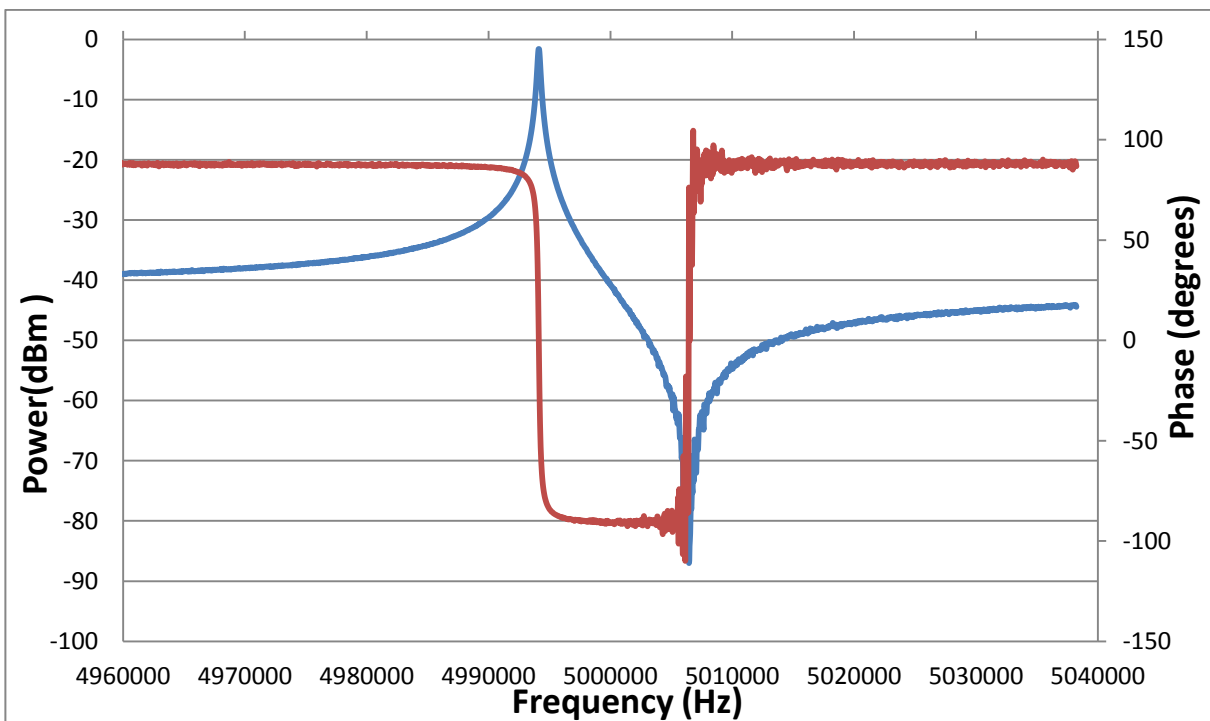
- [43]Marx, Kenneth A. "Quartz Crystal Microbalance: A Useful Tool for Studying Thin Polymer Films and Complex Biomolecular Systems at the Solution–Surface Interface." *Biomacromolecules* (2002): 1099-120. Print.

Appendices

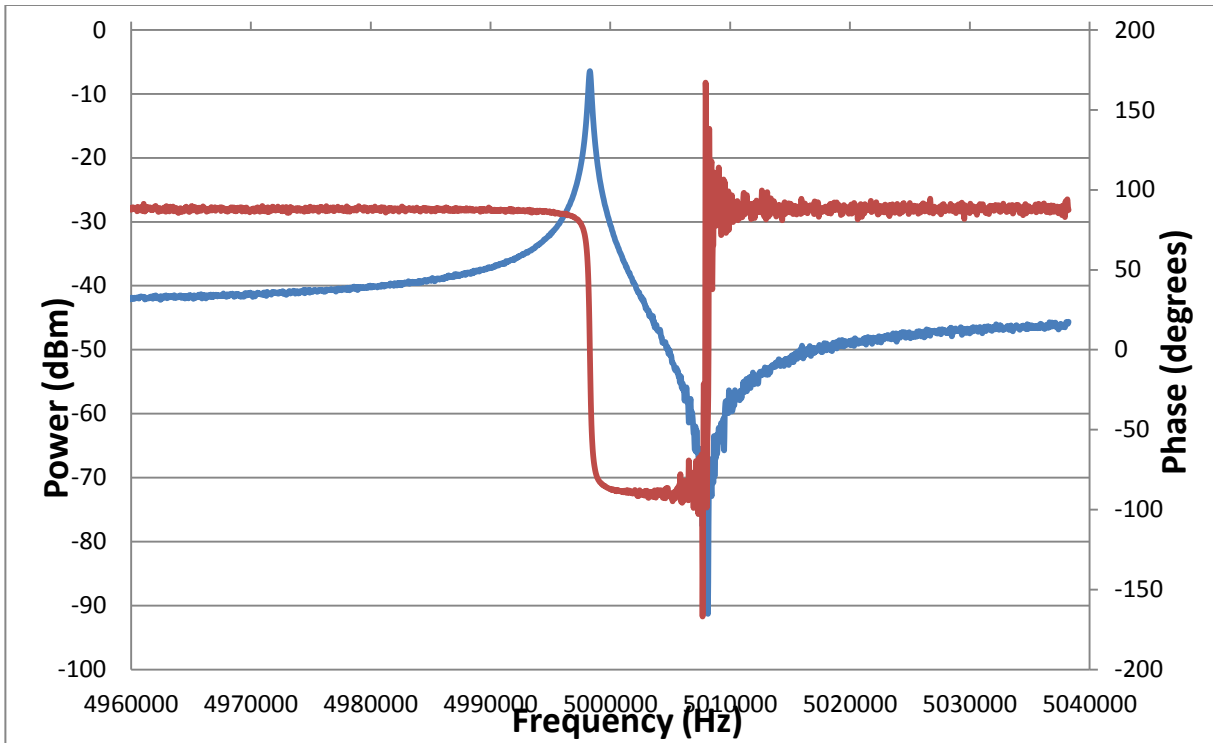
Appendix A: FRA data for common oscillators



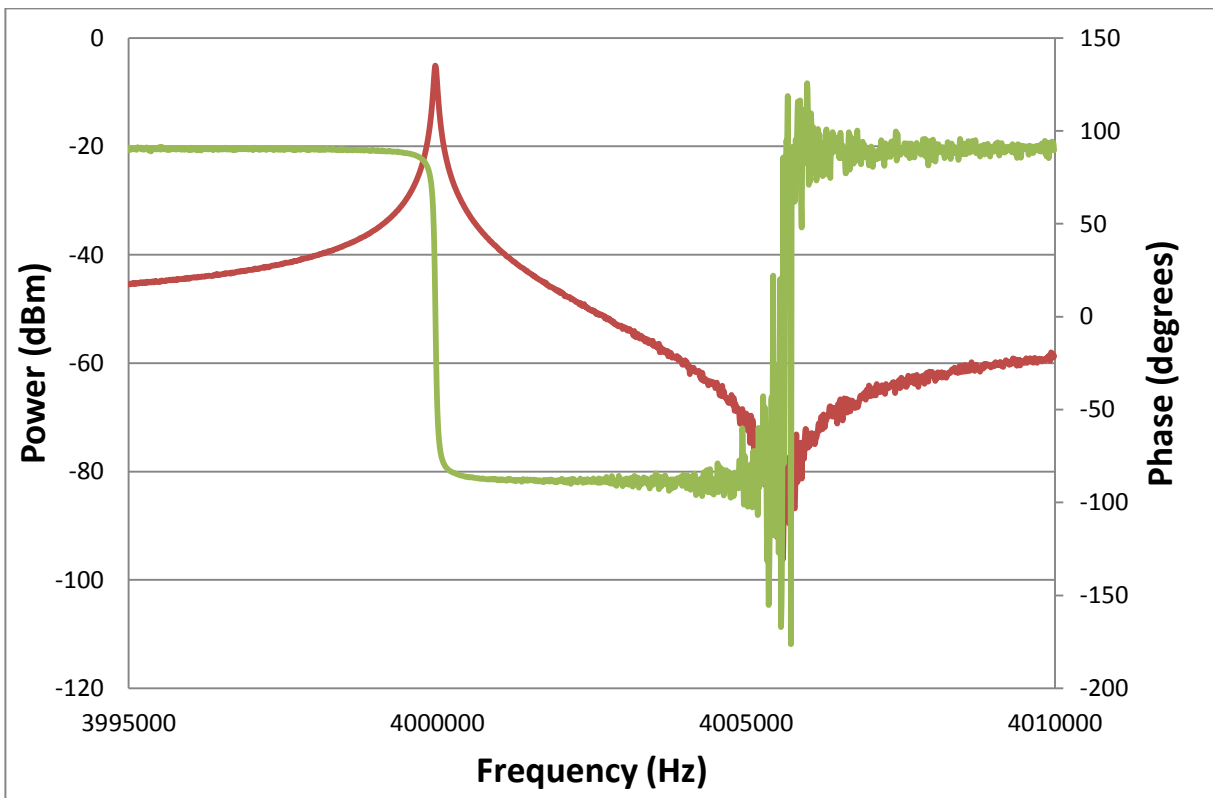
Frequency response (phase in blue) of a 5 MHz "large" oscillator



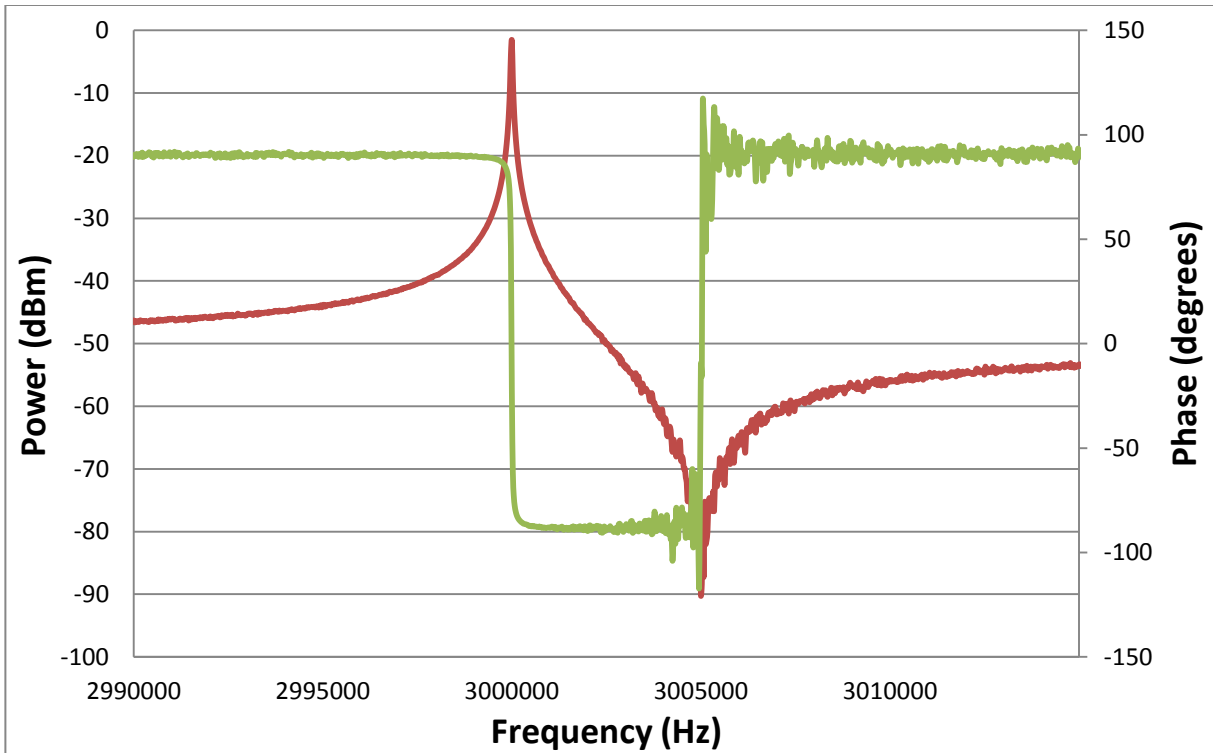
Frequency response (phase in blue) of a 5 MHz "open" oscillator



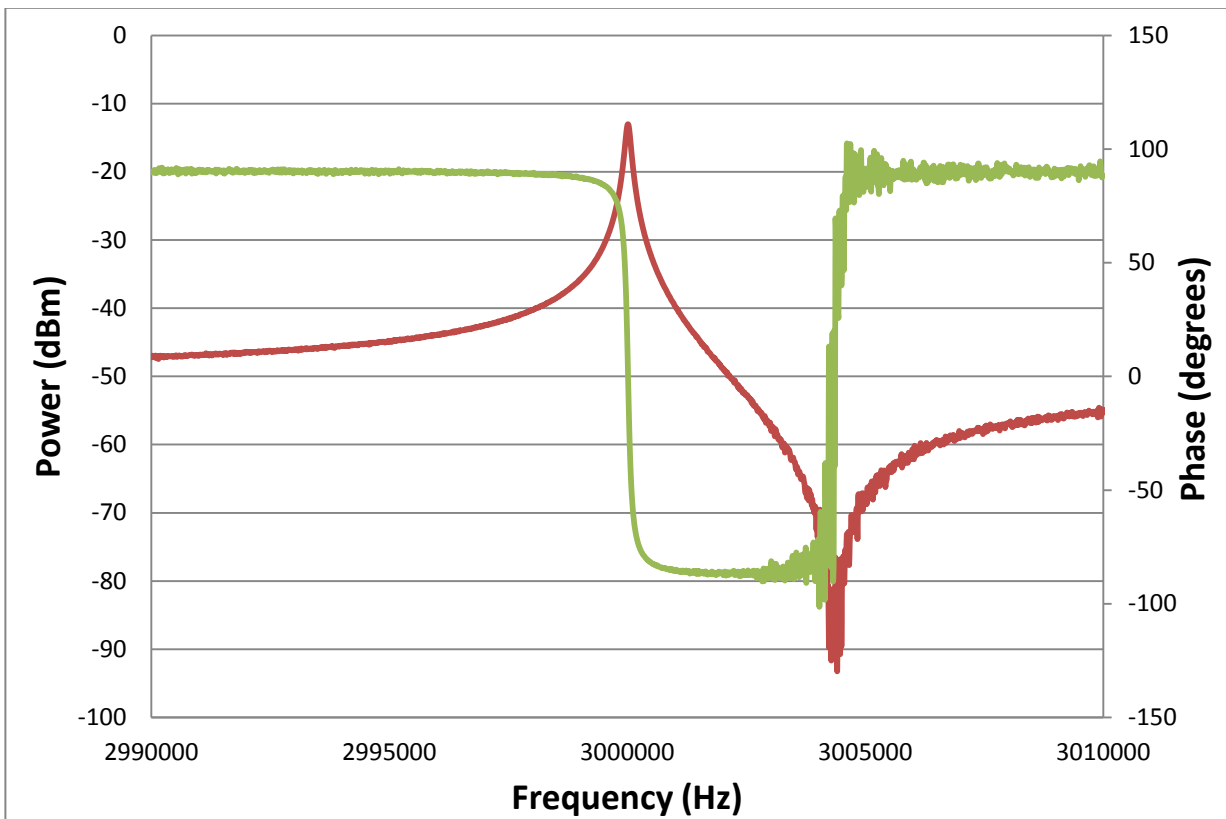
Frequency response (phase in blue) of a 5 MHz "small" oscillator



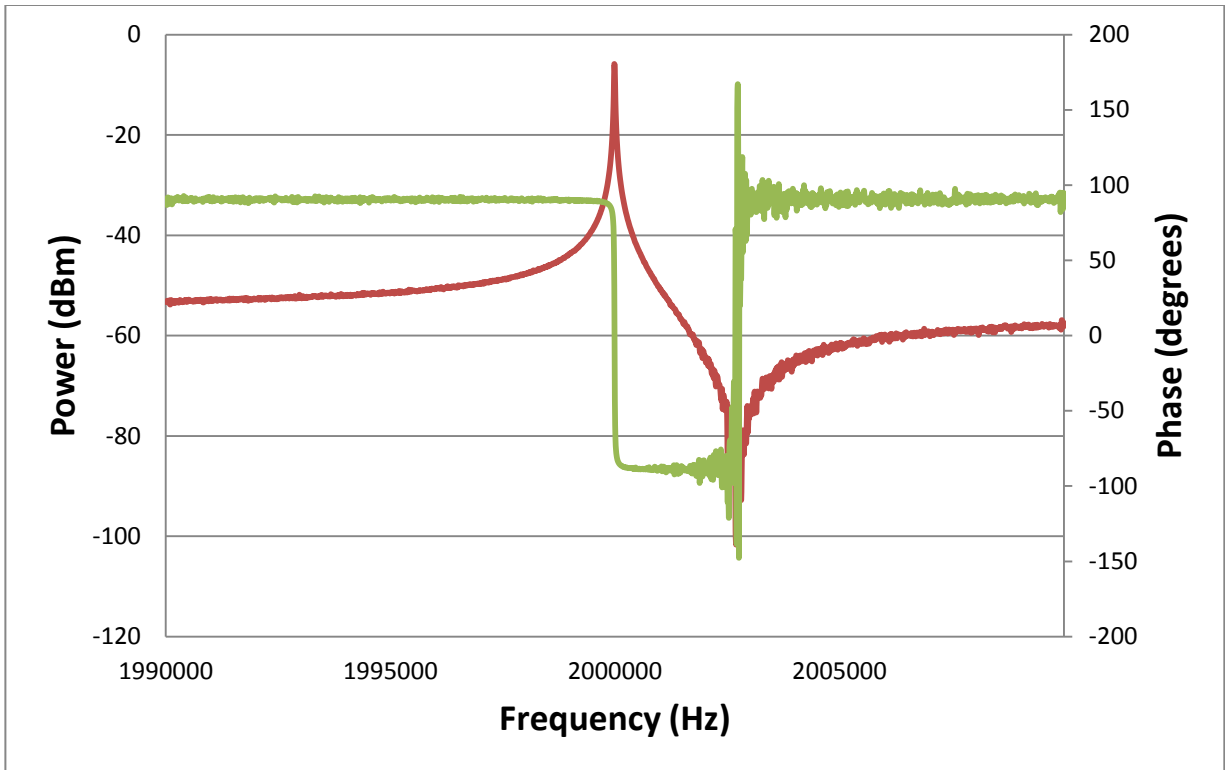
Frequency response (phase in green) of a 4 MHz oscillator



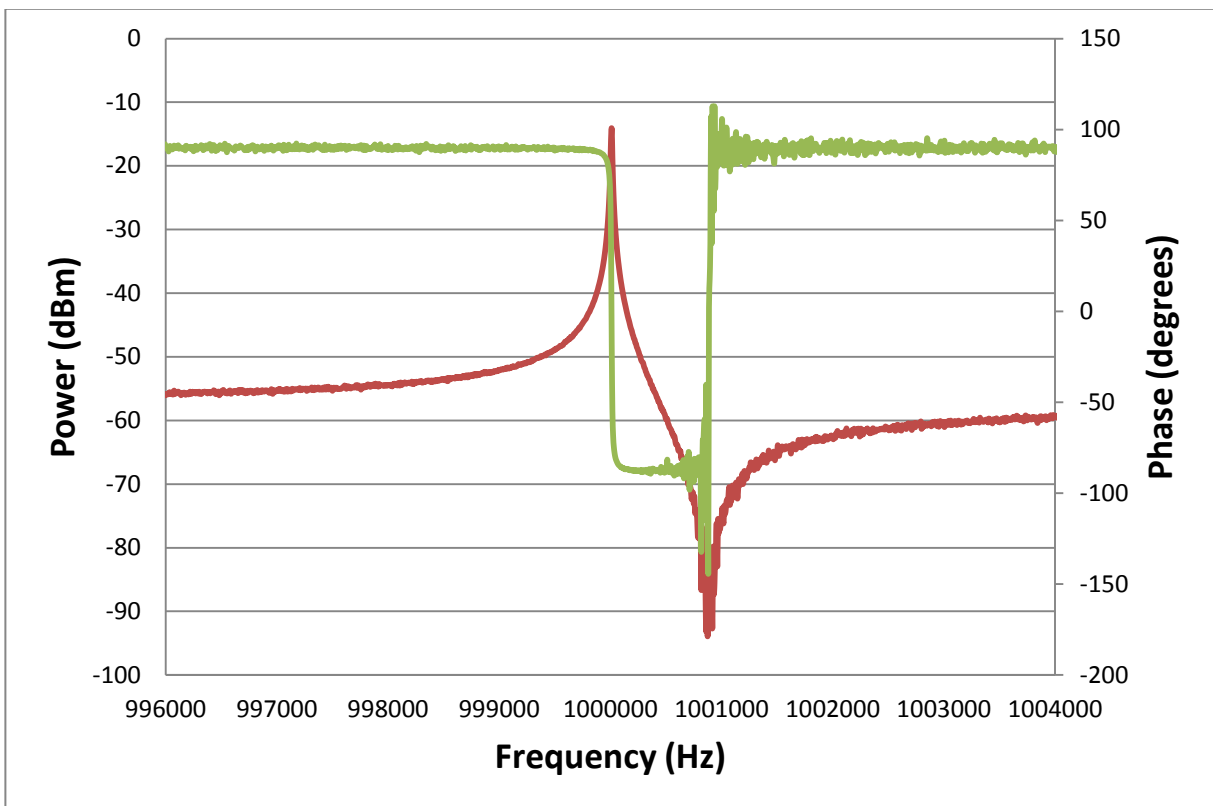
Frequency response (phase in green) of a 3 MHz "large" oscillator



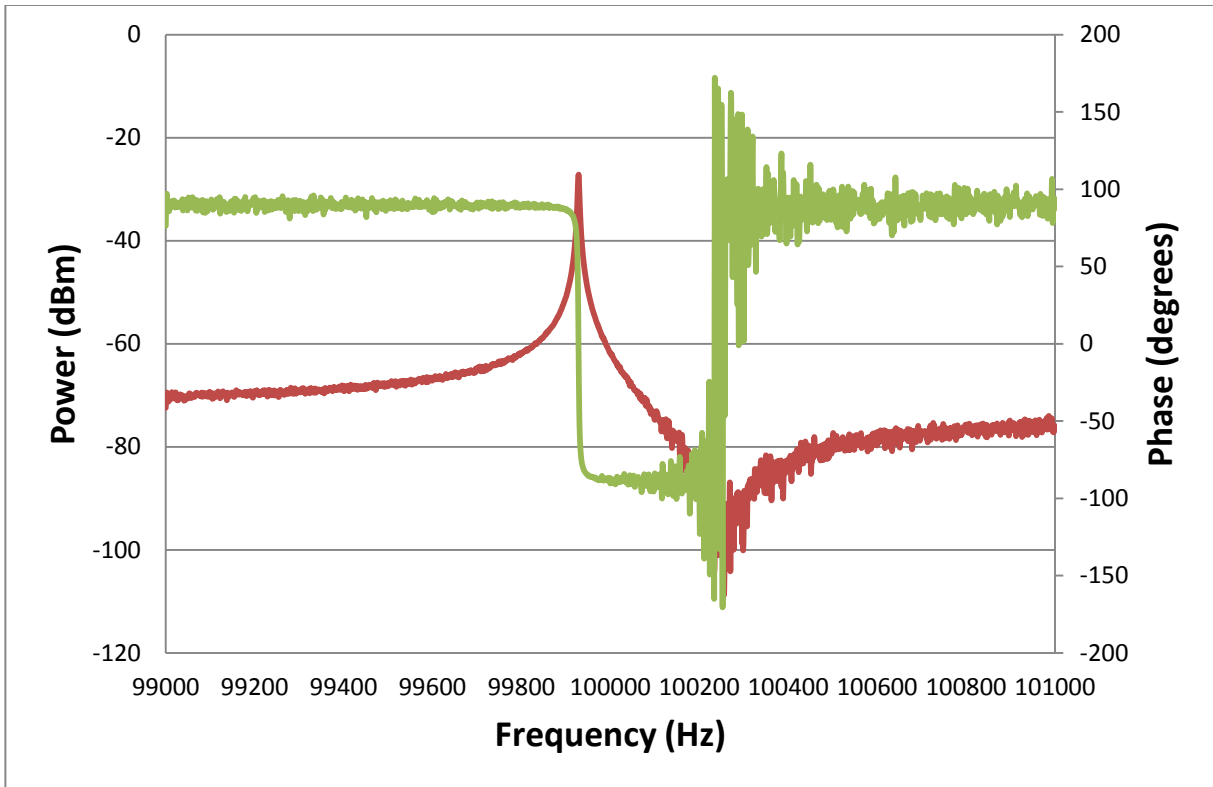
Frequency response (phase in green) of a 3 MHz "small" oscillator



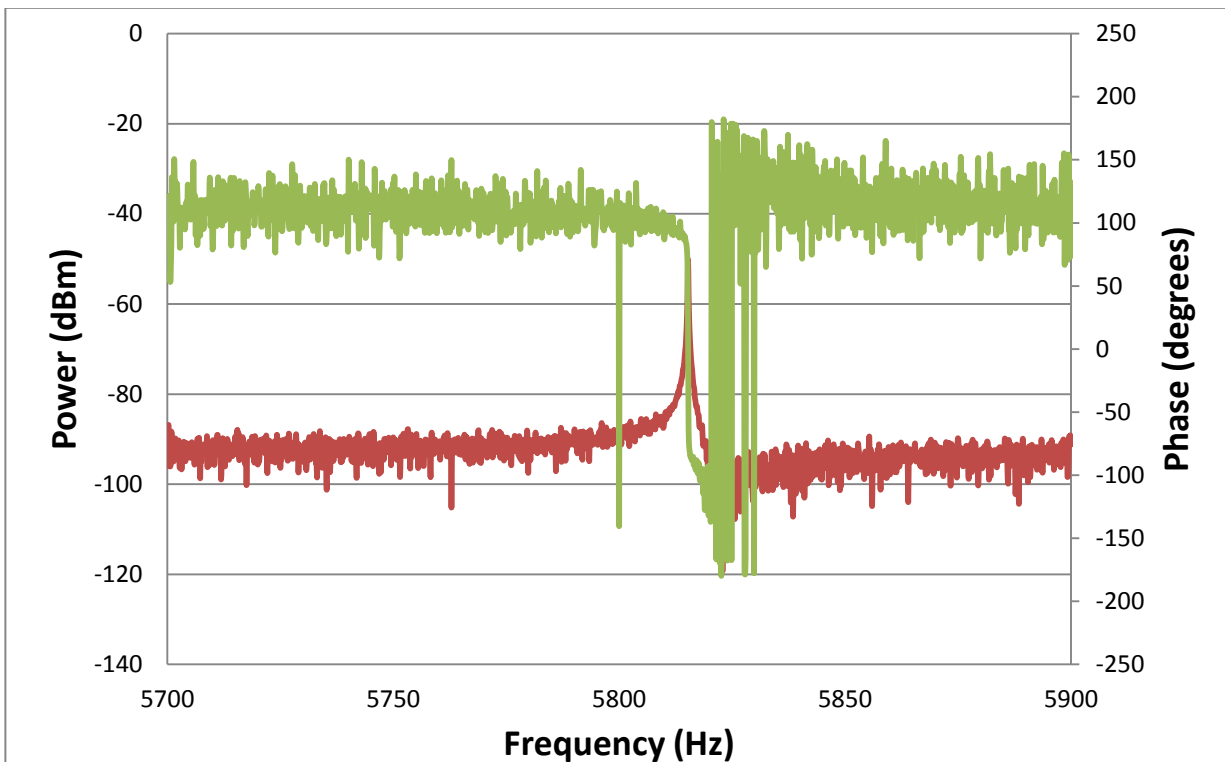
Frequency response (phase in green) of a 2 MHz oscillator



Frequency response (phase in green) of a 1 MHz oscillator



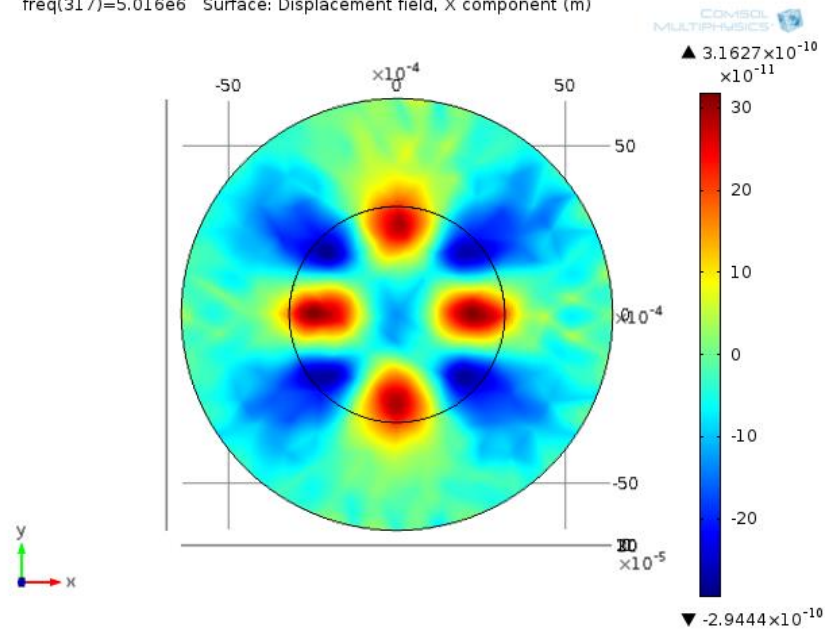
Frequency response (phase in green) of a 100 KHz oscillator



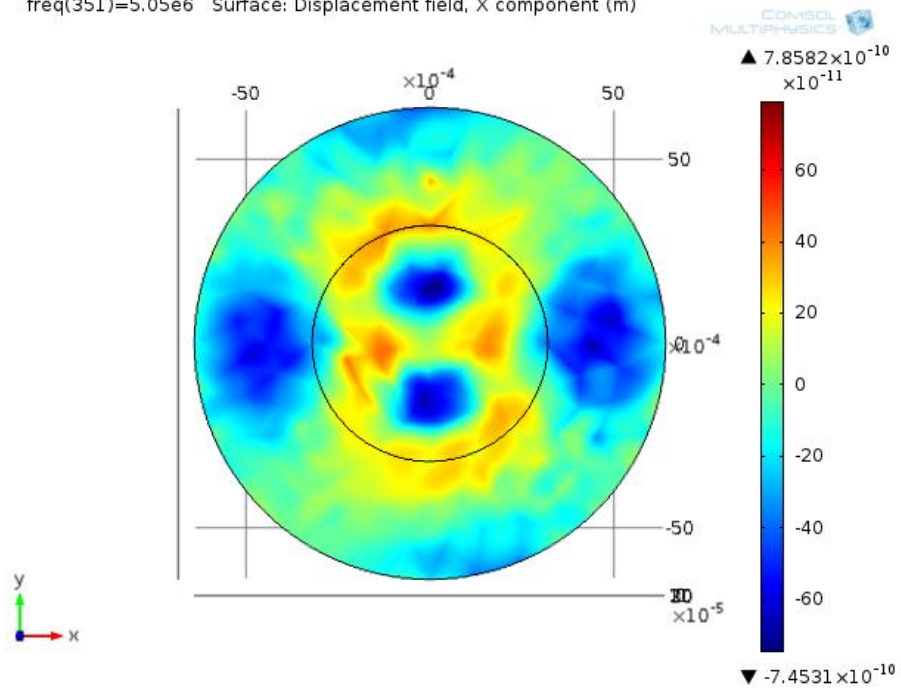
Frequency response (phase in green) of a 5814 Hz oscillator –UNUSED–

Appendix B: Multimodal Operation of Digital Model

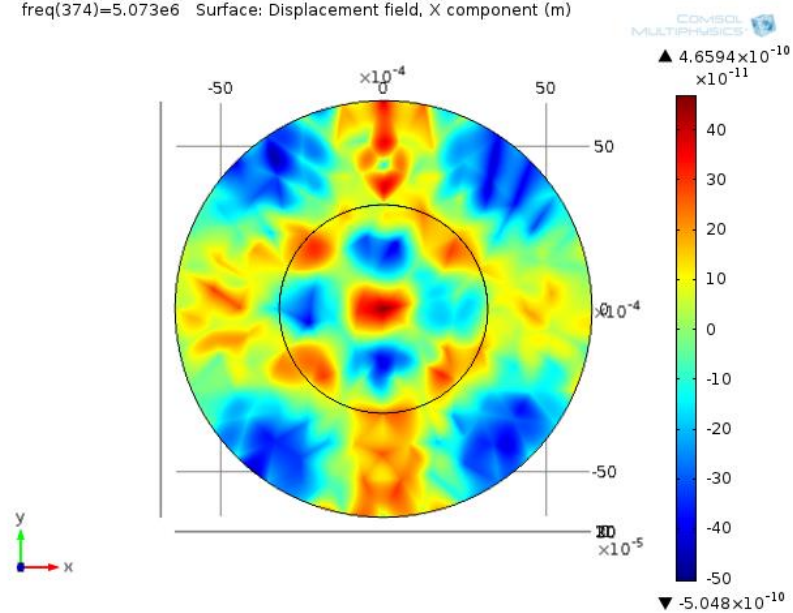
freq(317)=5.016e6 Surface: Displacement field, X component (m)



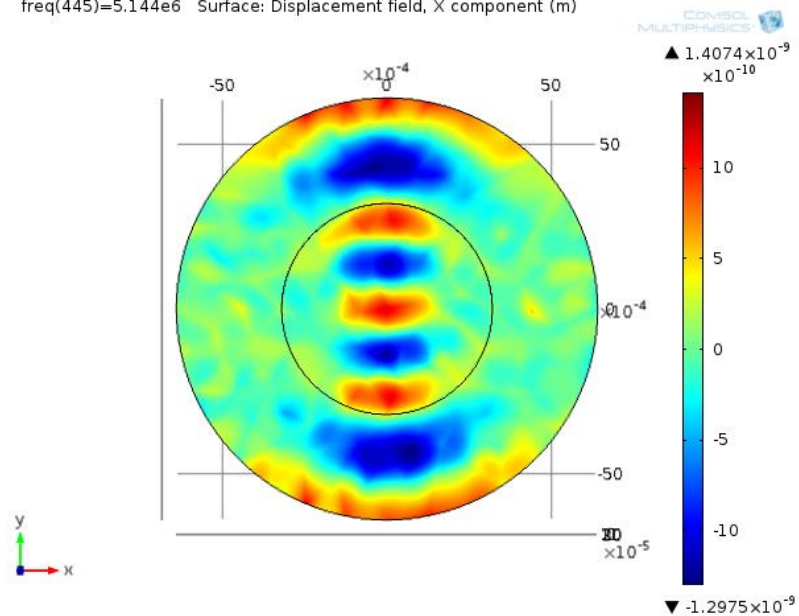
freq(351)=5.05e6 Surface: Displacement field, X component (m)



freq(374)=5.073e6 Surface: Displacement field, X component (m)



freq(445)=5.144e6 Surface: Displacement field, X component (m)



Appendix C: SQUID linearization data

(Values in dBm)	100uV	500uV	1mV	5mV	10mV	- 20dBm	50mV	100mV
5 MHz	-97.42	-86.40	-80.75	-67.79	-61.55	-53.75	-52.43	-50.65
4 MHz	-96.94	-85.12	-78.75	-65.66	-59.30	-51.72	-50.46	-48.88
3 MHz	-96.52	-82.37	-76.39	-63.08	-57.04	-49.53	-48.07	-46.67
2 MHz	-91.19	-78.02	-72.21	-59.02	-52.76	-45.62	-44.56	-43.33
1 MHz	-85.77	-71.80	-65.76	-52.66	-46.36	-39.48	-38.55	-37.48
100 KHz	-75.85	-61.89	-55.86	-42.53	-35.95	-26.00	-22.87	-18.88
5831 Hz	-94.23	-95.03	-94.45	-94.41	-95.68	-99.18	-98.54	-96.62

Appendix D: Half max frequency input-response data for QCM/oscillators

Osc. description	high/low value	Frequency (Hz)	Peak power (dBm)
5 MHZ Large	Low	4996900.00	-33.29
	High	4998700.00	-32.97
5 MHZ Small	Low	4997125.00	-38.11
	High	4999225.00	-38.57
QCM	Low	4993000.00	-33.70
	High	4995075.00	-34.61
4 MHZ	Low	3999750.00	-38.62
	High	4000200.00	-37.32
3 MHZ Large	Low	2999712.50	-38.37
	High	2999725.00	-38.93
3 MHZ Small	Low	2999450.00	-45.27
	High	3000462.50	-45.23
2 MHZ	Low	1999850.00	-42.87
	High	2000112.50	-42.45
1 MHZ	Low	999937.50	-48.99
	High	1000075.00	-48.69
100 KHZ	Low	99925.00	-48.12
	High	100124.85	-48.18